DEVELOPMENT, ANALYSIS AND SYNTHESIS OF A THREE-DEGREE-OF-FREEDOM TRANSLATIONAL TENSEGRITY MECHANISM

DÉVELOPPEMENT, ANALYSE ET SYNTHÈSE D'UN MÉCANISME DE TENSÉGRITÉ AVEC TROIS DEGRÉS DE LIBERTÉ EN TRANSLATION

A Thesis Submitted to the Division of Graduate Studies
of the Royal Military College of Canada
by

Christopher Mohr, B.Sc.(Eng)

In Partial Fulfillment of the Requirements for the Degree of
Master of Applied Science in Mechanical Engineering

July, 2015

"It's a magical world, Hobbes, ol' buddy... let's go exploring!"
-Calvin and Hobbes, by Bill Watterson

Acknowledgements

I am greatly indebted to the many people who assisted me during my master's work. This thesis would not have been possible for me to complete without you.

Above all, I would like to thank my supervisor Dr. Marc Arsenault. His knowledge, support, and advice have been invaluable throughout this endeavour and have had a profound impact on my academic and professional development. Additionally, I am extremely grateful for his financial support.

I would like to acknowledge all of the technicians (Dana, Dave, Mike, Brian, Marc, Wendy, and John) in the Mechanical Engineering Department who assisted me with the machining and construction of the mechanism prototype. They demonstrated a great deal of patience with my numerous requests and produced work at a level of quality that exceeded all of my expectations.

Finally I would like to recognize the endless moral support I received from my parents, Lloyd and Nancy, the rest of my family, my friends and especially my fiancé Jennifer. Thank you all for helping me maintain my sanity.

Abstract

This thesis presents a novel robotic mechanism based on the structural concept of Tensegrity. Winch-driven cables are used to actuate the mechanism in such a way that it experiences only translational motion of its end-effector. This behaviour, and the reduction of the mechanism's inertia due to the use of cables, could be beneficial for certain industrial operations.

A comprehensive study was conducted to investigate the behaviour of the proposed tensegrity mechanism. Kinematic analysis was performed to explore the relationship between actuator and end-effector coordinates, kinematic singularities, reachable workspace volume, and mechanical interferences between internal components. Models of the mechanism were derived to verify that tension is maintained within all cables for both static and dynamic cases. These models were used to determine external forces or accelerations that the mechanism can attain without losing cable tension, and thus controllability. Stiffness was also investigated, as it relates to the accuracy of the end-effector's position.

Additionally, the construction of a functional prototype is outlined. The design challenges faced when manufacturing this proof-of-concept are examined and a discussion of the chosen design approaches is included. Recommendations are made for future experimental work to evaluate the mechanism performance and validate the theoretical work of this thesis. The finished prototype may act as a platform for further development.

Résumé

Dans cette thèse, un mécanisme robotique novateur qui est développé à partir du concept de tenségrité est présenté. Le mécanisme est actionné à partir de câbles dont les longueurs sont modifiées par des treuils de manière à obtenir un mouvement en translation de sa plate-forme mobile. Ce type de mouvement, combiné avec une réduction de l'inertie du mécanisme en raison de l'utilisation de câbles, font du mécanisme un candidat intéressant pour certaines applications industrielles.

Une étude approfondie du mécanisme de tenségrité proposé est présentée. D'une part, une analyse cinématique permet d'établir le lien entre les longueurs des câbles et la position de la plate-forme mobile, d'identifier les singularités du mécanisme, de calculer les limites de son espace atteignable et de déceler l'existence d'interférences entre ses composants mécaniques. D'autre part, des modèles statique et dynamique du mécanisme permettent de vérifier les conditions nécessaires pour que ses câbles demeurent tendus pendant son opération. Ces modèles sont également utilisés pour calculer les forces externes pouvant être supportées par le mécanisme ou encore les accélérations qu'il peut exécuter lors de ses mouvements tout en gardant ses câbles tendus. Une analyse de la raideur du mécanisme est présentée de manière à évaluer l'exactitude avec laquelle la plate-forme mobile peut être positionnée dans son espace atteignable.

Finalement, la conception et la fabrication d'un prototype fonctionnel du mécanisme sont décrites. Les défis rencontrés pendant la fabrication du prototype sont expliqués et les décisions de conception sont justifiées. Certaines recommandations sont faites concernant des travaux futurs visant à mieux évaluer la performance du mécanisme et la validité de certains résultats théoriques obtenus dans cette thèse. Le prototype, pour sa part, est apte à être utilisé comme point de départ pour des recherches plus approfondies dans le domaine des mécanismes de tenségrité.

Contents

List of Tables

List of Algorithms

List of Figures

List of Symbols and Acronyms

A_i, B_i, C_i	The ith node of the mechanism's base, end-effector or torsion spring joint, respectively.
$\mathbf{A}$, $\mathbf{B}$	Equilibrium and compatibility matrices[1] of a pin-jointed structure.
$\mathbf{a}_i$, $\mathbf{b}_i$, $\mathbf{c}_i$	Vectors[2] locating nodes A_i, B_i, and C_i respectively.
$\mathcal{D}$	Dimension of the space being considered (i.e., 2 for planar, 3 for spatial).
$\mathcal{D}_b$	Degrees-of-freedom of a rigid body (i.e., 3 for planar, 6 for spatial).
$\mathcal{D}_i$	Number of degrees-of-freedom allowed by a mechanical joint.
$\mathbf{d}$	Vector containing the nodal displacements of a pin-jointed structure.
$\mathbf{e}$	Vector containing the elongations of all components in a pin-jointed structure.
$\mathbf{e}_{1i}$, $\mathbf{e}_{2i}$	Unit vectors defining the two axes of the universal joints found at the base of the i-th spring linkage.
$\mathbf{f}$	Force vector.
g, $\mathbf{g}$	Magnitude and direction of gravity (9.81 ms^{-2}).
$\mathbf{i}$, $\mathbf{j}$, $\mathbf{k}$	Unit vectors along global axes X, Y and Z, respectively.
$\mathbf{I}$	Inertia tensor.
$\mathbf{1}_{n\times n}$	Identity matrix, $n \times n$.
$\mathbf{J}$	The overall Jacobian matrix of the mechanism.
$\mathbf{J}_{\boldsymbol{\rho}}$, $\mathbf{J}_{\mathbf{x}}$	The partial Jacobian matrices.
$\mathbf{K}$	Stiffness matrix.

[1] All matrices are denoted by uppercase bold-faced characters.
[2] All vectors are denoted by lowercase bold-faced characters.

l_i	Length of the i-th virtual spring, defined as the distance between nodes A_i and B_i.
l_0	Rest length of the virtual compression spring linkages.
$\mathcal{M}$	Degree of static indeterminacy of a structure.
M	Mobility of a mechanism.
N_b	Number of bars or components in a pin-jointed structure.
N_I	Number of infinitesimal mechanisms.
N_j	Number of joints in a pin-jointed structure.
N_k	Number of kinematic constraints in a pin-jointed structure.
$\mathbf{n}_{ij}$	Unit vector describing the direction of a component between nodes i and j.
O	Origin of the global coordinate frame.
$\mathbf{p}$,$\dot{\mathbf{p}}$	Position vector of the tensegrity mechanism end-effector and its time derivative.
$\mathbf{Q}$	Rotation matrix.
$\mathbf{q}$	Vector containing a compatible change in the length of cables and springs.
r_b	Radius of the circumscribed circle formed by the base and end-effector triangles.
r_f	Maximum magnitude of a wrench that can be applied in any arbitrary direction for a given Available Wrench Set.
s_S	Number of prestress states.
T	Kinetic energy term.
$\mathbf{t}$	Vector of tensile forces.
$\mathbf{t}^*$	Vector of tensile and virtual compressive forces.
U	Potential energy term.
$\mathbf{u}_i$,$\mathbf{u}_{pi}$,$\mathbf{u}_{di}$	Unit vectors describing the direction of the ith virtual spring leg, proximal link and distal link, respectively.
$\mathbf{v}_j$	Unit vector describing the direction of the jth cable.
$\mathbf{W}$	Wrench matrix, relating cable tensions to net wrench.
$\mathbf{W}_K$	Extended wrench matrix, relating cable tensions *and* virtual spring forces to net wrench.
$\mathbf{w}$	Wrench vector, of the form $[f_x, f_y, f_z, n_x, n_y, n_z]$.
XYZ	Global coordinate frame, located at O.
$X'Y'Z'$	Body fixed reference frame attached to end-effector and located at P.
$\mathbf{x}$	Pose vector of mechanism, defining the position and orientation of the end-effector.
x, y, z	Cartesian coordinates of the end-effector position.

α_i,β_i	Rotation angles of the ith universal joint.
γ	Twist angle of tensegrity prism equilibrium configuration.
ε	Number of sides on a tensegrity prism's face.
η	Condition number of a stiffness matrix.
θ_i	Half angle between the two segments of the ith spring leg.
κ	Linear stiffness coefficient of the torsion springs.
λ, $\boldsymbol{\lambda}$	Lagrangian multipliers.
$\boldsymbol{\rho}$, $\dot{\boldsymbol{\rho}}$	Vectors of actuated cable lengths and their rates of change.
ρ_i	Actuated length of the ith cable pair.
τ_i	Torque generated in the ith torsion spring joint.
$\boldsymbol{\phi}$, ϕ_j	Kinematic constraints imposed by the actuated cable lengths.
φ, χ, ψ	Euler angles about the body fixed axes X', Y' and Z', respectively.
$\boldsymbol{\omega}$,$\boldsymbol{\omega'}$	Angular velocity in the global and body fixed reference frames, respectively.

AWS	Available Wrench Set (also $\mathcal{A}$)
DoF	Degrees of Freedom
CDPM	Cable Driven Parallel Mechanism/Manipulator

1 Introduction

Robotic manipulators have become commonplace in nearly all aspects of modern manufacturing. The primary reason for this widespread adoption is their ability to perform repetitive tasks at speeds and accuracies unachievable by humans. Humans are, in this case, a poor standard for comparison and there are strong motivations (e.g., economic) for further increasing the accelerations that manipulators can achieve. While evolutionary changes to existing designs of manipulators can gradually increase the acceleration limits, at some point more revolutionary changes must be attempted. Applying the structural concept of tensegrity to the field of robotics is one possible approach.

1.1 Robotic Manipulator Background

The term robot has been used to describe a large number of diverse applications. To some, the word robot brings to mind humanoid automatons from science fiction movies. Others are reminded of mobile robots such as those used by NASA for space exploration. In the context of this thesis, the only robots that will be referred to are robotic manipulators, used widely in industry to machine, assemble and package consumer goods. These manipulators are usually composed of rigid links connected by joints, some of which are actuated.

An extensive review of the history and development of early robotic manipulators is not necessary for the understanding of this thesis. The subject is already covered in many robotics textbooks, for example those by Tsai [1] or Angeles [2], and will be omitted here. Instead, a brief overview of the current state of the art of high-speed manipulators will be presented.

1.1.1 Serial Manipulators

Most robotic manipulators in use today may be categorized as rigid link manipulators. Rigid link manipulators are usually further categorized into two

primary architectures: serial and parallel. Serial manipulators, as shown in Figure 1.1a, are the more widely adopted architecture in industry. They are composed of a series of rigid links that are connected by fully actuated joints. The actuators are able to position subsequent links in the open kinematic chain, with the goal of locating and sometimes orienting the final link, known as the end-effector. Serial manipulators often appear anthropomorphic since they can be similar in function to human limbs.

Serial manipulators are well established due to their large reachable workspace, i.e., the area or volume in which they can position or orient their end-effector. Additionally, simpler analysis of their kinematics and dynamics makes the task of mechanical design easier. However, the high-speed performance of serial manipulators has inherent limitations. The naive approach to improve the dynamic abilities of a serial manipulator would be to reduce its mass, and thus inertia, while increasing the force or torque output of the actuators. Unfortunately, these are conflicting objectives; stronger actuators are generally more massive and, due to the serial architecture, will contribute to the inertia of the overall manipulator. In most applications, more massive actuators also require larger, stiffer links to prevent the manipulator from becoming undesirably flexible. The serial architecture also reduces the overall stiffness of the manipulator at the end-effector, since it is the summation of the stiffness of all included joints and links. Multi-objective optimization to improve high-speed performance is possible but it remains difficult to substantially increase the achievable accelerations of existing designs.

1.1.2 Parallel Manipulators

The second category of rigid link manipulators is parallel manipulators. Rather than an open kinematic chain, this type of manipulator includes multiple series of links that create closed kinematic chains, as shown in Figure 1.1b and Figure 1.2a. Not all joints need be actuated in a closed kinematic chain to completely define its configuration. This allows a degree of choice when selecting which joints are actuated. As such, the joints closest to or located on the stationary base are typically chosen, significantly reducing the contribution of the actuators to the manipulator's inertia. Without needing to support heavy actuators, the links of parallel manipulators may be much less massive than their serial counter-parts. The stiffness, and thus accuracy, of parallel manipulators is higher than serial architectures. This is due to the increased number of serial connections to the end-effector and the reduced number of individual joints and links in the linkages, which eliminates the cascading effect that serial chains have on stiffness. Adding redundant linkages, i.e., more than

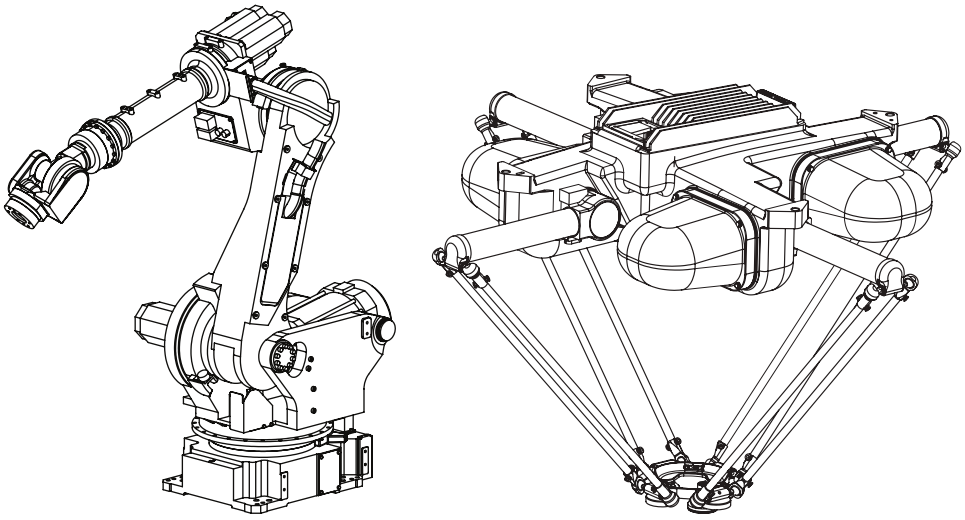

(a) **(b)**

Figure 1.1: Comparison of (a) the FANUC 430 serial manipulator and (b) the Adept Quattro parallel manipulator. Vector images created by the author using royalty-free CAD models obtained from GrabCAD.com [3].

needed to fully define the position of the end-effector, has been used to achieve higher accelerations [4]. Further gains have been found by using pantograph linkages to effectively magnify the forces generated by actuators [5].

Improvements to dynamic performance come at the cost of much more complicated analysis and design. Parallel manipulators tend to have relatively small, irregularly shaped workspaces due to the increased number of kinematic constraints introduced by the additional kinematic chains. This has to some extent limited the adoption of parallel manipulators to specialized tasks, such as pick-and-place operations in food or packaging industries, where a large workspace is not necessary.

1.1.3 Cable-Driven Parallel Manipulators

More recent research has been shifting to cable-driven parallel manipulators (CDPM). Early examples include the Landsberger mechanism [6], NIST Robocrane [7] and the Falcon [8]. Many are based loosely off of the Gough-Stewart parallel platform, shown in Figure 1.2a, essentially being a platform that is positioned and oriented in space by several linear actuators. Instead of heavy linear actuators, CDPMs use winch-actuated cables. In most cases,

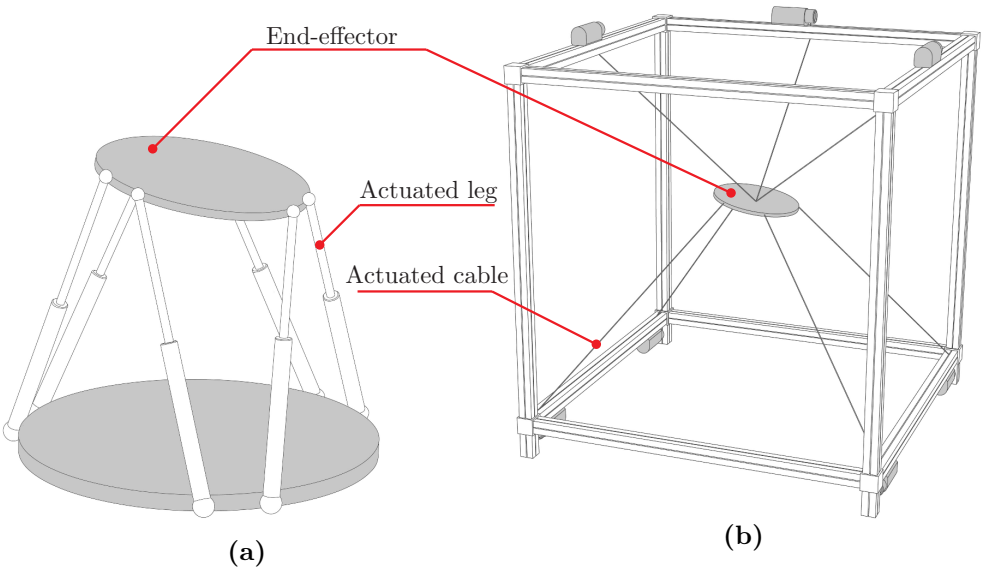

Figure 1.2: A comparison of (a) the 6-DoF Gough-Stewart platform and (b) a 6-DoF cable-driven parallel manipulator. Images adapted from Bruckmann et al. [12].

certainly those in small-scale manufacturing, the cable mass can be neglected, eliminating nearly all of the inertia of the manipulator aside from that of the end-effector, its payload, and the rotational inertia of its winches. Since nearly any length of cable may be reeled onto a winch, CDPMs can also be built to extremely large scales. Large-scale applications already include a cable suspended camera used to film sporting events [9], deployable cranes for the construction of solar farms [10] and proposed deployable search and rescue robots [11].

Cable actuation does however introduce a new constraint to the manipulator; cable tension must be maintained. Two approaches may be used to supply cable tension. In the case of suspended CDPMs, the weight of the end-effector and payload platform pulls on the cables. Alternatively, some CDPMs may introduce at least one redundant cable to pull antagonistically against the others and maintain tension. A drawback of this approach is that the cables will always surround the end-effector. In such cases CDPMs are more difficult to implement due to their required footprint and the likelihood of cables interfering with each other or other objects in a workspace. Hybrid manipulators, comprising of both actuated cables and rigid links, have also been proposed. These benefit from high-speed actuation due to the low

mass cables while maintaining large unobstructed workspaces by using other methods of supplying tension to the cables, e.g., applying prestress using gas compression springs [13–15].

1.2 Tensegrity

1.2.1 Structures

American architect Buckminster Fuller was the first to coin the term *tensegrity*, as a compounding of the words *tension* and *integrity*. He used the word to describe a class of lightweight structures composed of axially loaded compression members held together by tension cables to form "islands of compression in a sea of tension" [16]. He was not, however, the first person to build such structures. Kenneth Snelson, an artist and early student of Fuller, has made numerous claims that he was the original inventor. In his book on tensegrity, Motro [17] gives a good account of the dispute between the two based on his correspondence with Snelson. Despite the competing claims, similar structures can be traced as far back as 1921 with the sculpture "A Study in Motion" by the Russian Constructionist artist Karl Ioganson [18].

It could be argued that while Snelson did create the earlier tensegrity sculptures, Fuller was the first proponent of their practical applications. In his 1962 patent [16], Fuller described a large number of applications, mainly related to architecture, which benefited from tensegrity's high strength-to-weight ratio and easy deployment. Snelson, on the other hand, focused almost entirely on the aesthetic properties of tensegrities. He built his sculptures using heuristic approaches rather than using calculations and often expressed his doubt in how practical any scientific or engineering study of the concept was [19]. However, he did concede in his own patent on "continuous tension, discontinuous compression structures" [20] that possible benefits of tensegrity structures exist in mass-critical applications such as aircraft structures.

The sculptural work of Snelson, such as the examples in Figure 1.3, illustrates the diversity of potential topologies quite well. Tensegrity structures can contain essentially an unlimited number of compressive elements so long as a network of tension cables is still present to hold them together in static equilibrium. This freedom allows for a wide spectrum of architectures, from minimal two or three strut tensegrities to very large repeating structures.

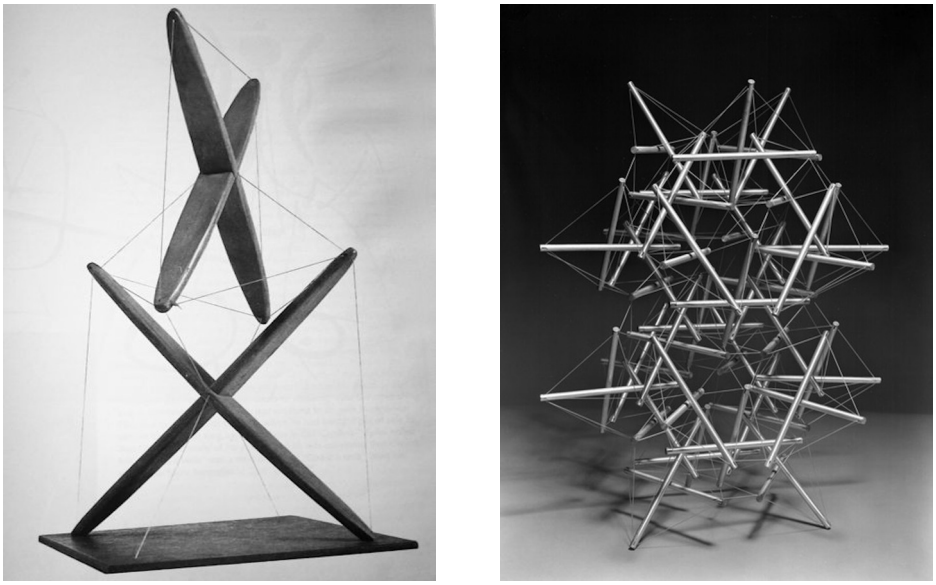

(a) **(b)**

Figure 1.3: The varying complexity of tensegrity sculptures, as demonstrated by (a) the *X-Piece (1948)* and (b) the *Double Star (1959)*, two sculptures by artist Kenneth Snelson. Photographs are from Snelson's online portfolio [21].

1.2.2 Mechanisms

The lengths of individual elements within tensegrity structures can be strategically actuated. Variations in these lengths can be controlled to cause desirable changes to the structures' geometry, leading to their possible use as mechanisms. In this context, a mechanism is a system of moving parts that can be controlled to generate desirable motions, although not all mechanisms are necessarily used as robotic manipulators. Mechanisms are generally less versatile than manipulators and designed to perform very specific and limited tasks. They are often found as components and sub-systems within devices, e.g., the read/write head within a disk drive. Coincidentally there exists a disk drive design with two read/write heads that is based on a planar tensegrity mechanism [22]. Tensegrity mechanisms are similar in many ways to parallel mechanisms and have many potential benefits.

As long as loads are applied to their nodes, elements within a tensegrity will remain axially loaded and will not experience bending moments. Without needing to resist bending, the tensegrity components can be much thinner and lighter without adversely affecting the strength of the structure as a whole.

This greatly reduces the mass and inertia of moving parts, potentially allowing high accelerations to be achieved during operation or the use of smaller (and cheaper) actuators. Stationary actuators, further reducing the inertia of the mechanism, can carry out the actuation of the structures' cables.

It has been observed that some tensegrity assemblies can be erected from a collapsed state by pulling on as few as one slack cable [23]. This creates the possibility of simple deployment, since manipulating tension within members can allow the entire structure to erect or collapse itself. Finally, tensegrity mechanisms that incorporate actuated cables generally do not require the complete surrounding of their end-effector by wires to be stable, unlike many cable-driven mechanisms. The lack of interference with cables could extend their workspace and simplify their practical implementation.

Research into the concept of tensegrity is not a recent occurrence but its application to the fields of mechanisms and robotics only began in the late 1990s. Early research considered controllable tensegrity smart structures, i.e., structures that could be actively actuated to reduce vibrations or have variable geometry [24]. Focus shifted to simpler tensegrity structures that could be made to generate much larger displacements [25]. These adaptive structures revealed many of the benefits that tensegrity mechanisms can potentially provide and opened the door to further development.

Tensegrity's high strength-to-weight ratio has generated interest in its use for aerospace applications. Emphasis has been placed on self-deploying tensegrity systems [26–28]. Deployable tensegrities could potentially be used as antennae masts on satellites [29]. Such designs could be packaged very compactly during launch and then deployed once in orbit. Most of these tensegrity masts are based on the simplest forms of tensegrity structures, the family of n-strut prisms [30]. Figure 1.4 shows a prototype tensegrity mast and illustrates how gradually applying tension to the structure's cables results in its erection.

Mechanisms with higher mobility, i.e., more degrees of freedom, have also been investigated. Control issues become more important when tensegrity is applied to higher speed manipulation applications. So too does the problem of path generation [32]. A large variety of tensegrity manipulators have been proposed. Sultan et al. suggested the use of a tensegrity mechanism as a flight simulator [33], similar to existing simulators based on the Gough-Stewart platform. Arsenault and Gosselin investigated both planar and spatial uses of tensegrity [34, 35], as well as modular mechanisms that could allow repeating tensegrity modules to be assembled into a quasi-serial manipulator [36, 37]. Tensegrity-like mechanisms have also been proposed; parallel manipulators developed to have self-stressing abilities similar to tensegrities [38].

Most recently, tensegrity has been applied to mobile robots. Generally,

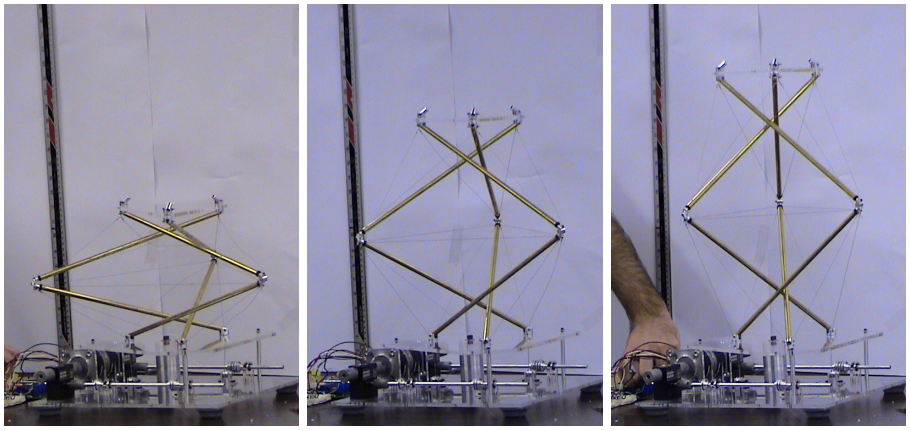

Figure 1.4: A deployable tensegrity mast prototype from the Skelton Structural Systems and Control lab at UCSD. Image adapted from Pinaud et al. [31]

these mechanisms are actuated to generate artificial gait or undulation for locomotion. Paul et al. used evolutionary algorithms (i.e., genetic algorithms) to generate a gait pattern to create the tensegrity mechanism shown in Figure 1.5a that can walk on the ends of its compressive members [39,40]. Rieffel explored similarities between biological systems (in this case caterpillars) and tensegrity mobile robots, using modular tensegrities to create an undulating motion to crawl [41]. In yet another example of generating a mobile robot from tensegrity, Shibata et al. designed a rolling tensegrity robot [42]. Mirats-Tur looked into using the minimal 3-strut prism to create rolling motion, simulating the mobile version of the mechanism to explore its dynamics [43]. He also built a preliminary prototype, shown in Figure 1.5b, with length actuated compression members and a stationary base to investigate physical implementation of the mechanism. The issue of where to locate the actuators, controllers and power supplies within a mobile tensegrity composed of nothing but cables and rods has yet to be addressed, limiting any real-world applications.

1.3 Motivation and Scope of Thesis

This thesis aims to demonstrate that tensegrity mechanisms are a feasible alternative to rigid link or cable-driven parallel manipulators. While adapting tensegrity structures into robotic manipulators has already been done, it has

(a) **(b)**

Figure 1.5: Example applications of the 3-strut prism tensegrity: (a) a tensegrity based mobile robot and (b) a stationary base tensegrity mechanism. Images adapted from Paul et al. [39] and Mirats Tur et al. [43], respectively.

only achieved a limited degree of success. Existing tensegrity mechanisms commonly suffer from several issues:

1. Limited (i.e., single) degrees of freedom appropriate for some applications, such as deployable mast-like space antennae, but undesirable from a manipulation standpoint.
2. Unrestrained degrees of freedom exist due to the extensive use of passive spring elements.
3. Complex actuation schemes that result in coupled translational and rotational movement of their end-effectors.
4. Theoretically possible designs that are difficult, if not impossible, to implement physically due to mechanical interferences.

To address these problems, a mechanism based on a known tensegrity architecture with a novel actuation scheme is presented. This mechanism will be shown to exhibit spatial, translational-only motion of its end-effector, making it well suited to manufacturing applications such as pick-and-place operations. Analysis of the mechanism's kinematics, statics, stiffness and dynamics is performed to gain a thorough understanding of its behaviour as well as to evaluate its feasibility as a practical robotic manipulator. The investigation is primarily performed using existing techniques that are common to the analysis of parallel manipulators and CDPMs by adapting them for use with tensegrity

mechanisms. Additionally, potential solutions to the challenges that are faced when attempting to translate tensegrity mechanisms from theory into reality are discussed. Some of these potential solutions are used to design and manufacture a prototype that will serve as a physical proof-of-concept and be used in future research.

2 Development of a Tensegrity Mechanism

The following chapter presents an expanded definition of tensegrity. Structural concepts such as self-stress and kinematic indeterminacy are explained, since they differentiate tensegrity architectures from the broader category of cable structures. A review of the mathematical tools used to analyze tensegrity structures is presented. Several existing tensegrity architectures are introduced, including the family of regular polygon prism tensegrities. Finally, this chapter describes the process of selecting a specific architecture, the reinforced triangular prism, and adapting it into the novel mechanism that will be the focus of the remainder of this thesis.

2.1 Definition of Tensegrity

Tensegrity has already been introduced as an assembly of compressive and tensile components. This basic description does not adequately describe all of the properties of this kind of cable structure. Additionally, the analysis in subsequent chapters relies on a thorough understanding of several key principles of tensegrity.

2.1.1 Tensegrity Architecture

To begin, the distinction between a tensegrity architecture and a tensegrity configuration must be made. Tensegrity architecture refers to a structural set of compression components and their specific connectivity via a network of tension components. However, not all combinations of compressive and tensile elements can form a stable tensegrity configuration, nor are all configurations of tensegrity architectures stable. To elaborate on this distinction, the following definition of tensegrity by Robert Skelton is provided:

> In the absence of external forces, let a set of rigid bodies in a specific *configuration* have torqueless connections... Then this *configuration* forms a *tensegrity configuration* if the given configuration can be stabilized by some set of internal tensile members, i.e., connected between the rigid bodies. The configuration is not a tensegrity configuration if no tensile members are required and/or no set of tensile members exist to stabilize the configuration. [22]

Skelton's definition describes tensegrity as being similar to a pin-jointed cable structure. It differentiates between a cable structure and a tensegrity, mainly by suggesting that tensegrity structures must have the ability to be self-stressing, i.e., they can reach static equilibrium without requiring external reaction forces. This ability must be achieved via internal changes to the amount of tension within a tensegrity's cables.

There are generally two types of components within tensegrity architectures: cables, which can only resist tension and struts, which must remain under compression. Some authors [44] also consider a third type of element, bars, that can support both tensile and compressive loads but must keep a constant length. Regardless of their type, each component must experience only uniaxial loading and not bending.

There is also some disagreement in literature with regards to the connection of compression elements. Some authors argue that the original definitions of tensegrity by Buckminster Fuller [16] and Kenneth Snelson [20] should be adhered to. This would require fully discontinuous compression within a structure for it to be considered a proper tensegrity. Most authors dispute this approach as being too restrictive and don't differentiate so long as the original pin-jointed assembly is followed, i.e., loading is still axial. Indeed there are many existing examples of structures and mechanisms that are claimed to be tensegrity systems yet possess joints between multiple compression elements. To address this issue, the Skelton Structural Systems and Control Lab introduced the following classification scheme, which has become widely adopted within the field:

> A class k tensegrity Structure is a stable equilibrium of axially loaded elements, with a maximum of k compressive members connected at the node(s). [45]

The classification distinguishes tensegrities by the maximum number of compressive members that share a common joint, although the members still cannot be rigidly attached to one another or transmit bending moments.

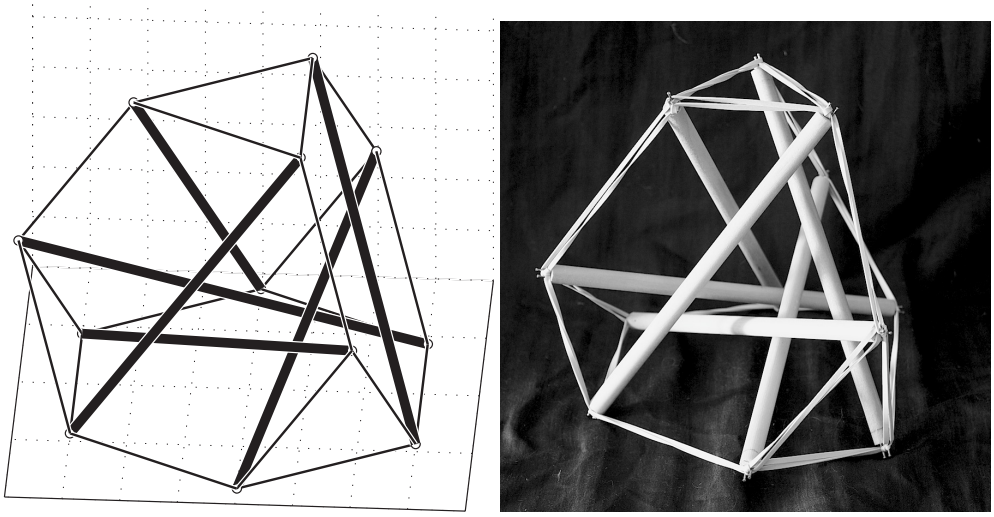

(a) **(b)**

Figure 2.1: Model of the truncated tetrahedron tensegrity. In (a) the model's formation configuration is a regular geometric shape while in (b) a physical model is shown in a deformed static equilibrium, i.e., its tensegrity configuration.

2.1.2 Tensegrity Configurations

To achieve a stable tensegrity configuration the components of a tensegrity architecture must be in static equilibrium. The connectivity of the components in tensegrity architectures is commonly based on regular polyhedra that possess geometric symmetries. However, after settling into their tensegrity configurations, these architectures are sometimes distorted. As an example, a tensegrity constructed from a truncated tetrahedron is shown in its assembly configuration in Figure 2.1a. A physical model of the same architecture that has reached static equilibrium is shown in Figure 2.1b. It becomes clear from the photograph that the positions of the tensegrity's nodes are no longer located at the corners of an easily described solid. This deformation is due partly to inaccuracies of the construction (e.g., elastics having different stiffness or struts having different lengths) but is also caused by the structure's components shifting to minimize the potential energy of the system.

The process of finding stable configurations of tensegrity architectures has been of significant interest in literature. Referred to as form-finding, the problem is generally approached in one of two ways: kinematically or stati-

cally. Kinematically, the problem can be solved by finding minimal compatible lengths of some or all of the tensile members while holding the lengths of the compressive members constant. Conversely, the length of some, or all, of the compressive members can be maximized while holding the tensile members to constant lengths. This can be visualized as pulling cables, or extending struts, until the structure erects itself, a useful property that has been exploited to develop deployable structures [26]. The statics approach to the problem is solved by finding the static equilibrium configurations of predetermined assemblies, i.e., with specified component lengths. Several extensive reviews of the most common form-finding methods have been written and are recommended for further reference [46–48].

Equilibrium configurations can be calculated analytically for simpler tensegrity structures. However, analytical solutions become difficult, if not impossible, for complex architectures that contain larger quantities of components. Recent literature has focused on numerical form-finding methods for use with complex tensegrities. These are primarily computationally expensive methods, such as a Monte Carlo "shotgun" approach [49] and genetic algorithms [50], although some newer methods also focus on reformulating the problem of form-finding to make it more suitable for automatic generation and solving [47].

2.1.3 Structural Analysis of Tensegrities

To investigate the structural properties of tensegrities, it is helpful to treat them as pin-jointed structures similar to trusses. Despite their similarities, some conventional methods of analyzing pin-jointed structures are not applicable in the case of tensegrity structures [24]. For example, Maxwell's well-known rule to verify whether or not a structure is statically determinate does not adequately take into account some properties of structures that are both statically and kinematically indeterminate,such as tensegrities [51]. The standard form of Maxwell's rule is as follows:

$$N_b + N_k - \mathcal{D}N_j = \mathcal{M} \tag{2.1}$$

where N_b is the number of components in the structure, N_k is the number of kinematic constraints imposed, $\mathcal{D}$ is the dimension of the space being considered ($\mathcal{D} = 2$ for planar structures, $\mathcal{D} = 3$ for spatial ones), N_j is the number of joints and $\mathcal{M}$ is the degree of static indeterminacy.

Pellegrino and Calladine have addressed the limitations of the conventional Maxwell's rule [51–53]. They begin by deriving the following system of linear equations to describe the nodal equilibrium of a pin-jointed structure:

$$\mathbf{At} = \mathbf{f} \tag{2.2}$$

The vector $\mathbf{t}$ is comprised of the N_b internal forces, where tension is considered to be positive and compression negative. These internal forces are related linearly to the net external forces applied at each node by the $(\mathcal{D}N_j) \times N_b$ equilibrium matrix $\mathbf{A}$, which is constructed based on the geometry and configuration of the structure. The vector $\mathbf{f}$ is comprised of the nodal forces in all $\mathcal{D}$ directions, and at all N_j nodes.

The virtual work principle may be used to develop a similar relationship between nodal displacements and changes in component lengths. Assuming quasi-static conditions, the work done by a set of nodal forces along very small displacements, $\delta\mathbf{d}$, is equal to the work done by the internal tension along compatible component elongations, $\delta\mathbf{e}$. More precisely, the following expression must be true:

$$\mathbf{f}^{\mathrm{T}}\delta\mathbf{d} = \mathbf{t}^{\mathrm{T}}\delta\mathbf{e} \tag{2.3}$$

The nodal equilibrium relationship from Equation 2.2 can be substituted into this relationship for $\mathbf{f}$ to yield the following:

$$(\mathbf{A}\mathbf{t})^{\mathrm{T}}\delta\mathbf{d} = \mathbf{t}^{\mathrm{T}}\delta\mathbf{e} \tag{2.4}$$

$$\mathbf{t}^{\mathrm{T}}\mathbf{A}^{\mathrm{T}}\delta\mathbf{d} - \mathbf{t}^{\mathrm{T}}\delta\mathbf{e} = \mathbf{0} \tag{2.5}$$

$$\mathbf{t}^{\mathrm{T}}\left(\mathbf{A}^{\mathrm{T}}\delta\mathbf{d} - \delta\mathbf{e}\right) = \mathbf{0} \tag{2.6}$$

Ignoring the trivial solution where there are no internal forces (i.e., $\mathbf{t} = \mathbf{0}$), the expression inside the brackets must be equal to zero. Therefore the following linear relationship is defined:

$$\mathbf{A}^{\mathrm{T}}\delta\mathbf{d} = \delta\mathbf{e} \tag{2.7}$$

$$\mathbf{B}\delta\mathbf{d} = \delta\mathbf{e} \tag{2.8}$$

which introduces the compatibility matrix $\mathbf{B}$, equal to $\mathbf{A}^{\mathrm{T}}$, and demonstrates the duality of the equilibrium matrix.

The properties of these matrices are useful in further describing the behaviour of tensegrity structures. Static indeterminacy can be described mathematically by considering the null space of the equilibrium matrix $\mathbf{A}$. If $\mathbf{A}$ is rank deficient, there exists a non-trivial solution, i.e., $\mathbf{t}_0 \neq \mathbf{0}$, to the equation $\mathbf{A}\mathbf{t}_0 = \mathbf{0}$. This corresponds physically to a combination of internal component forces that do not result in any net change of forces at the structure's nodes and thus can be applied while maintaining equilibrium. This is the definition of self-stress and is an important requirement of tensegrity systems.

Similarly, kinematic indeterminacy can be demonstrated by finding the null space of the compatibility matrix $\mathbf{B}$. In this case, if there exists a non-trivial solution, i.e., $\mathbf{d}_0 \neq \mathbf{0}$, to $\mathbf{B}\mathbf{d}_0 = \mathbf{0}$ the structure is kinematically indeterminate. Physically, such a solution would represent certain modes of nodal

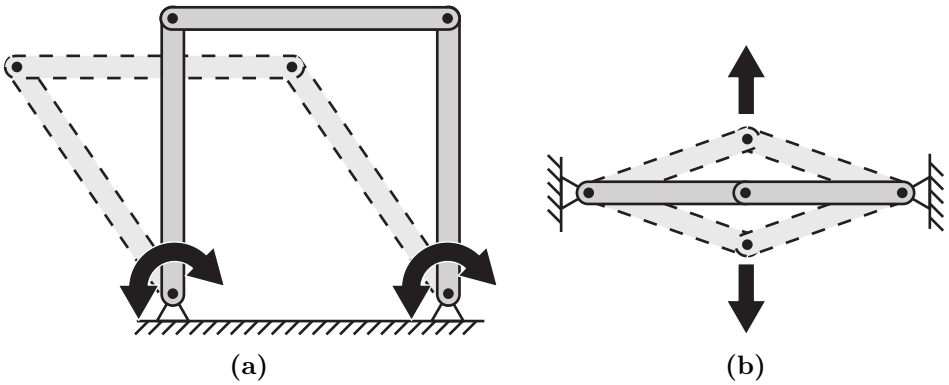

Figure 2.2: Example inextensible mechanisms of kinematically indeterminate structures. The infinitesimal mechanism in (b) has been exaggerated to improve clarity.

displacements that can occur without any changes to the component lengths. Rigid body motion of the whole structure will be included in these modes but may be removed through the addition of proper kinematic constraints. The remaining modes of displacements are defined as inextensible mechanisms. These mechanisms can be finite, such as the free rotation of the links within an unactuated four bar assembly like that shown in Figure 2.2a. They can also be infinitesimal, such as the infinitesimal motions that will be experienced by the assembly shown in Figure 2.2b. Infinitesimal displacements are typically resisted by the geometric stiffness of a structure and the original configuration, although not rigid, is stable.

Pellegrino and Calladine introduce two parameters to summarize the above work. First is the quantity of prestress states, or equivalently the degree of static indeterminacy. Using the rank of the equilibrium matrix this is defined as:

$$s_S = N_b - \text{rank}(\mathbf{A}) \tag{2.9}$$

where s_S is the number of prestress states. The number of inextensible mechanisms is defined as:

$$N_I = \mathcal{D}N_j - \text{rank}(\mathbf{A}) - N_k \tag{2.10}$$

where N_I is the number of inextensible mechanisms. Equations 2.9 and 2.10 are then combined to form an extended Maxwell's rule:

$$s_S - N_I = N_b - \mathcal{D}N_j + N_k \tag{2.11}$$

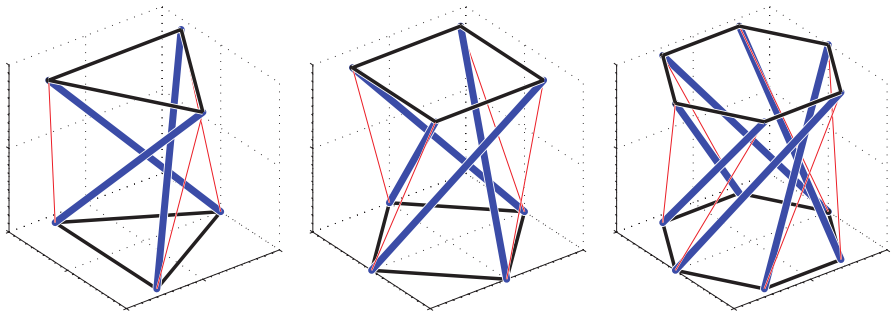

(a) **(b)** **(c)**

Figure 2.3: A selection of structures from the family of tensegrity prisms: the (a) triangular prism, (b) square prism and (c) hexagonal prism. All three are shown in their respective tensegrity configurations.

which becomes the basis of verifying an important requirement of tensegrity; tensegrities must be self-stressing and therefore must have $s_S \geq 1$.

2.2 Architecture Selection

There are a considerable number of tensegrity architectures to choose from when developing a mechanism. Several authors [23, 54, 55] have developed extensive catalogues of tensegrity structures and their respective tensegrity configurations. These architectures have generally been arrived at through trial and error approaches or through the exploration of polyhedra geometries. When generating a mechanism from tensegrity structures it is generally desired to have a limited number of cables and struts. Not only will this reduce the mass of the mechanism, it also allows for potential actuation schemes to be observed more clearly. The simplest and most extensively researched form of tensegrity structure is the family of tensegrity prisms.

2.2.1 Tensegrity Prisms

Tensegrity prisms are formed by two regular n-sided polygon faces connected by n compressive struts and n cables. A small selection of these structures is shown in Figure 2.3.

Due in part to their simple geometry, analytical solutions have been derived for the equilibrium configuration of any regular tensegrity prism [56, 57]. The configurations result in the two polygonal faces remaining parallel to each

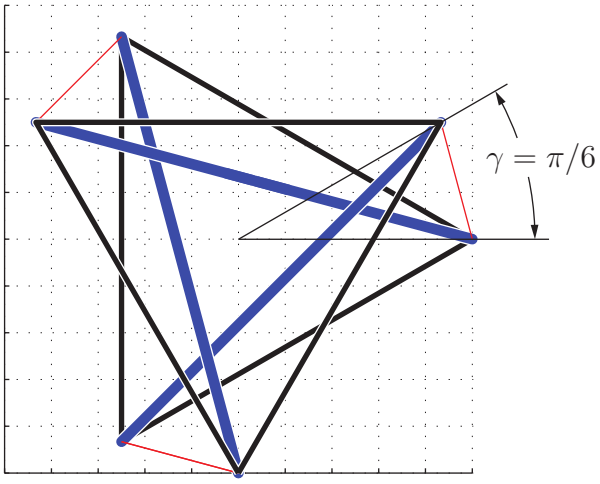

Figure 2.4: Twist angle (γ) of the triangular prism when in tensegrity configuration.

other but rotating slightly about their geometric centres. The angle of this rotation, γ, is dependent only on the number of sides, ε, of the prism's faces as follows:

$$\gamma = \frac{\pi}{2} - \frac{\pi}{\varepsilon} \tag{2.12}$$

This relationship was determined using a force-density form-finding method and is valid so long as the upper or lower polygons are similar to each other and both are regular, i.e., all sides have equal length and all internal angles are equal. The twist angle of the triangular tensegrity prism is shown in Figure 2.4.

All architectures in this family suffer from similar infinitesimal mechanisms (kinematic indeterminacy). This infinitesimal mechanism manifests itself as a screw-like motion of one polygon face with respect to the other. Specifically, the triangular prism tensegrity's infinitesimal mechanism is a rotation about and translation along an axis that is normal to the triangular faces and located at their centroids. Performing a structural analysis of the triangular prism using the methods described in Section 2.1.3 yields the quantities $s_S = N_I = 1$. These calculated values confirm that there exists a single inextensible mechanism and the result agrees with values reported by both Motro [17] and Oppenheim [24]. The exact nature of the inextensible mechanism may be confirmed by calculating the displacement vector that spans the null space of the compatibility matrix $\mathbf{B}$.

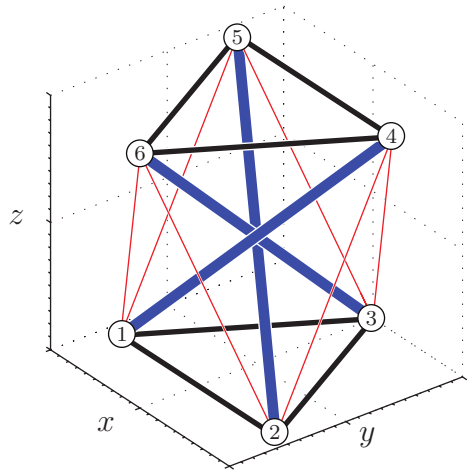

Figure 2.5: The reinforced triangular prism tensegrity structure with nodal definitions.

2.2.2 The Reinforced Triangular Prism

Due to its simpler architecture the triangular prism has already been used as the basis for numerous robot applications. However, the presence of an infinitesimal mechanism is undesirable when adapting the structure into a robotic mechanism. To solve this issue, Knight introduced reinforced versions of tensegrity prisms [27]. Redundant cables are added, as shown in Figure 2.5, resulting in four connections per node instead of the original three. Knight defined and used a quality index of geometric stability to demonstrate that a reinforced 3-strut prism is in stable equilibrium at a twist angle of $\gamma = \pi/3$. At this angle the geometry of a reinforced triangular prism becomes that of a regular antiprism, i.e., the two triangular faces are parallel, mirror images of each other.

The reinforced variant has several interesting improvements over its non-reinforced counterpart and may be explained using the structural analysis techniques discussed earlier. First, unit vectors $\mathbf{n}_{ij}$ are defined along each of the structure's components, where i is the originating node and j is the terminating node, as numbered in Figure 2.5. These unit vectors are used to

generate the equilibrium matrix $\mathbf{A}$ as follows:

$$\mathbf{A} = \begin{bmatrix} \mathbf{n}_{12} & \mathbf{n}_{13} & \mathbf{n}_{14} & \mathbf{n}_{15} & \mathbf{n}_{16} & & & & & & & & & & \\ \mathbf{n}_{21} & & & & & \mathbf{n}_{23} & \mathbf{n}_{24} & \mathbf{n}_{25} & \mathbf{n}_{26} & & & & & & \\ & \mathbf{n}_{31} & & & & \mathbf{n}_{32} & & & & \mathbf{n}_{34} & \mathbf{n}_{35} & \mathbf{n}_{36} & & & \\ & & \mathbf{n}_{41} & & & & \mathbf{n}_{42} & & & \mathbf{n}_{43} & & & \mathbf{n}_{45} & \mathbf{n}_{46} & \\ & & & \mathbf{n}_{51} & & & & \mathbf{n}_{52} & & & \mathbf{n}_{53} & & \mathbf{n}_{54} & & \mathbf{n}_{56} \\ & & & & \mathbf{n}_{61} & & & & \mathbf{n}_{62} & & & \mathbf{n}_{63} & & \mathbf{n}_{64} & \mathbf{n}_{65} \end{bmatrix} \tag{2.13}$$

where the elements of the matrix that contain zeros have been omitted. It should be noted that $\mathbf{n}_{ij} = -\mathbf{n}_{ji}$.The corresponding vector of component tensions becomes:

$$\mathbf{t} = [t_{12}, t_{13}, t_{14}, t_{15}, t_{16}, t_{23}, t_{24}, t_{25}, t_{26}, t_{34}, t_{35}, t_{36}, t_{45}, t_{46}, t_{56}]^{\mathrm{T}} \tag{2.14}$$

where t_{ij} is the internal force between the i and j nodes, with tension being considered positive. The vector of externally applied nodal forces is:

$$\mathbf{f} = [f_{1x}, f_{1y}, f_{1z}, \ldots, f_{6x}, f_{6y}, f_{6z}]^{\mathrm{T}} \tag{2.15}$$

where the net force at each node i is represented by three Cartesian components f_{ix}, f_{iy}, and f_{iz}.

As formulated, the analysis still considers rigid body motions. Sufficient kinematic constraints (i.e., $N_k = 6$) must be introduced to prevent the 3 translations and 3 rotations of the entire structure that are possible in $\mathcal{D} = 3$ dimensional space. Fixing the displacements of node 1 in all three Cartesian directions (i.e., x, y and z) removes the three translational degrees of freedom. Fixing node 2 in the y and z directions removes two more rotational degrees of freedom and restricting node 3 from moving in the z direction removes the final free rotation of the structure. Removing the corresponding rows of the equilibrium matrix (i.e., rows 1–3, 5, 6 and 9) and nodal force vector enforces the six kinematic constraints. The matrix $\mathbf{A}$ now has 12 rows and 15 columns.

The elements of the unit vectors $\mathbf{n}_{ij}$ are populated based on the tensegrity configuration of the reinforced prism and substituted into Equation 2.13. From examination it is found that the rank of $\mathbf{A}$ will remain equal to 12, so long as the end-effector and base triangles are not coplanar. Using Equation 2.9 the number of states of self-stress is found to be:

$$s_S = N_b - \mathrm{rank}(\mathbf{A}) = 15 - 12 = 3 \tag{2.16}$$

This reveals that the reinforced triangular prism has 3 states of self-stress instead of the single state of the plain triangular prism. As such, more components will need to be prestressed for the structure to be stable. Using

Equation 2.10, the number of infinitesimal mechanisms is found to be:

$$N_I = \mathcal{D}N_j - \text{rank}(\mathbf{A}) - N_k = 3 \cdot 6 - 12 - 6 = 0 \tag{2.17}$$

This shows that the infinitesimal mechanism found in the triangular prism has been eliminated via the addition of the extra cables.

2.3 Adaptation to Mechanism

So far in this work the tensegrity concept has only been treated as a structural concept. Generating a useful mechanism from the chosen architecture amounts to finding a strategic actuation scheme to control the geometry of the structure. Large elongations of a tensegrity's components are possible and could generate useful movement of a point or a rigid body in the structure that is defined as the mechanism's end-effector. The process of adapting the reinforced-triangular prism tensegrity into a mechanism will now be discussed.

2.3.1 Mechanism Definition

As shown in Figure 2.5, the reinforced-triangular prism tensegrity is comprised of three compressive members and twelve tensile members. To conform more closely to the notation used in robot manipulator analysis, the numbered node system will be redefined as shown in Table 2.1.

The tensile members between the bottom three nodes (A_i, $i = 1, 2, 3$) are considered to have constant lengths and be perfectly inextensible. This assumption, along with the kinematic constraints introduced to eliminate rigid body motions of the entire system, will effectively fix these nodes to the mechanism's base. As such, the three tensile members connecting these nodes are no longer of interest and may now be ignored. Applying the same assumptions to the tensile members between the three top nodes (B_i) fixes them with respect to each other. Both the top and bottom sets of nodes will form congruent equilateral triangles, defined by the radius, r_b, of their circumscribed circles.

Furthermore, the joints that attach the end-effector members to the rest of the members are considered perfectly spherical, i.e., they will not transmit any torques. In this case the three tensile components connecting the B_i nodes may be replaced with a single rigid plate. Substituting a plate for the tensile components does not violate the definition of tensegrity; the assembly will still be a class-1 tensegrity structure. Three compressive members remain, joining nodes A_1B_1, A_2B_2 and A_3B_3, along with six tensile members, joining nodes A_1B_2, A_1B_3, A_2B_1, A_2B_3, A_3B_1 and A_3B_2.

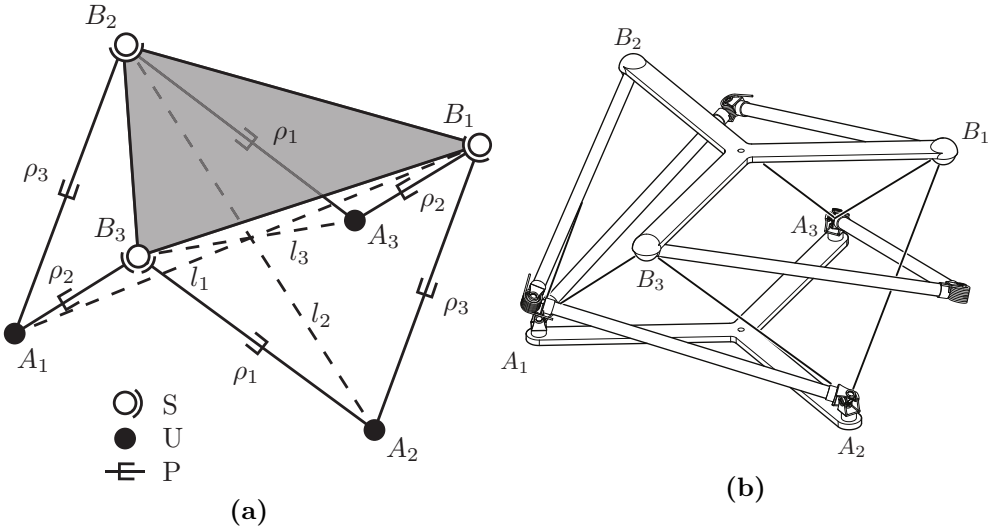

Figure 2.6: The (a) simplified kinematic geometry and (b) conceptual CAD model of the reinforced triangular prism tensegrity mechanism.

2.3.2 Actuation Scheme

The lengths of the tensile members joining the base and end-effector of the mechanism will be actuated. Winch-actuated cables are used to benefit from a large range of motion and the use of stationary actuators that will reduce the inertia of the system. Cables can be flexible enough to act as joints themselves, eliminating the need to place multiple mechanical joints concentrically at all of the nodes. Based on their flexibility, the six cables between the end-effector and base triangles will be treated as universal-prismatic-spherical (U-P-S) linkages, as shown in Figure 2.6a. Each cable will be terminated where it is attached to the end-effector, routed through the centre of the base nodes and actuated by a motorized winch below the base.

The well-known Chebyshev-Grübler-Kutzbach mobility formula [58] may be applied to the simplified kinematic geometry of the mechanism to produce

Table 2.1: Naming convention used for mechanism nodes

Structure Node Number	1	2	3	4	5	6
Mechanism Node Name	A_1	A_2	A_3	B_1	B_2	B_3

the following result:

$$M = 6(N_b - N_j - 1) + \sum_{i=1}^{N_j} \mathcal{D}_i = 6(14 - 18 - 1) + 36 = 6 \tag{2.18}$$

where M is the mobility of the mechanism and $\mathcal{D}_i$ is the total degrees-of-freedom allowed by the i-th joint (i.e., 1 for prismatic or revolute joints, 2 for universal and 3 for spherical). With six degrees of mobility and no infinitesimal mechanisms, the pose of the end-effector of the reinforced triangular prism will be fully controlled by actuating the length of the six cables. This result does however require the cables to remain taut and not experience sag so that they may be treated as prismatic actuators.

The development of the mechanism's architecture is based on the desire to reduce the inertia of the moving parts, to simplify actuation, and to generate pure translational motion of the end-effector. To this effect, one may observe the occurrence of the three parallelograms, $A_1A_2B_1B_2$, $A_2A_3B_2B_3$, and $A_3A_1B_3B_1$, formed by the mechanism's elements and demonstrated in Figure 2.7. The arrangement of these parallelograms presents an opportunity to ensure that the movement of the end-effector triangle is only translational. If the cables remain taut and are actuated in the pairs shown in Table 2.2, the end-effector will be forced to remain parallel to the ground. Length actuation of the cables could be achieved by using a single motorized winch to drive each pair of cables (total of three winches), further simplifying the mechanism's architecture.

2.3.3 Application of Prestress

In addition to its novel actuation scheme, this mechanism differs from existing tensegrity mechanisms based on the reinforced triangular prism [34, 35] in the way it is prestressed. Equation 2.16 shows that the structure has three states of self-stress, which could be applied by replacing some components with force elements.

Table 2.2: Actuated pairs of cables

Length	Cable Pair
ρ_1	A_2B_3, A_3B_2
ρ_2	A_1B_3, A_3B_1
ρ_3	A_1B_2, A_2B_1

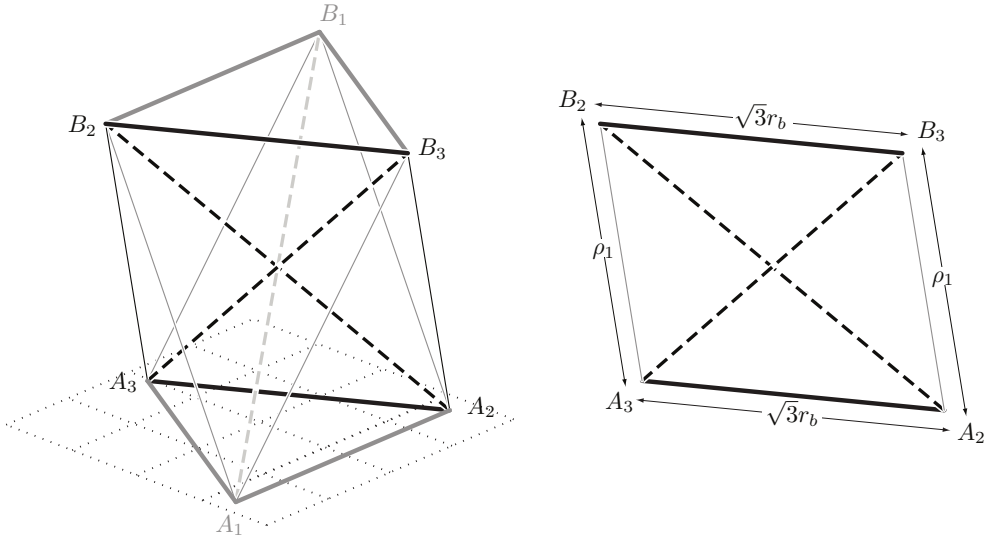

Figure 2.7: Location of the parallelogram $A_2B_3B_2A_3$ with respect to the rest of the mechanism.

Any subset of three components could be used if their associated columns in the equilibrium matrix are linearly independent (see Equation 2.13). The tension components are a poor selection since replacing them with springs or force actuating them would conflict with the chosen actuation scheme. Alternatively, the three compression members, which are linearly independent so long as the end-effector and base do not become coplanar, will be replaced with compression springs. This particular architecture is beneficial for its ability to automatically find tensegrity configurations since, given a set of fixed cable lengths, it will naturally deform to a stable configuration to minimize its potential energy.

Attempting to physically implement this mechanism is difficult due to the mechanical interference of the compressive elements at their respective midpoints. This interference occurs for the same reason that the end-effector remains in translation, i.e., the existence of parallelograms in the architecture. As seen in Figure 2.7 the compression components lie on the diagonals of the parallelograms, which will always intersect each other. To overcome this issue, each compression component is replaced with a non-interfering spring linkage, shown in Figure 2.8. The linkage design incorporates two rigid links of length $l_0/2$ that are connected to each other via a revolute joint at node C_i. A torsion spring is located at this revolute joint and applies a torque between the upper and lower links, acting to fully extend the two rigid links. As a

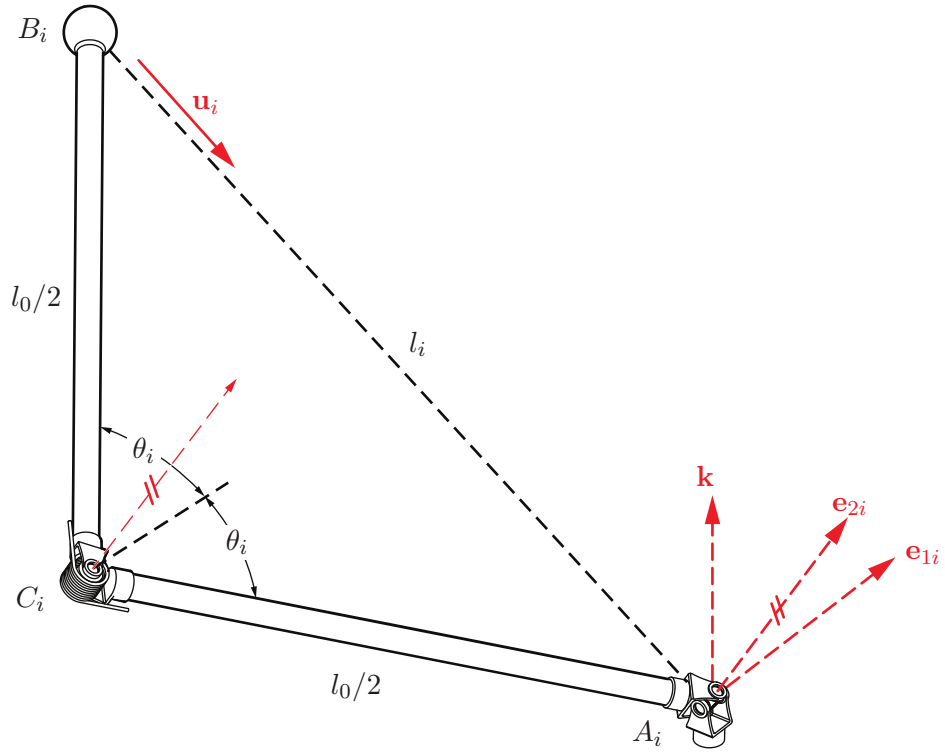

Figure 2.8: Illustration of the proposed compression spring linkage.

result, the linkage will act as a "virtual" compression spring, albeit with a nonlinear force-deflection relationship.

Each spring linkage is attached to the base with a universal joint, which must be designed while considering the issue of mechanical interference between linkages. The first axis of the universal joint, $\mathbf{e}_{1i}$, is defined to be orthogonal to both the line $\overline{OA_i}$ and the vertical z-axis:

$$\mathbf{e}_{1i} = \frac{\mathbf{k} \times \mathbf{a}_i}{||\mathbf{k} \times \mathbf{a}_i||} \tag{2.19}$$

where $\mathbf{a}_i$ is a vector locating the base node with respect to the centre of the base triangle. Meanwhile, the second joint axis $\mathbf{e}_{2i}$ is parallel to the axis of the torsion spring revolute joint:

$$\mathbf{e}_{2i} = \frac{\mathbf{u}_i \times \mathbf{e}_{1i}}{||\mathbf{u}_i \times \mathbf{e}_{1i}||} \tag{2.20}$$

where $\mathbf{u}_i$ is a unit vector describing the direction of the line segment between nodes B_i and A_i. This choice of joint axes constrains each set of links to act

only within a plane, referred to as the linkage's plane-of-action, which always has its normal vector parallel to $\mathbf{e}_{2i}$. The reasoning behind this selection of joint axes is two-fold. The universal joint will prevent any rotation of the linkage along the A_iB_i axis, simplifying the kinematics of the mechanism. It will also resist the moment that is generated about that axis by the offset weight of the links and torsion spring.

The deflection of the torsion spring joint is described using the half angle, θ_i, between the two links, defined as:

$$\theta_i = \arcsin\left(\frac{l_i}{l_0}\right) \tag{2.21}$$

where the length l_0 can be chosen to reduce interferences between links and the actuated cables. The design theoretically allows the virtual spring to achieve a full range of motion, $l_i \in [0, l_0]$, potentially maximizing the size of the mechanism's workspace. Mechanical interferences between cables and links is investigated in greater depth in Chapter 3.

3 Kinematic Analysis

In this chapter the movement of the reinforced triangular tensegrity mechanism is analyzed. The translational motion of the mechanism will be confirmed by minimizing its potential energy. This optimization is constrained by the actuated cable lengths and must be solved using numeric methods. More convenient analytical solutions to the position and velocity-level kinematics are presented based on several assumptions made about the mechanism's geometry and the cable tensions. The occurrence of singularities and their impact on the mechanism's kinematics are discussed briefly. A simple and efficient method of checking for mechanical interference between the mechanism's components is presented. Finally, the kinematic boundaries of the mechanism's workspace are summarized and presented.

3.1 Position-Level Kinematics

The direct kinematic problem (DKP) is the task of calculating the pose of the mechanism, defined as the position and orientation of the end-effector triangle, when provided with a set of known actuated cable lengths. Solving the DKP of this particular mechanism is directly analogous to the task of tensegrity form-finding. Similar to the static form-finding methods discussed in Section 2.1.2, it is possible to minimize the potential energy within the mechanism to determine its equilibrium configuration.

This optimization problem is subject to the constraints imposed by the six actuated cables. The cables will technically pose inequality constraints since they cannot exceed their actuated lengths but may become slack, i.e., $\rho \in [0, \rho_{max}]$. However, only configurations where tension is maintained and the mechanism is fully defined by the length of its cables are of interest. Equality constraints are therefore used instead. The exercise of confirming that cable tension is maintained is left to Chapter 4.

A reduced set of generalized coordinates must be chosen to fully describe

the configuration of the mechanism. The base nodes, A_i, where $i = 1, 2, 3$, are already completely kinematically constrained and do not contribute any degrees of freedom to the mechanism. Additionally, the end-effector nodes, B_i, are all considered to be located on a rigid body. Thus the configuration of the mechanism and the lengths of all of its components can be completely defined using only the position and orientation of the end-effector. The global reference frame, XYZ, used to describe the motion of the mechanism is shown in Figure 3.1. It is located at point O, the centroid of the base triangle, with the X axis aligned with the line between nodes A_1 and A_2, the Y axis passing through node A_3, and the Z axis normal to the plane formed by nodes $A_1A_2A_3$. Within this reference frame, the A_i nodes are located by the following vectors:

$$\mathbf{a}_1 = \frac{r_b}{2}\begin{bmatrix}-\sqrt{3}\\-1\\0\end{bmatrix} \qquad \mathbf{a}_2 = \frac{r_b}{2}\begin{bmatrix}\sqrt{3}\\-1\\0\end{bmatrix} \qquad \mathbf{a}_3 = \frac{r_b}{2}\begin{bmatrix}0\\1\\0\end{bmatrix} \tag{3.1}$$

where r_b is the radius of the circle circumscribed by the base and end-effector triangles, e.g., the distance $||OA_i||$. The base and end-effector triangles must both be congruent and equilateral and therefore share the same value of r_b. This radius may be used as a scaling factor to alter the size of the mechanism.

The centroid of the mechanism's end-effector triangle, P, is located in the XYZ frame by the position vector $\mathbf{p} = [x, y, z]^{\mathrm{T}}$. A body-fixed reference frame, $X'Y'Z'$, is attached to the end-effector at point P and is initially aligned with frame XYZ as shown in Figure 3.1. Within the $X'Y'Z'$ frame, the three nodes of the end-effector, B_i, are located by the following vectors:

$$\mathbf{b}'_1 = \frac{r_b}{2}\begin{bmatrix}\sqrt{3}\\1\\0\end{bmatrix} \qquad \mathbf{b}'_2 = \frac{r_b}{2}\begin{bmatrix}-\sqrt{3}\\1\\0\end{bmatrix} \qquad \mathbf{b}'_3 = \frac{r_b}{2}\begin{bmatrix}0\\-1\\0\end{bmatrix} \tag{3.2}$$

There is not yet any proof that the end-effector body will experience translational motion and, as such its orientation must be taken into consideration. While numerous methods of representing orientation exist, the end-effector orientation can be conveniently represented using Euler angles in this case. Euler angles are a set of three successive rotations about predefined axes that represent the orientation of an object with respect to a fixed reference frame. If the end-effector remains in translation as speculated, the actual values of these angles are not of interest since they should all be found to equal zero. Therefore an arbitrary Euler convention may be selected, so long as consecutive axes of rotation are orthogonal. In this case the angles φ, χ, and ψ will be used to represent rotations about the body-fixed X', Y', and Z' axes, respectively. These rotations are represented by the following rotation matrices:

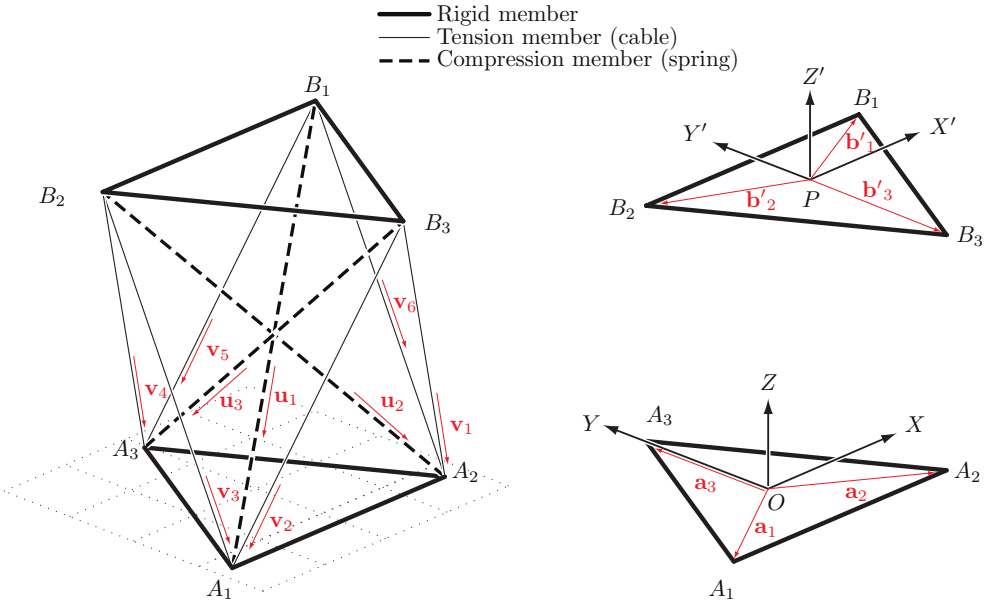

Figure 3.1: A vector representation of the mechanism, displaying the reference frames used and the unit vectors that describe direction of its components.

$$\mathbf{Q}_\varphi = \begin{bmatrix} 1 & 0 & 0 \\ 0 & \mathrm{c}\varphi & -\mathrm{s}\varphi \\ 0 & \mathrm{s}\varphi & \mathrm{c}\varphi \end{bmatrix} \qquad \mathbf{Q}_\chi = \begin{bmatrix} \mathrm{c}\chi & 0 & \mathrm{s}\chi \\ 0 & 1 & 0 \\ -\mathrm{s}\chi & 0 & \mathrm{c}\chi \end{bmatrix} \qquad \mathbf{Q}_\psi = \begin{bmatrix} \mathrm{c}\psi & -\mathrm{s}\psi & 0 \\ \mathrm{s}\psi & \mathrm{c}\psi & 0 \\ 0 & 0 & 1 \end{bmatrix}$$

where the shorthand $\mathrm{s}\varphi$, $\mathrm{c}\varphi$, etc. have been used in place of $\sin(\varphi)$, $\cos(\varphi)$, etc. for brevity. The individual matrices are post-multiplied:

$$\mathbf{Q} = \mathbf{Q}_\varphi \mathbf{Q}_\chi \mathbf{Q}_\psi \tag{3.3}$$

which generates the overall rotation matrix $\mathbf{Q}$ that describes the orientation of the end-effector.

The position of the end-effector nodes that are currently located in the body-fixed frame can now be expressed in the global reference frame by the vectors $\mathbf{b}_i$ as follows:

$$\mathbf{b}_i = \mathbf{p} + \mathbf{Q}\mathbf{b}'_i, \qquad i = 1, 2, 3 \tag{3.4}$$

where $\mathbf{b}'_i$ is the vector locating the end-effector nodes with respect to the centre of mass. The configuration of the mechanism is thus fully defined by

the three end-effector position coordinates along with the three Euler angles. These variables will be combined into the following vector $\mathbf{x}$ for simplicity:

$$\mathbf{x} = [x, y, z, \varphi, \chi, \psi]^{\mathrm{T}} \tag{3.5}$$

3.1.1 Numerical Solution to the Direct Kinematic Problem

The mechanism's DKP may now be solved using constrained optimization. The objective function to be minimized is defined as the potential energy of the system and is constrained by the actuated cable lengths. Only the energy contained within the three torsion spring linkages will be considered; the effect of external forces and gravity will be considered later in Chapter 4.

The length of each virtual spring, l_i, can be found using a vector loop closure approach:

$$-l_i\mathbf{u}_i = \mathbf{p} + \mathbf{Q}\mathbf{b}'_i - \mathbf{a}_i \tag{3.6}$$

$$l_i^2 \cancelto{1}{\mathbf{u}_i^{\mathrm{T}}\mathbf{u}_i} = \left(\mathbf{p} + \mathbf{Q}\mathbf{b}'_i - \mathbf{a}_i\right)^{\mathrm{T}}\left(\mathbf{p} + \mathbf{Q}\mathbf{b}'_i - \mathbf{a}_i\right)$$

$$l_i = \sqrt{\left(\mathbf{p} + \mathbf{Q}\mathbf{b}'_i - \mathbf{a}_i\right)^{\mathrm{T}}\left(\mathbf{p} + \mathbf{Q}\mathbf{b}'_i - \mathbf{a}_i\right)} \qquad i = 1, 2, 3 \tag{3.7}$$

where $\mathbf{u}_i$ is a unit vector directed along the ith virtual spring axis, as shown in Figure 2.8 and Figure 3.1. The deflection angle, θ_i, of each torsion spring has already been derived in Equation 2.21. Assuming that the springs behave linearly and are at rest when $\theta_i = \theta_0 = \pi/2$ (i.e., when the legs are fully extended), the potential energy within each torsion spring is equal to:

$$U_i = \frac{1}{2}\kappa(2\theta_i - \pi)^2 \tag{3.8}$$

where κ is the torsional stiffness and is assumed to be the same for all of the springs. Equations 2.21, 3.7 and 3.8 can be combined to give an expression for the total potential energy, U, of the system:

$$U = \frac{1}{2}\kappa \sum_{i=1}^{3} \left[2\arcsin\left(\frac{\sqrt{\left(\mathbf{p} + \mathbf{Q}\mathbf{b}'_i - \mathbf{a}_i\right)^{\mathrm{T}}\left(\mathbf{p} + \mathbf{Q}\mathbf{b}'_i - \mathbf{a}_i\right)}}{l_0} \right) - \pi \right]^2 \tag{3.9}$$

A vector loop closure approach may also be used to generate the kinematic constraints posed by the six cables. If the cables are actuated in the pairs

shown in Table 2.2, the six constraint functions ϕ_j, $j = 1, \ldots, 6$ are:

$$\phi_1 = (\mathbf{p} + \mathbf{Q}\mathbf{b}'_3 - \mathbf{a}_2)^{\mathrm{T}}(\mathbf{p} + \mathbf{Q}\mathbf{b}'_3 - \mathbf{a}_2) - \rho_1^2 = 0 \tag{3.10}$$

$$\phi_2 = (\mathbf{p} + \mathbf{Q}\mathbf{b}'_2 - \mathbf{a}_3)^{\mathrm{T}}(\mathbf{p} + \mathbf{Q}\mathbf{b}'_2 - \mathbf{a}_3) - \rho_1^2 = 0 \tag{3.11}$$

$$\phi_3 = (\mathbf{p} + \mathbf{Q}\mathbf{b}'_3 - \mathbf{a}_1)^{\mathrm{T}}(\mathbf{p} + \mathbf{Q}\mathbf{b}'_3 - \mathbf{a}_1) - \rho_2^2 = 0 \tag{3.12}$$

$$\phi_4 = (\mathbf{p} + \mathbf{Q}\mathbf{b}'_1 - \mathbf{a}_3)^{\mathrm{T}}(\mathbf{p} + \mathbf{Q}\mathbf{b}'_1 - \mathbf{a}_3) - \rho_2^2 = 0 \tag{3.13}$$

$$\phi_5 = (\mathbf{p} + \mathbf{Q}\mathbf{b}'_2 - \mathbf{a}_1)^{\mathrm{T}}(\mathbf{p} + \mathbf{Q}\mathbf{b}'_2 - \mathbf{a}_1) - \rho_3^2 = 0 \tag{3.14}$$

$$\phi_6 = (\mathbf{p} + \mathbf{Q}\mathbf{b}'_1 - \mathbf{a}_2)^{\mathrm{T}}(\mathbf{p} + \mathbf{Q}\mathbf{b}'_1 - \mathbf{a}_2) - \rho_3^2 = 0 \tag{3.15}$$

where ρ_i are the actuated cable lengths. Finally, the optimization problem may be formally posed:

$$\begin{aligned} \underset{\mathbf{x}}{\text{minimize}} \quad & U(\mathbf{x}) \\ \text{subject to} \quad & \phi_j(\mathbf{x}) = 0; \quad j = 1, \ldots, 6 \end{aligned}$$

The field of optimization offers many approaches to solving problems that are subject to multiple constraints. If the cable constraints were represented by inequality constraints, as originally suggested, penalty function, barrier function or gradient free methods could be used to perform the optimization [59]. However, since the cable constraints are being treated as equalities, it is possible to use a Lagrangian multiplier method instead.

To satisfy equality constraints, a constrained extrema (minimum or maximum) must be located on the point, line, plane, surface, etc., defined by the constraint functions. Furthermore, if a compatible extrema exists, it must be in a level set of the objective function that is tangent to the constraint functions [59]. In other words, the gradient of the objective function will be parallel to the gradient of the constraint function at an extrema, although they are not necessarily of equal magnitude. This can also be written as:

$$\nabla_{\mathbf{x}} f(\mathbf{x}) = \lambda \nabla_{\mathbf{x}} g(\mathbf{x}) \tag{3.16}$$

where $\nabla_{\mathbf{x}}$ is the gradient operator with respect to $\mathbf{x}$, $f(\mathbf{x})$ is an arbitrary objective function, $g(\mathbf{x})$ is a constraint function, and λ is known as a Lagrange multiplier. A unique multiplier for each of the constraint functions is introduced and used to create the Lagrangian function $\mathcal{L}$, where:

$$\mathcal{L} = f(\mathbf{x}) - \sum \lambda g(\mathbf{x}) \tag{3.17}$$

The goal is now to locate a stationary point, i.e., a point where all partial derivatives of the Lagrangian function are zero that still satisfies all of the constraint functions.

In the case of minimizing the potential energy of the tensegrity mechanism, the Lagrangian function is:

$$\mathcal{L} = U(\mathbf{x}) - \sum_{j=1}^{6} \lambda_j \phi_j(\mathbf{x}) \tag{3.18}$$

The functions partial derivative with respect to $\mathbf{x}$ must satisfy $\nabla_{\mathbf{x}}\mathcal{L} = \mathbf{0}$ and the constraint equations (Equations 3.10-3.15) must also be satisfied. The constraint equations can be included together or derived from the Lagrangian function by taking the partial derivative with respect to the vector of Lagrangian multipliers, $\boldsymbol{\lambda}$. The resulting twelve multivariate equations may be written more concisely as:

$$\mathbf{h}(\mathbf{x}^*) = \begin{Bmatrix} \nabla_{\mathbf{x}}\mathcal{L} \\ \nabla_{\boldsymbol{\lambda}}\mathcal{L} \end{Bmatrix} \tag{3.19}$$

where

$$\mathbf{x}^* = [x, y, z, \varphi, \chi, \psi, \lambda_1, \ldots, \lambda_6] \tag{3.20}$$

As there are twelve unknown variables (the six elements of the mechanism's configuration variable $\mathbf{x}$ and the six Lagrangian multipliers) the system of equations should be solvable. However, the resulting equations are highly non-linear and arriving at an analytical solution is not possible. Instead the well known numerical Newton-Raphson method will be used.

The Newton-Raphson method is based on a first order Taylor series expansion of a function [59]:

$$\mathbf{h}(\mathbf{x}_o^* + \Delta\mathbf{x}^*) \approx \mathbf{h}(\mathbf{x}_o^*) + \Delta\mathbf{x}^*\boldsymbol{\Gamma}(\mathbf{x}_0^*) \tag{3.21}$$

where an initial guess $\mathbf{x}_o^*$ is required to begin an iterative search for a solution where the value of the function to be solved is zero. The matrix $\boldsymbol{\Gamma}$ is the partial derivative of function $\mathbf{h}$ with respect to the vector $\mathbf{x}^*$, i.e., :

$$\boldsymbol{\Gamma}(\mathbf{x}_0^*) = \left.\frac{\partial \mathbf{h}}{\partial \mathbf{x}^*}\right|_{\mathbf{x}^*=\mathbf{x}_o^*} \tag{3.22}$$

It can be used to calculate the magnitude and direction of each iterative step toward the potential solution as follows:

$$\begin{aligned} \mathbf{h}_o + \boldsymbol{\Gamma}(\mathbf{x}_o^*)\Delta\mathbf{x}^* &= \mathbf{0} \\ \boldsymbol{\Gamma}(\mathbf{x}_o^*)\Delta\mathbf{x}^* &= -\mathbf{h}_o \\ \Delta\mathbf{x}^* &= -\boldsymbol{\Gamma}(\mathbf{x}_o^*)^{-1}\mathbf{h}_o \end{aligned} \tag{3.23}$$

where $\mathbf{h}_0 = \mathbf{h}(\mathbf{x}_0^*)$ is the function evaluated at $\mathbf{x}^* = \mathbf{x}_0^*$. Using Equation 3.23 successive estimates are obtained by calculating $\Delta\mathbf{x}^*$ and adding it to the current estimate. This process is repeated until the change in $\mathbf{x}^*$ is sufficiently small (i.e., $||\Delta\mathbf{x}^*|| \leq \epsilon_{\text{tol}}$) and the solution is considered to have converged.

When applying numerical methods there is always a possibility that the solution will not converge. To assist with convergence, a continuation approach as described by Arsenault and Gosselin [35] or Tsai [1] is used. The approach divides the DKP into multiple sub-problems, i.e., calculating the mechanism's configuration from several intermediate sets of inputs. These intermediate sets of inputs are formed by discretizing a vector between an input set that is known to produce a certain mechanism configuration and the original input set that is in question. The Newton-Raphson algorithm is still applied to each of these sub-problems, with the calculated configuration of each set being used as the initial guess of the next sub-problem. Finer discretization improves the solution stability by avoiding extremely large iteration steps that may arise from steep gradients.

An analytically derived version of Equation 3.19 and its Jacobian matrix were imported into a MATLAB (The MathWorks, Inc., Natick, MA, USA) script and a function was written to perform the iterative Newton-Raphson procedure. The procedure converged to solutions quickly (within 10 iterations per sub-problem) for an example mechanism defined by $r_b = 1$ and using a convergence tolerance of $\epsilon_{\text{tol}} = 0.001$. The fast convergence is likely due to the quadratic nature of the potential energy function. The exercise was repeated for numerous sets of inputs and in all of those tested, the three Euler angles were found to be approximately zero. This indicates that the end-effector rotation remains roughly constant and suggests that equilibrium configurations of the mechanism will result in translational behaviour when cable tension is maintained.

3.1.2 Analytical Solution to the Direct Kinematic Problem

Conducting a numerical optimization every time the DKP needs to be solved is computationally inefficient, especially if it can be shown that the cables are always in tension, or at least remain taut in a well defined subset of the reachable workspace. Instead, a second analysis of the mechanism, assuming taut cables, is performed to obtain analytical solutions that are faster to compute. The satisfying conditions of this assumption will be verified later in Chapter 4.

The presence of the parallelograms discussed in Section 2.3.2, prevents any rotation of the end-effector when all cables are taut. If the end-effector orientation is constant, the rotation matrix $\mathbf{Q}$ is equal to the 3×3 identity

matrix and it is observed that $\mathbf{b}_i = -\mathbf{a}_i$. Additionally, the sum of any two of the $\mathbf{a}_i$ vectors is equal to the negative of the third, e.g., $\mathbf{a}_1 + \mathbf{a}_2 = -\mathbf{a}_3$. Using either Equations 3.10, 3.12, 3.14 or Equations 3.11, 3.13, 3.15, the constraints imposed by the actuator lengths are found to be:

$$\rho_i^2 = (\mathbf{p} + \mathbf{a}_i)^{\mathrm{T}}(\mathbf{p} + \mathbf{a}_i), \qquad i = 1, 2, 3 \tag{3.24}$$

where it is recognized that Equation 3.24 is an expression for three spheres of radii ρ_i centred at $-\mathbf{a}_i$. Therefore, solving for $\mathbf{p}$ is analogous to finding the intersection of those spheres. Expanding Equation 3.24 leads to a general expression for the length of cable i in terms of components of the unknown position vector $\mathbf{p}$ and the components of the known vectors $\mathbf{a}_i$ as follows:

$$\rho_i^2 = \mathbf{p}^{\mathrm{T}}\mathbf{p} + 2\mathbf{p}^{\mathrm{T}}\mathbf{a}_i + \mathbf{a}_i{}^{\mathrm{T}}\mathbf{a}_i = x^2 + y^2 + z^2 + 2xa_{i_x} + 2ya_{i_y} + a_{i_x}^2 + a_{i_y}^2 \tag{3.25}$$

Expanding and solving Equation 3.25 for x, y, and z yields:

$$x = \frac{\sqrt{3}(\rho_2^2 - \rho_1^2)}{6r_b} \tag{3.26}$$

$$y = \frac{(2\rho_3^2 - \rho_2^2 - \rho_1^2)}{6r_b} \tag{3.27}$$

$$z = \pm\frac{\sqrt{\rho_1^2\rho_2^2 + \rho_2^2\rho_3^2 + \rho_3^2\rho_1^2 - \rho_1^4 - \rho_2^4 - \rho_3^4 + 3r_b^2(\rho_1^2 + \rho_2^2 + \rho_3^2 - 3r_b^2)}}{3r_b} \tag{3.28}$$

which is the analytical solution to the DKP.

Despite the existence of two solutions to the DKP for every set of inputs $\boldsymbol{\rho}$, one of the solutions corresponds to a configuration above the XY plane and the other corresponds to the mirrored configuration below the XY plane. Only one of these configurations would be possible for a physical model of the mechanism to achieve without a collision occurring between the base and end-effector. Therefore any solution with a negative z value may simply be ignored making the solution to the DKP effectively a one-to-one mapping between the actuator space and Cartesian space.

3.1.3 Analytical Solution to the Inverse Kinematic Problem

The inverse kinematic problem (IKP) is the task of calculating the cable lengths, $\boldsymbol{\rho}$, required to achieve a given position of the mechanism's end-effector, $\mathbf{p}$. Similar to other parallel mechanisms, the process of solving the IKP for this mechanism is relatively straightforward. Given the position of the end-effector platform and assuming zero rotation of the end-effector, the location

of points B_i are known and the same vector loops used in the DKP can be used to determine the lengths of each cable pair. Taking the square root of Equation 3.24 gives

$$\rho_i = \sqrt{(\mathbf{p}+\mathbf{a}_i)^{\mathrm{T}}(\mathbf{p}+\mathbf{a}_i)}, \qquad i = 1,2,3 \tag{3.29}$$

which is the solution to the IKP.

3.2 Mechanism Jacobians and Singularity Analysis

Continuing with the assumption of maintained cable tension, the velocity-level kinematics are now addressed. The goal is to describe the relationships that exist between the joint velocities, i.e., the rates of change of the cable lengths, and the Cartesian velocity of the end-effector. Knowledge of these relationships is essential when planning paths that the end-effector will take to travel between two or more desired poses. The time derivative of Equation 3.24 leads to:

$$\rho_i\dot{\rho}_i = (\mathbf{p}+\mathbf{a}_i)^{\mathrm{T}}\dot{\mathbf{p}}, \qquad i = 1,2,3 \tag{3.30}$$

The resulting velocity equations may be expanded and written in matrix form as:

$$\begin{bmatrix}\rho_1 & 0 & 0\\ 0 & \rho_2 & 0\\ 0 & 0 & \rho_3\end{bmatrix}\begin{bmatrix}\dot{\rho}_1\\ \dot{\rho}_2\\ \dot{\rho}_3\end{bmatrix} = \begin{bmatrix}(\mathbf{p}+\mathbf{a}_1)^{\mathrm{T}}\\ (\mathbf{p}+\mathbf{a}_2)^{\mathrm{T}}\\ (\mathbf{p}+\mathbf{a}_3)^{\mathrm{T}}\end{bmatrix}\begin{bmatrix}\dot{x}\\ \dot{y}\\ \dot{z}\end{bmatrix} \tag{3.31}$$

$$\mathbf{J}_{\boldsymbol{\rho}}\dot{\boldsymbol{\rho}} = \mathbf{J}_{\mathbf{x}}\dot{\mathbf{p}} \tag{3.32}$$

where $\mathbf{J}_{\boldsymbol{\rho}}$ and $\mathbf{J}_{\mathbf{x}}$ are the Jacobian matrices of the mechanism. The overall Jacobian of the mechanism is:

$$\mathbf{J} = \frac{\partial \mathbf{p}}{\partial \boldsymbol{\rho}} = \mathbf{J}_{\mathbf{x}}^{-1}\mathbf{J}_{\boldsymbol{\rho}} \tag{3.33}$$

but it is easier to derive the two separate Jacobians, as is often the case for parallel mechanisms. These matrices describe the linear relation between the actuator velocities $\dot{\boldsymbol{\rho}}$ and the end-effector velocities $\dot{\mathbf{p}}$. Furthermore, the time derivative of Equation 3.32 can be taken to determine the relationship between joint accelerations and the end-effector Cartesian acceleration.

$$\begin{bmatrix}\dot{\rho}_1 & 0 & 0\\ 0 & \dot{\rho}_2 & 0\\ 0 & 0 & \dot{\rho}_3\end{bmatrix}\begin{bmatrix}\dot{\rho}_1\\ \dot{\rho}_2\\ \dot{\rho}_3\end{bmatrix} + \begin{bmatrix}\rho_1 & 0 & 0\\ 0 & \rho_2 & 0\\ 0 & 0 & \rho_3\end{bmatrix}\begin{bmatrix}\ddot{\rho}_1\\ \ddot{\rho}_2\\ \ddot{\rho}_3\end{bmatrix} = \begin{bmatrix}\dot{\mathbf{p}}^{\mathrm{T}}\\ \dot{\mathbf{p}}^{\mathrm{T}}\\ \dot{\mathbf{p}}^{\mathrm{T}}\end{bmatrix}\begin{bmatrix}\dot{x}\\ \dot{y}\\ \dot{z}\end{bmatrix} + \begin{bmatrix}(\mathbf{p}+\mathbf{a}_1)^{\mathrm{T}}\\ (\mathbf{p}+\mathbf{a}_2)^{\mathrm{T}}\\ (\mathbf{p}+\mathbf{a}_3)^{\mathrm{T}}\end{bmatrix}\begin{bmatrix}\ddot{x}\\ \ddot{y}\\ \ddot{z}\end{bmatrix} \tag{3.34}$$

$$\dot{\mathbf{J}}_{\boldsymbol{\rho}}\dot{\boldsymbol{\rho}} + \mathbf{J}_{\boldsymbol{\rho}}\ddot{\boldsymbol{\rho}} = \dot{\mathbf{J}}_{\mathbf{x}}\dot{\mathbf{p}} + \mathbf{J}_{\mathbf{x}}\ddot{\mathbf{p}} \tag{3.35}$$

It is important to remember that these results neglect any angular velocities or accelerations of the end-effector that may be generated if the cables go slack or are not perfectly rigid.

The Jacobians also give insight into the mechanism behaviour. From linear algebra it is known that square matrices are not always invertible, and thus the system of linear equations they represent does not always possess a unique solution. A singular matrix is rank deficient and by definition will always have a determinant of zero. Poses that result in a singular Jacobian matrix can affect the mechanism's mobility and have a negative impact on its performance.

Singularities are typically categorized into three types [60]:

Type I Occur when $\det \mathbf{J}_{\boldsymbol{\rho}} = 0$. Therefore the null space of $\mathbf{J}_{\boldsymbol{\rho}}$ is not empty and there exist non-zero joint velocities that cause no Cartesian velocities of the end-effector. There will also exist some configurations that lead to reduced mechanism mobility where certain end-effector velocities are impossible to generate, regardless of the supplied actuator velocities.

Type II Occur when $\det \mathbf{J}_{\mathbf{x}} = 0$. In this case the null space of $\mathbf{J}_{\mathbf{x}}$ is not empty and there exist non-zero Cartesian velocities that do not require any corresponding joint velocities. As such, there exist configurations of increased mobility, where certain end-effector movements can occur, even when the actuators are locked.

Type III Occur when a parameter that defines the architecture of the mechanism allows both of the Jacobian matrices to simultaneously become singular. In this type of singularity the mechanism will demonstrate a combination of the behaviours typical to Type I and II.

Due to the duality of the Jacobians (see the virtual work explanation of the duality of the structural assembly matrix in Section 2.1.3) there are also poses in which no actuator forces, i.e., cable tensions, exist that allow the end-effector to resist or exert certain forces and moments. It becomes essential to identify these singular poses and prevent the mechanism from entering or passing through any of them for the mechanism to operate in a determinable manner.

The location of the tensegrity mechanism's singularities may be found by examining the determinants of the Jacobian matrices:

$$\det \mathbf{J}_{\boldsymbol{\rho}} = \rho_1 \rho_2 \rho_3 \tag{3.36}$$

$$\det \mathbf{J}_{\mathbf{x}} = -\frac{\sqrt{3}}{2} r_b z \tag{3.37}$$

From Equation 3.36 it can be seen that the determinant of $\mathbf{J}_{\boldsymbol{\rho}}$ will become zero when one, or more, of the actuator lengths equals zero. The upper limit placed

on the actuator lengths is usually considered to also be a form of singularity. However, due to the use of winch actuated cables, practically any length of cable can be achieved so this condition is ignored. From Equation 3.37 it can be seen that the determinant of $\mathbf{J_x}$ will become zero if the z–component of the position vector $\mathbf{p}$ is zero. Another singularity can occur if $r_\mathrm{b} = 0$, causing $\mathbf{J_x}$ to always be singular. This case is trivial because it would correspond to the end-effector and base triangles being points. In this situation all of the mechanism's components would be coincident, which is physically not possible and undesirable from a practical standpoint so the case may be ignored.

It should be noted that the only poses where $\rho_i = 0$ occur when $z = 0$. Therefore the XY-plane is the only singularity surface in the simplified kinematic model (i.e., the model shown in Figure 2.6a where cables are assumed taut). If allowed to reach the XY-plane, the spatial mechanism would degenerate into a planar mechanism and lose the ability to exert forces in the Z direction. It would also no longer be able to generate velocities in the Z direction. In practise, mechanical interferences would prevent a physical model of the mechanism from reaching this plane, eliminating the occurrence of the singularities.

While not included in the kinematic analysis, the torsion spring linkages could be considered to impose singularities on the mechanism. Each linkage is constrained to act in a plane, as shown in Section 2.3.3, and therefore resembles a two-link planar serial mechanism. Although the joints are all passive, this "serial mechanism" will still reach singularities if fully extended ($l_i = l_0$) or fully compressed ($l_i = 0$). When fully extended the torsion spring will no longer exert a force along its virtual length (i.e., along line A_iB_i). Moreover, fully extended spring linkages impose additional kinematic constraints on the mechanism, reducing the distance from the base that the end-effector can extend to. Physical limitations of the range of motion in the joints of the spring linkages would generally prevent these conditions from occurring.

3.3 Mechanical Interference Between Components

The possibility of mechanical interferences between the mechanism's components has already been mentioned. The torsion spring linkages applying prestress to the mechanism are designed specifically to avoid the constant interference that would be experienced by linear spring elements. However, the design is not without its own faults. Interference between the cables and the linkages are possible as they fold outwards and must share the same space. Some similar mechanisms [61] allow cable interferences to occur by compen-

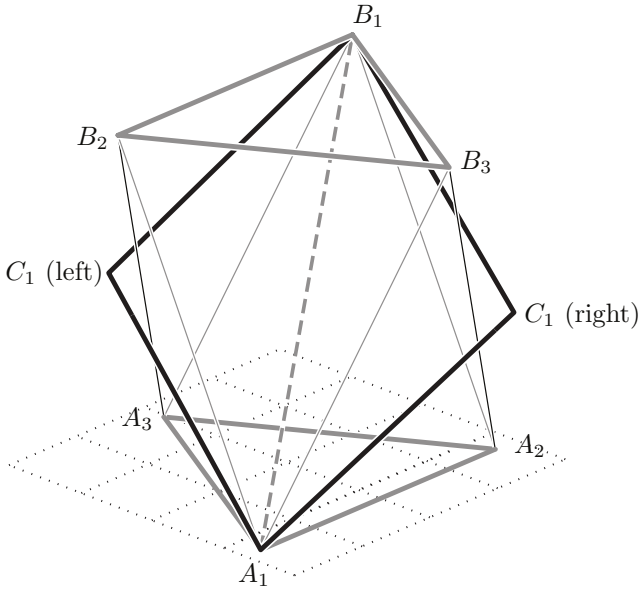

Figure 3.2: Assembly modes of the first torsion spring linkage and the cables (A_3B_2 if left-folding, A_2B_3 if right) that can potentially cause interference.

sating with redundant actuation but this adds complexity to their control. Instead mechanical interferences will be avoided and the constraints that this may place on the mechanism's movement will ideally be limited.

The location of the torsion spring joints must first be determined to gain a better idea of where the cables and linkages might interfere. The node C_i will be defined as the centre of each torsion spring. Therefore the proximal link of the spring linkages will be the line segment C_iA_i, and the distal link will be B_iC_i. Recalling the definitions of the universal joint axes $\mathbf{e}_{1i}$ and $\mathbf{e}_{2i}$ defined in Section 2.3.3 allows the vector that locates node C_i to be found as:

$$\mathbf{c}_i = \mathbf{a}_i - \frac{1}{2} l_i \mathbf{u}_i \pm \frac{1}{2} l_0 \cos\theta_i \left(\frac{\mathbf{u}_i \times \mathbf{e}_{2i}}{||\mathbf{u}_i \times \mathbf{e}_{2i}||} \right) \tag{3.38}$$

where the sign ambiguity of the last term reveals that the mechanism has multiple assembly modes. Each spring linkage can be assembled to fold in one of two directions, as shown in Figure 3.2. Due to axial symmetry in the mechanism, the two assembly modes where all linkages fold in the same direction are equivalent, albeit reversed. For simplicity all of the linkages will be considered to fold to the left, i.e., the last term in Equation 3.38 is considered to always be positive.

The assembly mode dictates which cables and links are at risk of potentially interfering. From visual inspection it can be seen that each spring linkages' distal and proximal links can only come into contact with a single cable. For example, Figure 3.2 highlights the cable that can potentially interfere with the links of the first ($i = 1$) linkage, depending on the assembly mode (i.e., right or left folding). The other cables are either on the side opposite from the direction that the linkage folds or share attachment nodes. Those cables sharing an attachment node will be routed through the joints located at these nodes (to be discussed in Chapter 6) and won't otherwise mechanically interfere with the linkages. Therefore, of the six cables present in the mechanism only three need be considered, and each can only interfere with a single linkage.

3.3.1 Interference Checking Method

Checking for mechanical interferences in parallel mechanisms has been widely addressed in literature. This is especially true for cable driven parallel mechanisms due to the large number of cables that must surround their end-effector and be present within the mechanism's workspace. Methods of quickly checking for interferences have been developed both for online determination and for generating sets of interference free configurations. The following approach is based on the one that Masory and Wang [62] developed for the Stewart-Gough platform, although it has since been adapted for use with CDPMs [63, 64].

The approach considers two skew line segments, arbitrarily defined here as $\overline{P_1Q_1}$ and $\overline{P_2Q_2}$ and shown in Figure 3.3. The direction of each segment is represented by a unit vector $\mathbf{n}_k$, $k = 1, 2$, and their starting points, P_k, are separated by the vector $\mathbf{d}$. It can be shown that the minimum distance between these two line segments must be along their shared normal, $\mathbf{n}_r$, defined as:

$$\mathbf{n}_r = \frac{(\mathbf{n}_1 \times \mathbf{n}_2)}{||(\mathbf{n}_1 \times \mathbf{n}_2)||} \tag{3.39}$$

The closest point on each line segment is considered to occur at R_k, which is located at a distance of c_k from point P_k. The minimum distance between the line segments, i.e., the distance between points R_1 and R_2, is represented as r. This allows the formation of the following vector loop equation:

$$c_1\mathbf{n}_1 + r\mathbf{n}_r - c_2\mathbf{n}_2 - \mathbf{d} = \mathbf{0} \tag{3.40}$$

or, alternatively, the vector equation may be rewritten as the following system

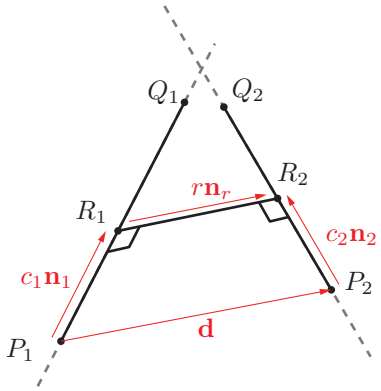

Figure 3.3: Vector notation used for calculating minimum distance between two arbitrary skew lines $\overline{P_1Q_1}$ and $\overline{P_2Q_2}$.

of equations:

$$\begin{bmatrix}\mathbf{n}_1 & \mathbf{n}_2 & \mathbf{n}_r\end{bmatrix}\begin{bmatrix}c_1\\-c_2\\r\end{bmatrix}=\begin{bmatrix}\mathbf{d}\end{bmatrix} \tag{3.41}$$

which is solvable, so long as $\mathbf{n}_1$ and $\mathbf{n}_2$ are not parallel. If the line segments were parallel there would be no unique minimum distance between the two lines.

Mechanical interference will occur if the sum of the radii of both the cable and the linkage in question exceeds the absolute value of the minimum distance between them. In most practical applications the diameter of the cables may be considered negligible. The geometry of the linkage will depend on the desired scale of the mechanism and the need to resist bending under the load of the torsion springs. For now they will be also be considered to have a negligible diameter. Additionally, the spring linkages are considered to always fold to the left, as shown in Figure 2.6b. As such, the only interferences that need be considered are those between the distal and proximal links of each spring linkage and the cable that passes between them, i.e., linkage 1 with cable $\overline{B_2A_3}$, linkage 2 with cable $\overline{B_3A_1}$, and linkage 3 with cable $\overline{B_1A_2}$.

It is important to note that although solving Equation 3.41 yields the minimum distance between the two lines, it may not necessarily yield the minimum distance between the line *segments*. More concisely, point R_k may not lie between points P_k and Q_k on one or both of the lines in question. To consider only the line segments, the condition $c_k \in [0, l_k]$, where l_k is the length of each segment, must be enforced when solving Equation 3.41. Several

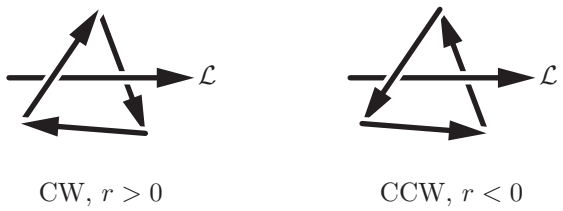

Figure 3.4: Definition of interference directions and their relation to the sign of r.

cases can occur (i.e., R_k can lie on both, one, or none of the respective line segments) and Equation 3.41 may need to be solved multiple times.

However, the mechanism's architecture and the chosen assembly mode allow a much simpler approach to be utilized. In the field of computer graphics, ray tracing is the exercise of determining whether or not digital "rays" of light intersect with an object in space. Object surfaces are often created using a tessellation of triangles, and if a ray intersects a triangle, that triangle is considered to be illuminated. The three sides of each triangle may be represented by vectors and the cross product method described earlier in this section may be used to calculate the value of r.

The difference, in this case, is that only the sign of r is of concern. If a ray passes through the triangle and the vectors describing the edges of the triangles are arranged tip-to-tail, as shown in Figure 3.4, then the sign of r, as calculated for each edge vector, will be the same. This can also be interpreted as the common normal vectors of the ray and the triangle edge all pointing toward or away from the ray vector. Furthermore, a common convention is used so that the vectors describing the sides of all triangles are connected in the same direction. As such, if all r values are positive for a given triangle and ray, the triangle's edge vectors pass around the ray in a clockwise direction, as shown in Figure 3.4.

This simplified approach may be applied to the tensegrity mechanism by considering the triangles made by nodes A_i, B_i, and C_i. Due to the geometry of the mechanism, for each cable and linkage that can potentially interfere, the cable must pass within this triangle. The vectors that represent the cable, distal, and proximal links are defined such that all $r > 0$ in an initial "home" position of $\mathbf{p} = [0, 0, r_b]^{\mathrm{T}}$. Subsequent poses can be checked for interferences by ensuring $r > 0$ still holds. The only limitation of this approach is that there could potentially be mechanism poses where this condition is met, but that are unreachable without passing through poses that cause interferences. This issue is addressed in the following section by using an iterative search

procedure.

3.3.2 Generating the Set of Interference Free Poses

The approach described in Section 3.3.1 is useful for checking individual poses of the mechanism but must be extended in order to define the set of all interference free poses. A possible method of generating this set would be to use an interval analysis technique. Interval analysis employs a special arithmetic to handle equations that contain variables with finite ranges of allowable values (i.e., intervals) instead of single values. Solutions provided by such arithmetic are also in the form of intervals and they encompass the entire range of all possible evaluations of an equation for all possible values in the input intervals. A full explanation of interval arithmetic is not within the scope of this thesis but is available in literature [65]. Such a method would generate a guaranteed set of poses that do not allow interferences.

In the case of interference checking, a three-dimensional interval or "box" representing the Cartesian space that will be investigated is generated. Using this box, the vectors defining each spring linkage segment and cable are derived (these too will be intervals) and then checked for interference. For every pose within the box to be interference free, every value in the resulting intervals must satisfy the interference conditions. A bisection algorithm, previously used in literature to generate workspace representations for cable driven parallel mechanisms [66–68], would then be used to refine the boxes checked for interference and yield a closer representation of the workspace volume.

However, the dependency problem discussed by Gouttefarde and Merlet [68] prevents effective use of interval analysis for this particular mechanism. The dependency problem is most easily explained by considering an interval as a variable with an amount of uncertainty, e.g., $x \pm \epsilon$. Generally, when more operations are performed on such a variable, especially operations such as exponents, the error in the result will become larger. This corresponds to an interval with expanded range because it must encompass all possible solutions. There are a large number of cross products and vector normalization operations that are performed to locate the nodes C_i and to check for interference between the cables and linkage segments. As such it becomes difficult to use the interval bisection method mentioned above because even small boxes will not fully satisfy the conditions of being interference free.

Although not ideal, the numeric approach detailed in Algorithm 3.1 is used to generate the boundaries of the mechanism's interference-free workspace. Cylindrical coordinates (z, θ, and d) are used to generate candidate poses that

are checked for interferences. For each pose, the inverse kinematics are solved to find vectors describing the linkage segments and cables. The minimum distances of separation between applicable links and cables are checked to verify that no interferences have occurred. Line search methods are then used to continue evaluating the candidate poses in the current direction until a pose is found that causes interferences.

Algorithm 3.1 yields a discrete set of points along the boundary surface of the mechanism's interference free workspace. This method is appropriate for gaining a rough estimation of the workspace, but is dependent on the resolution used to discretize the search space. However, regardless of the degree of resolution refinement, there is no guarantee that any points other than those actually checked are within the workspace. Unlike the interval analysis techniques discussed earlier, this method must be treated as a best-case estimate, since points outside of the workspace may be inadvertently included.

```
for z ∈ [0, z_max] do
    for θ ∈ [0, 2π) do
        d ← 0
        while d ≤ d_max do
            x ← d sin θ
            y ← d cos θ
            if IsPoseInterferenceFree(x, y, z) ≠ True then
                break
            else
                d ← d + d_increment
            end if
            StoreBoundaryPose(x, y, z)
        end while
    end for
end for
```

Algorithm 3.1: Numerical search algorithm for detecting the boundaries of the interference free workspace using cylindrical coordinates

3.4 Kinematic Workspace Boundaries

A mechanism's workspace refers to the set of poses it can achieve. This set is typically dependent on the mechanism geometry and the constraints that limit the motion of its joints and actuators. Only the kinematic constraints will be considered in this section. Other boundaries to the workspace that result from constraints such as maintaining cable tension will be discussed later in Chapter 4. The sources of the kinematic workspace boundaries may be summarized as follows:

Cables

The cables could theoretically limit the workspace since they must have a maximum achievable length, $\rho_{\max}$. However, the actuated winches can wind large quantities of cable onto reels. In practical applications, the winch systems can thus be designed to yield a maximum cable length that will not restrict the workspace because the later will be more limited by other components.

Spring linkages

The virtual length of the spring linkage will also have minimum and maximum ($l_{\min}$ and $l_{\max}$) values to which it can compress or extend. Ideally, the virtual spring length would achieve the range of $[0, l_0]$ but this is not realistic due to the mechanical limitations that will be present in its universal, revolute and spherical joints. Recalling that $\mathbf{b}_i = -\mathbf{a}_i$ if the mechanism end-effector maintains a constant orientation, Equation 3.7 can be rewritten as:

$$l_i^2 = (\mathbf{p} - 2\mathbf{a}_i)^{\mathrm{T}} (\mathbf{p} - 2\mathbf{a}_i) \tag{3.42}$$

which, similar to Equation 3.24, also describes a set of spherical boundaries. The workspace, based only on linkage constraints, would be the intersection of these three spheres, each having a radius of $l_{\max}$ and centred at $2\mathbf{a}_i$. An example of this volume for a mechanism with $l_{\max} = 4$ is shown in Figure 3.5, normalized to a base radius of $r_{\mathrm{b}} = 1$. In the likely event that $l_{\min} \neq 0$ there will be another three spheres also centred at $2\mathbf{a}_i$ with radii of $l_{\min}$. For example, the loss of workspace volume due to a lower limit of $l_{\min} = \frac{1}{2} r_{\mathrm{b}}$ is shown in Figure 3.5. The workspace volume will then be reduced by subtracting the union of the volumes contained within the three smaller spheres from the intersection of the larger three.

Singularities

As shown in Section 3.2 the entire XY plane is a singularity surface.

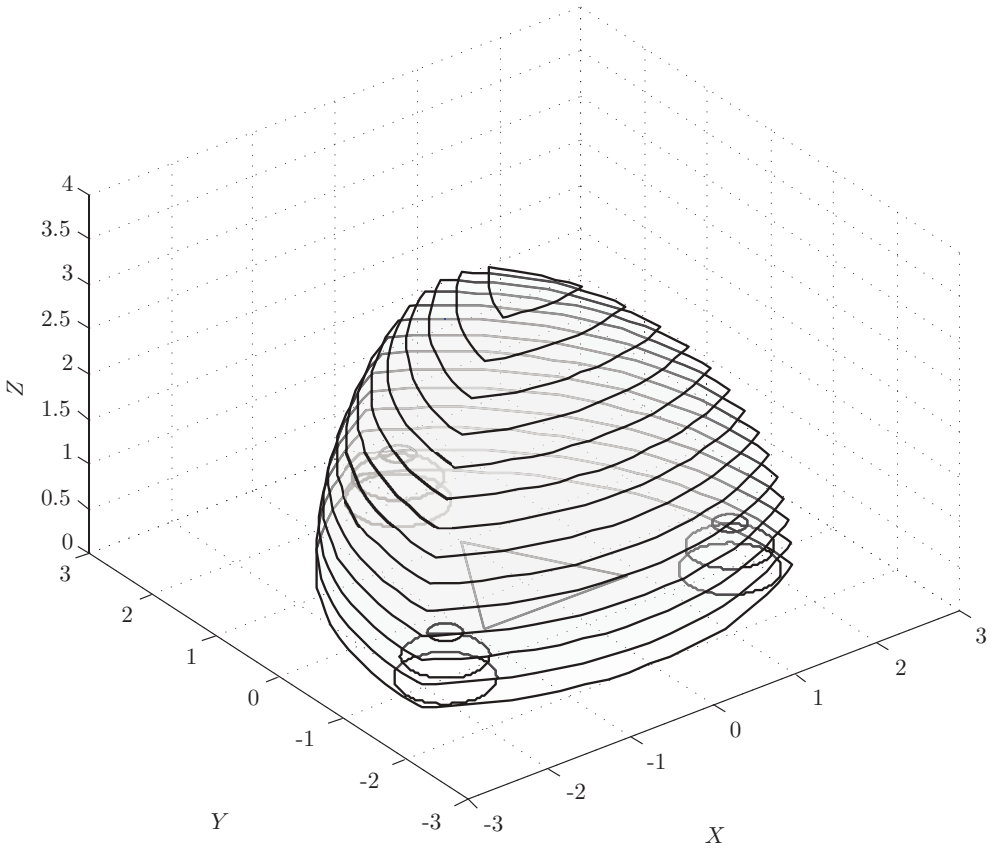

Figure 3.5: The maximum achievable workspace volume of the mechanism with $l_0 \in [\frac{1}{2}, 4]r_\mathrm{b}$. The results are normalized to the mechanism base radius $r_\mathrm{b} = 1$.

This constrains the continuous workspace volume of the mechanism to be either fully above or below the horizontal plane, since the mechanism should not pass through this boundary during operation. The volume above and below will be mirror opposites of each other so only one, chosen to be the positive half, needs to be considered.

Mechanical Interferences

Mechanical interferences have already been shown to occur between cables and the spring linkages and may further limit the kinematic workspace. Unlike the previous boundaries, there are no simple geometric descriptions available to describe where these interferences occur. Instead, these boundaries need to be determined numerically using the

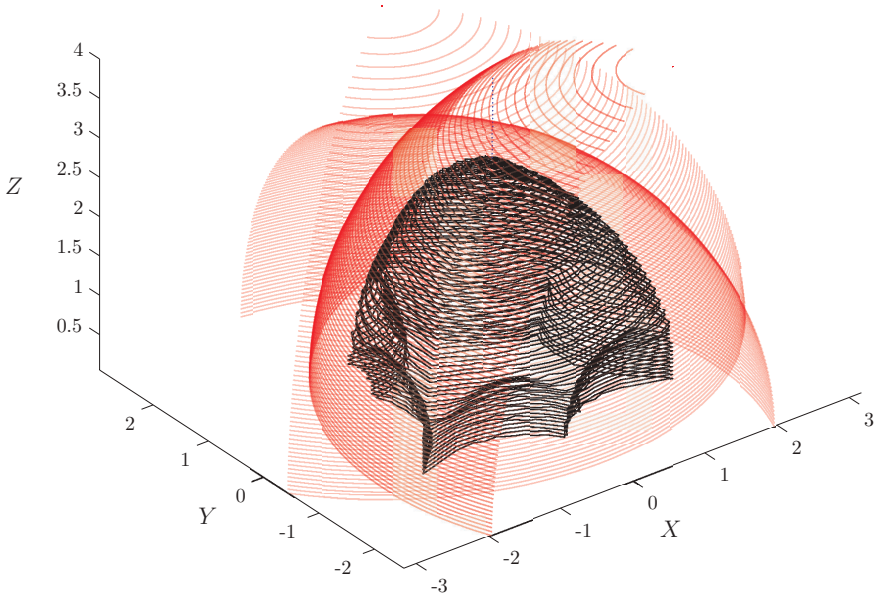

Figure 3.6: Three dimensional representation of the interference free workspace (shown in black) and the maximum reachable workspace (shown in red). The results are normalized to the mechanism radius, $r_\mathrm{b} = 1$, for the case where $l_0 = 4r_\mathrm{b}$.

approach described in Section 3.3. The entire interference free workspace is shown as a three dimensional volume in Figure 3.6 for a normalized example mechanism defined by $l_0 = 4r_\mathrm{b}$. Figure 3.7 also depicts the interference free workspace for the same example mechanism, this time using horizontal slices of the volume at various heights. For these parameters, mechanical interferences are shown to occur entirely inside the volume previously defined by the spring linkage constraints and therefore create a new boundary surface.

Interferences generally occur when the spring linkages approach full extension. Kinematically, the mechanism may be defined by only two parameters: its base radius and the spring rest length. Since increasing the base radius simply scales the entire mechanism, the interference surfaces will depend only on the ratio between the free length of the

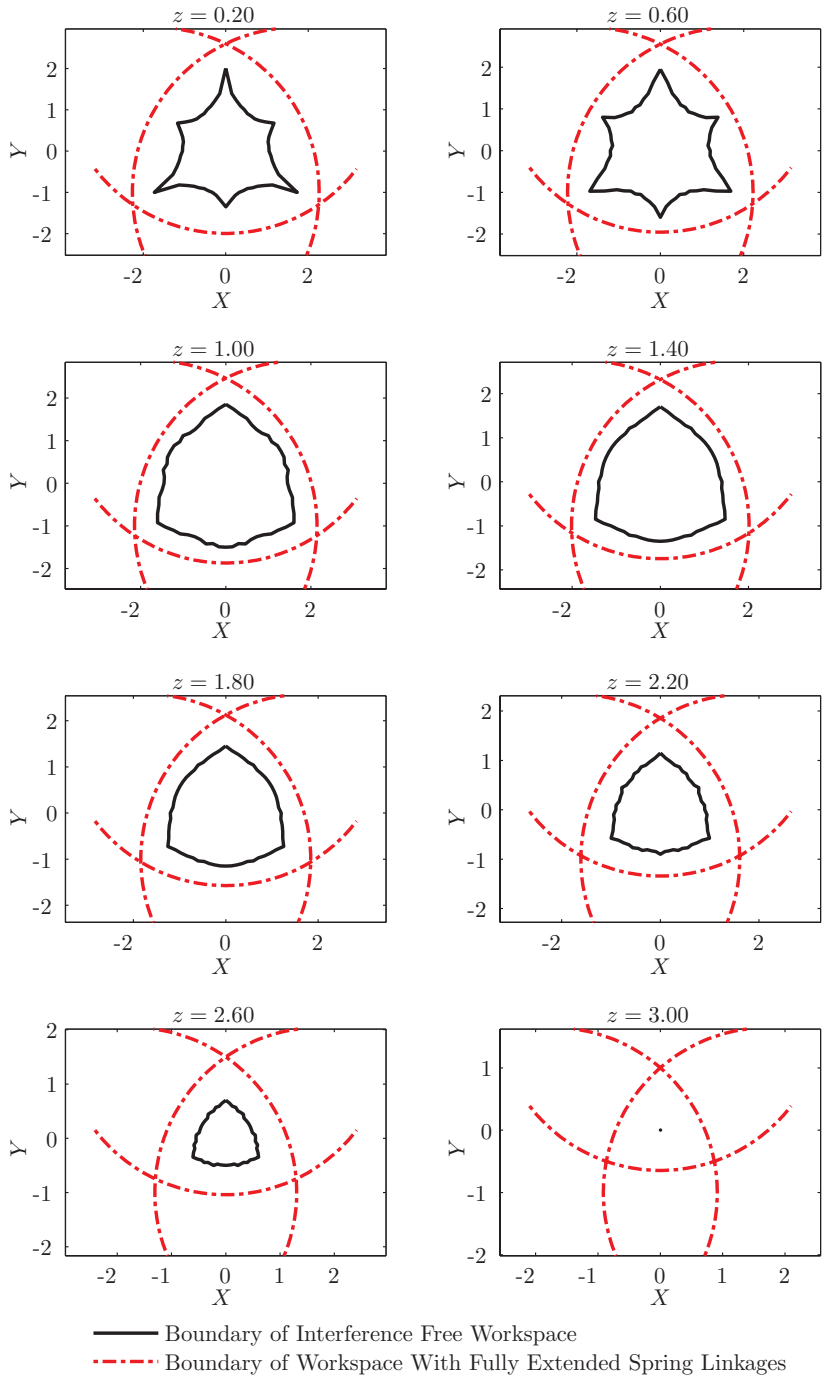

Figure 3.7: XY plane slices depicting the interference free workspace boundaries at increasing values of z. Normalized to the mechanism radius, r_b, and for the case where $l_0 = 4r_b$.

s

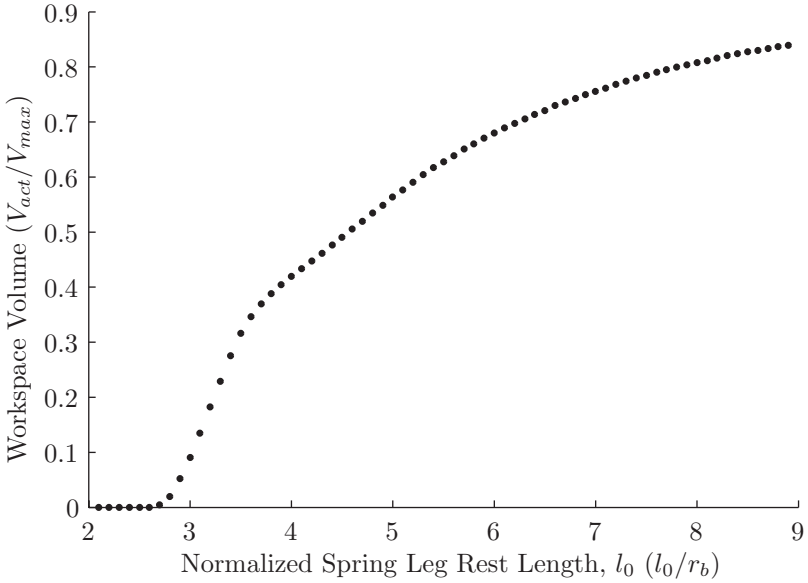

Figure 3.8: Volume fraction of the maximum reachable workspace that is interference free for various spring linkage rest lengths.

spring linkages and the base radius, i.e., l_0/r_b. Increasing this ratio should reduce the possibility of interferences because the linkages will remain folded outwards, away from the centre of the mechanism. To confirm this, the volume of the interference free workspace was estimated using a numerical approach for various normalized spring lengths. For comparison, the maximum workspace volume was calculated for each case using the analytical expression for the volume of a three sphere intersection derived by Gibson and Scheraga [69]. This assumes that each linkage has a full range of $l_i \in [0, l_{max}]$.

The fraction of the maximum workspace volume also contained within the interference free workspace is shown in Figure 3.8. As expected, the volume ratio gradually approaches unity. However, increasing the spring lengths will become detrimental to the goal of maximizing workspace volume. Eventually the mass of such linkages will become impractical and shorter linkages should be chosen that reach a compromise between mass and workspace volume.

4 Static Analysis

In Chapter 3, the tensegrity mechanism was demonstrated to experience only translational motion of its end-effector. This observation was made under the assumption that cable tension is maintained and all components are perfectly rigid. To verify that the cables remain taut, and that the mechanism will be able to support both its own weight and other external forces, an investigation into the internal forces of the mechanism must be undertaken. This chapter explores the mechanism's internal forces under static or pseudo static conditions where inertial effects are neglected. Wrench based analysis tools are introduced to calculate the cable tensions and a method of quantifying the set of external forces that can be generated by the mechanism is presented. The stiffness of the loaded end-effector is also investigated using techniques that are adapted from the analysis of parallel and cable-driven manipulators.

4.1 Wrench and Matrix Analysis Techniques

The primary goal of the static analysis is to calculate the tension in each actuated cable in an equilibrium pose. While the forces within the mechanism's joints and linkages may be of interest from a mechanical design perspective, this chapter is only concerned with the overall forces that the mechanism's components exert on the end-effector. Both the cables and spring linkages are attached to the end-effector using spherical joints and therefore do not directly transmit any moments. However, since the attachment points of the components ($\mathbf{b}_i$) are offset from the centre of mass, there will still be resultant moments generated. Once the direction and magnitude of the compressive forces exerted by the spring linkages are known, along with any external or gravitational loads, a force and moment balance about the mechanism's end-effector may be completed to calculate cable tensions.

The simplest representation of the spring linkages is to treat them as "virtual" compression springs, as mentioned in Section 2.3.3. This approach as-

sumes that each linkage exerts a compressive force f_i along the line passing through nodes A_i and B_i. The magnitude of the compressive force will always be negative (due to the force sign convention used in this thesis) and will have a non-linear relationship with the virtual length of each linkage.

Assuming that the torsion spring behaves linearly and is at rest when it is fully extended (i.e., $\theta_i = \theta_0 = \pi/2$) it will generate a torque equal to:

$$\tau_i = \kappa(2\theta_i - \pi) \tag{4.1}$$

where κ is the torsion spring constant and all three springs are considered to be identical. Taking a moment balance about the axis of the torsion spring's revolute joint, as shown in Figure 2.8, the magnitude of the force exerted by the spring is found to be:

$$f_i = \frac{2\tau_i}{l_0 \cos\theta_i} \tag{4.2}$$

Substituting Equation 4.1 and $\theta_i = \arcsin(l_i/l_0)$ into Equation 4.2 yields the following expanded equation:

$$f_i = \frac{2\kappa\left[2\arcsin\left(\frac{l_i}{l_0}\right) - \pi\right]}{l_0\sqrt{1 - \left(\frac{l_i}{l_0}\right)^2}} \tag{4.3}$$

In this equation it is recalled that the virtual length of each spring l_i is simply the distance between points A_i and B_i. Equation 4.3 leads to the spring force vector being defined as $\mathbf{f}_i = f_i\mathbf{u}_i$.

The virtual spring approach ignores the mass of the links in each spring linkage. In an ideal case, the torsion springs would be significantly stiff so that the forces that act on each linkage due to gravity could be considered negligible. However, mechanical and material constraints on the design of torsion springs, along with the counterproductive increase in mass that is inherent of larger springs, will limit the possible stiffness of the torsion spring. The mass of the links must therefore be considered and will alter the direction and magnitude of the spring force $\mathbf{f}_i$ based on the mechanism pose.

An analysis of each linkage in a given pose is possible due to the design of their universal joints. The full analysis is omitted here for brevity (see Appendix A) but the mass-dependent force that is exerted by each spring linkage is found to be:

$$\mathbf{f}_i = \begin{bmatrix} (\mathbf{u}_{\mathrm{d}i} \times \mathbf{e}_{2i})^{\mathrm{T}} \\ [(\mathbf{u}_{\mathrm{d}i} + \mathbf{u}_{\mathrm{p}i}) \times \mathbf{e}_{1i}]^{\mathrm{T}} \\ [(\mathbf{u}_{\mathrm{d}i} + \mathbf{u}_{\mathrm{p}i}) \times \mathbf{e}_{2i}]^{\mathrm{T}} \end{bmatrix}^{-1} \begin{bmatrix} \frac{2}{l_0}\tau_i - (\frac{1}{2}m_d\mathbf{g} \times \mathbf{u}_{\mathrm{d}i})^{\mathrm{T}}\mathbf{e}_{2i} \\ -(\mathbf{g} \times \mathbf{e}_{1i})^{\mathrm{T}}[(\frac{1}{2}m_p + m_s + m_d)\mathbf{u}_{\mathrm{p}i} + \frac{1}{2}m_d\mathbf{u}_{\mathrm{d}i}] \\ -(\mathbf{g} \times \mathbf{e}_{2i})^{\mathrm{T}}[(\frac{1}{2}m_p + m_s + m_d)\mathbf{u}_{\mathrm{p}i} + \frac{1}{2}m_d\mathbf{u}_{\mathrm{d}i}] \end{bmatrix} \tag{4.4}$$

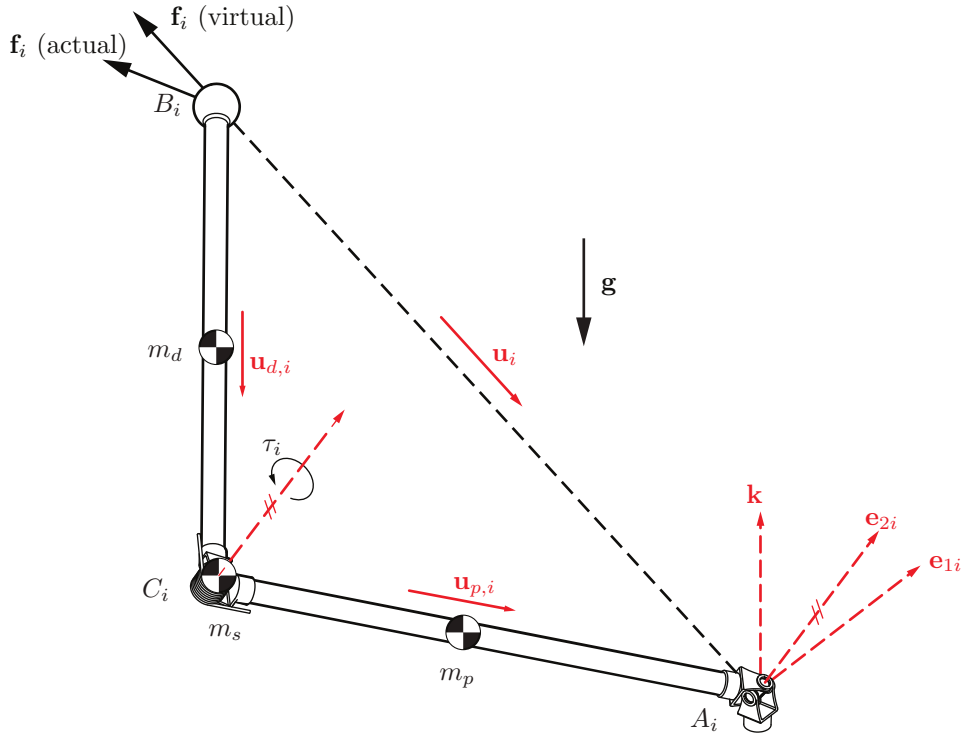

Figure 4.1: Internal and external forces that act on the ith torsion spring linkage.

where $\mathbf{g}$ is the gravity vector. The masses of the spring joint, and the proximal and distal links are m_s, m_p and m_d, respectively. The unit vectors $\mathbf{e}_{1i}$ and $\mathbf{e}_{2i}$ represent the axes of the universal joint at A_i and, as shown in Figure 4.1, $\mathbf{u}_{\mathrm{p}i}$ and $\mathbf{u}_{\mathrm{d}i}$ are unit vectors aligned with the proximal and distal links.

The consideration of gravity introduces the choice of orienting the mechanism such that its end-effector is above or below its mechanical base. In applications like pick-and-place, a robotic manipulator is typically chosen to be oriented above its workspace with its end-effector below, allowing it to freely manipulate objects on conveyor belts or workbenches. For the tensegrity mechanism specifically, this orientation will have the added benefit that the mechanism's weight will tend to pull on cables, thus potentially increasing prestress. Equation 4.4 clearly shows that the spring force is gravity dependent, and the weight of the linkages may add to the force that acts on the end-effector. This force is also pose dependent, so it is likely that the shape of the static workspace will be determined by the mass of the linkages. The

effect of gravity and component mass on the volume of the static workspace will be discussed later in this chapter.

The forces applied to the end-effector by the cables are easier to represent. The mass of the cables will be negligible at the scale that the mechanism is likely to be built and cable sagging may be ignored. Therefore the tensile force t_j within each cable will be applied in the direction of the unit vector $\mathbf{v}_j$ (as defined in Figure 3.1) that represents its longitudinal axis. The force balance on the end-effector centre of mass is:

$$\sum_{j=1}^{6} t_j \mathbf{v}_j + \sum_{i=1}^{3} \mathbf{f}_i + m_e \mathbf{g} + \mathbf{f}_{\text{ext}} = \mathbf{0} \tag{4.5}$$

where m_e is the mass of the end-effector and $\mathbf{f}_{\text{ext}}$ is the sum of all externally applied forces that act on the end-effector's centre of mass. The total moment applied about the centre of mass is:

$$\sum_{j=1}^{6} (\mathbf{b}_* \times t_j \mathbf{v}_j) + \sum_{i=1}^{3} (\mathbf{b}_i \times \mathbf{f}_i) + \mathbf{n}_{\text{ext}} = \mathbf{0} \tag{4.6}$$

where $\mathbf{b}_*$ is the vector representing the appropriate attachment point of the jth cable (refer to Table 2.2 for the connections), $\mathbf{b}_i$ is the attachment point of the ith spring, and $\mathbf{n}_{\text{ext}}$ is any externally applied moment.

For convenience, a wrench-based notation will be adopted. A wrench, $\mathbf{w} \in \mathbb{R}^6$, is a vector that combines both a force and a moment, i.e., $\mathbf{w} = [\mathbf{f}^{\mathrm{T}}, \mathbf{n}^{\mathrm{T}}]^{\mathrm{T}}$, and simplifies the representation of the balance equations. Additionally, there exists a linear relationship between the individual cable tensions and the overall wrench they apply to the end-effector. As such, the sum of their contributions may be re-written using the 6×6 wrench matrix $\mathbf{W}$ defined as:

$$\mathbf{W} = \begin{bmatrix} \mathbf{v}_1 & \mathbf{v}_2 & \mathbf{v}_3 & \mathbf{v}_4 & \mathbf{v}_5 & \mathbf{v}_6 \\ \mathbf{b}_3 \times \mathbf{v}_1 & \mathbf{b}_3 \times \mathbf{v}_2 & \mathbf{b}_2 \times \mathbf{v}_3 & \mathbf{b}_2 \times \mathbf{v}_4 & \mathbf{b}_1 \times \mathbf{v}_5 & \mathbf{b}_1 \times \mathbf{v}_6 \end{bmatrix} \tag{4.7}$$

where in translation $\mathbf{b}_i = -\mathbf{a}_i$. When combined with the total wrench exerted by all three springs, $\mathbf{w}_s$, the following wrench balance equation can be written:

$$\mathbf{W}\mathbf{t} + \mathbf{w}_s + \mathbf{w}_{\text{ext}} = \mathbf{0} \tag{4.8}$$

where $\mathbf{w}_{\text{ext}}$ represents all externally applied wrenches.

This concise notation allows for the cable tensions to be computed so long as the wrench matrix $\mathbf{W}$ is invertible, i.e., as long as the determinant of $\mathbf{W}$

is non-zero. For an equilibrium pose of the mechanism, the wrench matrix can be expressed in terms of the end-effector Cartesian coordinates and the compatible cable lengths. The determinant of the wrench matrix can then be simplified as:

$$\det(\mathbf{W}) = \frac{81\sqrt{3}}{4}\left(\frac{z^3 r_b^6}{\rho_1^2\rho_2^2\rho_3^2}\right) \tag{4.9}$$

which shows that the matrix becomes singular when $z = 0$ or becomes undefined if $\rho_i = 0$. Both of these conditions can only occur if the end-effector becomes coincident with the xy-plane. This singularity result is analogous to those discussed in Section 3.2. The wrench matrix and the mechanism's Jacobian share some of the same singularities, which is consistent with the theory of virtual work. As previously mentioned, in practice the xy-plane would be unreachable due to the mechanical constraints of the mechanism. Therefore the cable tensions can be calculated in any practically reachable pose.

The boundaries to the static workspace are then defined by the following set of inequalities:

$$\mathbf{t} = -\mathbf{W}^{-1}\left(\mathbf{w}_s + \mathbf{w}_{\text{ext}}\right) > \mathbf{0} \tag{4.10}$$

which ensures that tension within all cables remains positive. Verifying that Equation 4.10 is satisfied is an effective method of checking the state of the mechanism in a single pose but requires exact knowledge of externally applied forces and moments.

4.2 Force Capabilities

A method of quantifying the load capabilities of the mechanism, rather than just checking individual poses, would be useful in the evaluation and optimization of the mechanism design. Additionally, in practice there will exist an upper limit to the cable tensions that can be generated by the mechanism's winch actuators. Generating the set of allowable external wrenches that can be resisted while tension is constrained to a feasible range of positive values is the goal of this section.

The problem of defining the set of poses in which the robot can support a set of applied wrenches has been addressed frequently in the study of cable driven parallel mechanisms. One approach, the wrench closure workspace (WCW) [70], is defined as the set of poses that can support any externally applied wrench while maintaining positive tension, i.e., $t \in [0, \infty]$. Realistically, there will limits to the range of tensions, as well as the applied wrenches. Alternatively the wrench feasible workspace (WFW) [68, 71] defines a set of poses that support a given required set of wrenches based on a finite range

of cable tensions. However, both of these methods are better suited for fully-constrained CDPMs with antagonistic cable actuation supplying prestress, rather than gravity or springs.

The tensegrity mechanism is similar to suspended cable mechanisms; it uses prestress to keep cables taut instead of antagonistic cable actuation. Without antagonistic cables the mechanism's WCW is an empty set. Additionally, the set of required wrenches is unknown at this time in the mechanism's development but are required for calculating the WFW. Instead, it is more informative to try to characterize the wrenches that the mechanism can generate over its workspace. Fortunately, a method of geometrically developing the Available Wrench Set (AWS) introduced by Bouchard et al. [66] does just that.

4.2.1 Available Wrench Set

The available wrench set is the set of all external wrenches that can be generated by the end-effector of a mechanism. To begin, $\mathbf{w}_{\text{ext}} = \mathbf{w}_g - \mathbf{w}_e$ is substituted into Equation 4.8 so that it can be rewritten as:

$$\mathbf{w}_e = \mathbf{W}\mathbf{t} + \mathbf{w}_s + \mathbf{w}_g \tag{4.11}$$

where $\mathbf{w}_e$ is now treated as the total wrench that can be *exerted* by the end-effector, rather than resisted by it. The $\mathbf{w}_g$ term is included to represent the weight of the end-effector.

Vectors of minimum tension, $\underline{\mathbf{t}}$, and maximum tension, $\overline{\mathbf{t}}$, are defined as:

$$\underline{\mathbf{t}} = [\underline{t}_1, \underline{t}_2, \underline{t}_3, \underline{t}_4, \underline{t}_5, \underline{t}_6]^{\mathrm{T}}, \qquad \overline{\mathbf{t}} = \left[\overline{t}_1, \overline{t}_2, \overline{t}_3, \overline{t}_4, \overline{t}_5, \overline{t}_6\right]^{\mathrm{T}} \tag{4.12}$$

based on a specified range of allowable cable tensions. As such, any valid cable tension vector must be in that range, i.e., $\mathbf{t} \in [\underline{\mathbf{t}}, \overline{\mathbf{t}}]$. This vector inequality is interpreted as meaning each individual element of vector $\mathbf{t}$ satisfies $\underline{t}_j \leq t_j \leq \overline{t}_j$. Using this tension constraint and Equation 4.11, the available wrench set $\mathcal{A}$ is defined as:

$$\mathcal{A} = \left\{ \mathbf{w}_e \in \mathbb{R}^6 \;\middle|\; \mathbf{w}_e = \mathbf{W}\mathbf{t} + \mathbf{w}_s + \mathbf{w}_g,\, \mathbf{t} \in [\,\underline{\mathbf{t}}, \overline{\mathbf{t}}\,] \right\} \tag{4.13}$$

which is set notation for "all six dimensional wrenches $\mathbf{w}_e$ that satisfy Equation 4.11 and have tensions between the minimum and maximum values".

Borrowing from the approach used by Bouchard et al. [66], a new parameter, α, is introduced:

$$\alpha_j = \frac{t_j - \underline{t}_j}{\Delta t_j} \tag{4.14}$$

where $\Delta t_j = \bar{t}_j - \underline{t}_j$. Cable tension t_j is constrained to be between $\underline{t}_j$ and $\bar{t}_j$ so it may be observed that the parameter α_j must remain between 0 and 1. This allows the set from Equation 4.13 to be rewritten as:

$$\mathcal{A} = \left\{ \mathbf{w}_e \in \mathbb{R}^6 \;\middle|\; \mathbf{w}_e = \sum(\mathbf{w}_j \alpha_j \Delta t_j) + \mathbf{W}\underline{\mathbf{t}} + \mathbf{w}_s + \mathbf{w}_g,\ \alpha_j \in [0,1] \right\} \quad (4.15)$$

where $\mathbf{w}_j$ is the jth column of matrix $\mathbf{W}$. Bouchard et al. made the observation that in this form $\mathcal{A}$ shares the definition of a zonotope.

A zonotope is a set of points in space formed by the combinatorial addition of a set of vectors in that space, known as a Minkowski sum. To better understand this concept, consider the following set of two dimensional vectors:

$$\mathcal{Z} = \left\{ \alpha_1 \begin{bmatrix} 0 \\ 1 \end{bmatrix} + \alpha_2 \begin{bmatrix} 0.5 \\ 0.5 \end{bmatrix} + \alpha_3 \begin{bmatrix} 0.5 \\ 0 \end{bmatrix}, \alpha_k \in [0,1] \right\}, k = 1,2,3$$

which has some similarities to the set in Equation 4.15. The Minkowski sum of the generator vectors can be seen graphically in Figure 4.2a. Every point contained within set $\mathcal{Z}$ may be written as a sum of the generator vectors, each multiplied by a different coefficient α_k. Points that are full combinations of the generator vectors are labelled with their indices. For example, the point (1,1,1) indicates that the coefficients are $\alpha_1, \alpha_2, \alpha_3 = 1,1,1$ and the point is the full sum of all three vectors. A convex hull of all of these points, shown by the bold lines in Figure 4.2a, forms a polygon that fully encloses the set. This is the definition of a two dimensional zonotope. In general, a zonotope can be formed from generator vectors in any dimension, so the concept can be extended, forming a convex polyhedron in $\mathbb{R}^3$ and a convex polytope in $\mathbb{R}^n$ for $n > 3$.

In the case of the available wrench set, the generator vectors are the columns of the wrench matrix, scaled by the respective Δt_j. This makes every point within the formed zonotope a valid wrench that can be exerted by the mechanism. The other terms in Equation 4.15, i.e., $\mathbf{W}\underline{\mathbf{t}}$, $\mathbf{w}_s$, and $\mathbf{w}_g$, translate the zonotope but do not affect its shape. In the case of the tensegrity mechanism, where the wrenches being considered are in $\mathcal{R}^6$, the zonotope becomes difficult to visualize but is still generated in the same manner.

As a simpler, more easily visualized example, consider the mechanism in Figure 4.3a. It consists of a point mass "end-effector", actuated by two cables and a linear spring to supply prestress. For a given pose, the generator vectors are unit vectors aligned with the cables, scaled by the range of allowable tensions. The zonotope is found in the same way as in Figure 4.2a, with the exception that the spring force and the minimum cable tensions cause the whole zonotope to translate, seen in Figure 4.3b. In this simplified case, the

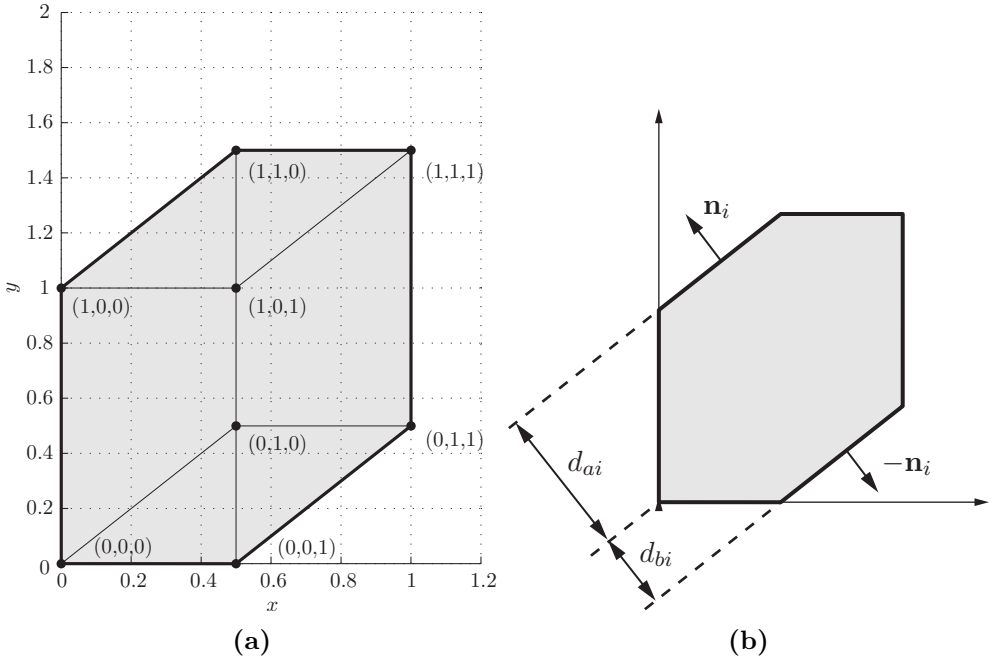

Figure 4.2: Example of a two dimensional zonotope formed by Minkowski sum.

shaded area in the figure represents all of the forces the mechanism can exert. For instance, it can be seen that the mechanism can apply a relatively large upwards force. This makes sense because this is the general direction the cables are pulling. However, a downwards force of similar magnitude would likely be outside of the shaded region. Again, this makes sense since the spring only applies a finite prestress and cable tension can only be lowered to a certain point before going slack.

Using a convex hull to define the zonotope is a straightforward approach but has some disadvantages. Methods of deriving a convex hull, such as the well-known Quick Hull algorithm [72], are iterative and can take an unpredictable amount of time to run, especially for higher dimensions. In response, Bouchard et al. [66] formulated an alternative method of representation termed the hyperplane shifting method.

4.2.2 Hyperplane Shifting Method

A hyperplane is the higher dimensional equivalent of a plane and divides a space in half, with all points lying above or below it. If all points in a set are

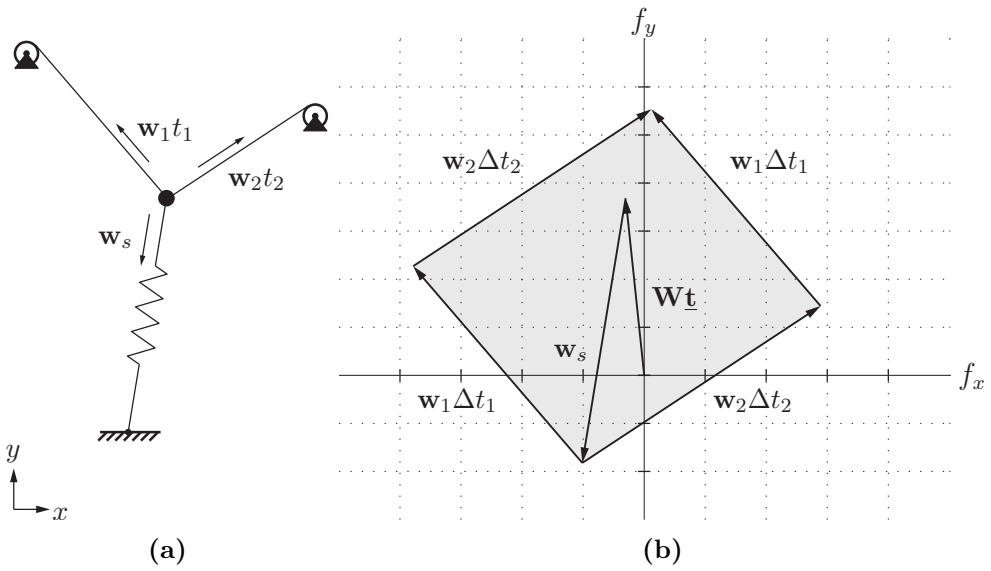

Figure 4.3: Example of a 2D cable mechanism (a) and its available wrench set (b).

located on one side of a hyperplane, that hyperplane is said to support the set [66]. Furthermore, a convex polytope may be represented using a number of supporting hyperplanes that fully enclose all points in the set [73]. The ith supporting hyperplane is defined using a normal vector $\mathbf{n}_i$ and a scalar value d_i. The normal vector is directed "above" the hyperplane, i.e., its direction is toward the outside of the zonotope that it supports. The scalar d_i represents how far the hyperplane is shifted, i.e., translated, from the origin and is calculated by projecting a point, known to lie anywhere on the hyperplane, onto that hyperplane's normal vector.

For a point, or in this case the available wrench $\mathbf{w}_e$, to be supported by a hyperplane the following inequality must be satisfied:

$$\mathbf{n}_i^{\mathrm{T}} \mathbf{w}_e \leq d_i \tag{4.16}$$

where the contributions from the springs $\mathbf{w}_s$, the end-effector weight $\mathbf{w}_g$ and the minimum tension $\mathbf{W}\underline{\mathbf{t}}$ terms in Equation 4.15 cause a shift of the zonotope and are accounted for in the values of d_i. Gouttefarde and Krut [74] provided a mathematical proof of this approach as well an improved method of calculating the normal vectors requiring fewer computations. Regardless of the method used to calculate the normal vectors, the available wrench set may be written

as a set of linear inequalities:

$$\mathbf{N}\mathbf{w}_e \leq \mathbf{d} \tag{4.17}$$

where $\mathbf{N}$ is a matrix such that its ith row is equal to $\mathbf{n}_i^{\mathrm{T}}$ and $\mathbf{d}$ is a vector whose ith element is d_i. The inequalities describe linear bounds on a space in a manner similar to constrained optimization in linear programming. By projecting any external wrench onto the hyperplane norms, it can be determined if all constraints (cable tensions) are satisfied and whether the wrench can be generated by the mechanism.

The hyperplane shifting method provides an efficient way of checking if the mechanism can support an external wrench while maintaining cable tensions. Quantifying the size of the available wrench set in a meaningful way is not as easy, since it is highly likely that the set is not symmetric about the origin or about its own centre. Calculating the volume of the available wrench set also introduces obscure units and yields little practical information. Alternatively, there are ways of utilizing the properties of zonotopes to quantify the load capabilities of the mechanism over its workspace, as well as deriving the static boundaries of this workspace.

4.2.3 Characterizing the Available Wrench Set

Several authors [4,75] have quantified the size of a zonotope by calculating the maximum radius of a hypersphere (i.e., a sphere in an arbitrary dimension) centred at the origin that is contained within the zonotope. Physically this radius will represent the maximum magnitude of a wrench that can be applied to the end-effector in an arbitrary direction. The largest hypersphere will be tangent to the hyperplane nearest the origin because zonotopes are convex. The surface of the hypersphere where it becomes tangent to the hyperplane is orthogonal to the hyperplane normal and the radius of the hypersphere is therefore equal to the corresponding d_i. The nearest plane will have the smallest corresponding d_i and therefore the maximum arbitrary wrench magnitude will simply be:

$$||\mathbf{w}_e|| \leq \min_i d_i \tag{4.18}$$

While useful, this characterization suffers from inconsistent units. In the case of the tensegrity mechanism, the wrench vector will include both force and moment units, which causes the magnitude of the wrench to be physically meaningless. A matrix partitioning technique is introduced here to separate the force components of the wrench vector from the moments and derive a

meaningful index for evaluating the load capabilities of the mechanism. The $\mathbf{N}$ matrix is partitioned into four submatrices:

$$\mathbf{N} = \left[\begin{array}{c:c} \mathbf{N}_{aa} & \mathbf{N}_{ab} \\ \hdashline \mathbf{N}_{ba} & \mathbf{N}_{bb} \end{array}\right] \tag{4.19}$$

and the vector $\mathbf{d}$ is split into two parts:

$$\mathbf{d} = \begin{bmatrix} \mathbf{d}_a \\ \hdashline \mathbf{d}_b \end{bmatrix} \tag{4.20}$$

The maximum arbitrary wrench is partitioned into its force $\mathbf{f}_e$ and moment $\mathbf{n}_e$ components:

$$\mathbf{w}_e = \begin{bmatrix} \mathbf{f}_e \\ \mathbf{n}_e \end{bmatrix} \tag{4.21}$$

so that the inequality in Equation 4.17 can be rewritten as:

$$\mathbf{N}_{aa}\mathbf{f}_e + \mathbf{N}_{ab}\mathbf{n}_e \leq \mathbf{d}_a \tag{4.22}$$

$$\mathbf{N}_{ba}\mathbf{f}_e + \mathbf{N}_{bb}\mathbf{n}_e \leq \mathbf{d}_b \tag{4.23}$$

There will be an even number of supporting hyperplanes and each will have a parallel pair due to the nature of zonotopes [73]. These parallel pairs will share a normal vector, although with opposite signs, and represent opposite faces of the zonotope. The normal vectors can be sorted when constructing the matrix $\mathbf{N}$ such that $\mathbf{N}_{aa} = -\mathbf{N}_{ba}$ and $\mathbf{N}_{ab} = -\mathbf{N}_{bb}$. It is important to note that the distance each hyperplane pair is shifted will not necessarily be equal, i.e., $\mathbf{d}_a \neq \mathbf{d}_b$.

An assumption must now be made about the nature of the loads being applied to the mechanism. The primary application proposed for the tensegrity mechanism is pick-and-place operations. Assuming that the objects being manipulated by the mechanism are located in close proximity to the centre of mass of the end-effector, they will not generate substantial moments. When combined with the knowledge that the mechanism will be operating in translational motion only, the net external wrench applied will be considered negligible, i.e., $\mathbf{n}_e \approx \mathbf{0}$. Equation 4.22 and Equation 4.23 can then be combined as follows:

$$\begin{bmatrix} \mathbf{N}_{aa} \\ -\mathbf{N}_{aa} \end{bmatrix} \mathbf{f}_e \leq \begin{bmatrix} \mathbf{d}_a \\ \mathbf{d}_b \end{bmatrix} \tag{4.24}$$

The rows of $\mathbf{N}_{aa}$ must be re-normalized so that they are of unit length. The values of $\mathbf{d}_a$ and $\mathbf{d}_b$ must also be divided by the magnitude of the rows of

Table 4.1: Physical parameters of the constructed prototype mechanism.

Parameter			
Name	Symbol	Value	Unit
Base triangle radius	r_b	0.2034	m
Spring leg rest length	l_0	0.8636	m
Torsion spring stiffness	κ	4.74	$\mathrm{N \cdot m \cdot rad^{-1}}$
Cable stiffness	k_cable	24.742	$\mathrm{kN \cdot m^{-1}}$
Torsion spring joint mass	m_s	0.186	kg
Lower leg segment mass	m_p	0.399	kg
Upper leg segment mass	m_d	0.168	kg
End-effector mass	m_e	0.823	kg

$\mathbf{N}_{aa}$ to still satisfy the linear inequality. The force-only zonotope is therefore described as:

$$\mathbf{N}'\mathbf{f}_e \leq \mathbf{d}' \tag{4.25}$$

where $\mathbf{N}'$ and $\mathbf{d}'$ are the adjusted versions of the matrix and vectors found in Equation 4.24. All elements in the reduced zonotope have force units. The maximum magnitude of an arbitrary force that can be supported by the mechanism while satisfying tension requirements corresponds to the value of smallest positive element in $\mathbf{d}'$.

Reducing the dimension of the zonotope to $\mathcal{R}^3$ has the additional benefit that the available wrench set can now be visualized. Figure 4.4 shows the three primary views and an isometric view of the available wrench set at pose $\mathbf{p} = [0, 0, r_b]^\mathrm{T}$. This force-only zonotope was generated by limiting cable tension to $\mathbf{t} \in [1, 20]$ N and using the mechanism parameters listed in Table 4.1. These parameters are found from the constructed prototype that is described in Chapter 6. For this case gravity was ignored.

Figure 4.4 also shows the sphere that represents the maximum force that can be applied in any arbitrary direction which, as earlier described, lies tangent to the side of the zonotope closest to the origin. In this particular pose the sphere's radius is approximately 15.2 N. It can be clearly seen that while this is the maximum force that can be exerted in any arbitrary direction, the mechanism is still capable of exerting much larger forces in certain directions, e.g., vertically along the z axis. The major axis of the available wrench set, defined as the direction of the maximum available wrench, depends highly on the pose of the mechanism. For example, when centred above the origin, the mechanism's symmetry leads to a symmetric polygon with the major axis be-

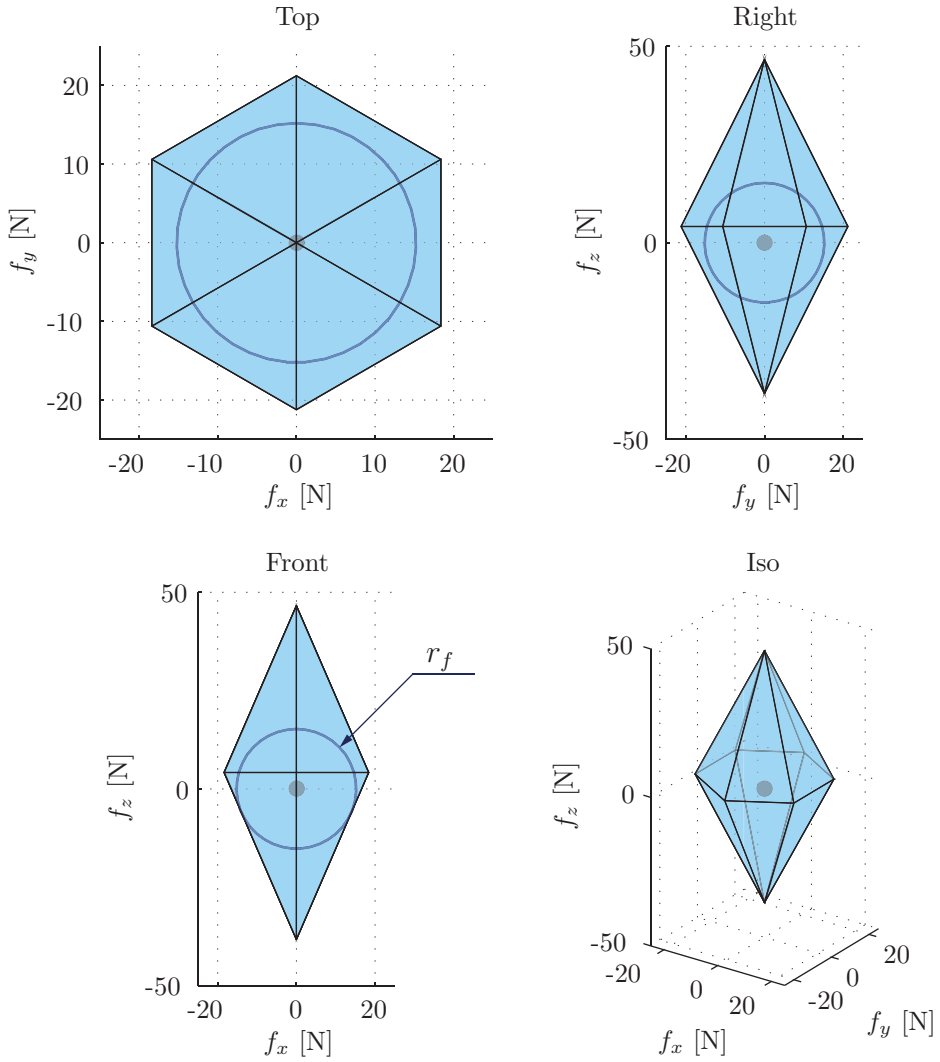

Figure 4.4: Multiple viewing angles of the force-only zonotope representing the available wrench set at $\mathbf{p} = [0, 0, r_b]^{\mathrm{T}}$ while neglecting gravity.

ing vertical but in other poses, as shown in Figure 4.5, the AWS starts tilting in other directions. The shape of the AWS remains similar but the major axis tends to be roughly parallel to a line drawn between the centre of the mechanism's base and end-effector. This makes sense since this is the general direction in which the cables and springs act. While knowledge of the major axis may be useful when designing for specific applications, the maximum arbitrary wrench magnitude, r_f, is of more interest in this general examination of the mechanism.

4.2.4 Static Workspace Visualization

To investigate the force capabilities of the mechanism over its workspace, a grid of kinematically feasible poses was generated. For each pose the available wrench set was developed, based again on the prototype parameters and this time limiting tension to $t \in [1, 20]$ N. Then the AWS was reduced to three dimensions so that the maximum arbitrary force, r_f, could be calculated. This procedure was repeated for three cases. The first case considered the mechanism to be "standing", i.e., the end-effector is always located above the base, causing its weight to tend to reduce prestress and lower tension. The next case considered the mechanism to be "hanging", i.e., the end-effector is always located below the base and its weight tends to increase prestress and tension. In the third case gravity was ignored, assuming that the spring stiffness of the legs provide enough prestress that their weights are negligible. The results from all three cases are shown in Figures 4.6-4.8.

The figures to the left display the contours of r_f at several heights over the workspace of the mechanism. This reveals the relative strength of the mechanism in any given pose. In general, it can be observed that closer to the centre of the static workspace the mechanism exhibits larger force capabilities than toward the outer boundaries. This makes sense because in these central poses the spring legs will be more compressed and increase the prestress of the mechanism. The spring legs will also be positioned in a more symmetric manner and therefore apply forces of similar magnitudes. For the mechanism to move away from centre, at least one of the spring legs must start compressing or extending more than the others. As such, the spring forces will tend to decrease the further a pose is from the Z-axis. The magnitude of the spring forces will also become increasingly dissimilar. While this allows the mechanism to exert larger forces in certain directions, the overall set of wrenches or forces available to it in any arbitrary direction will decrease.

The figures also include a visualization of the volume defined by $r_f = 0$. Each volume defines one possibility of a static workspace with, in this case, the

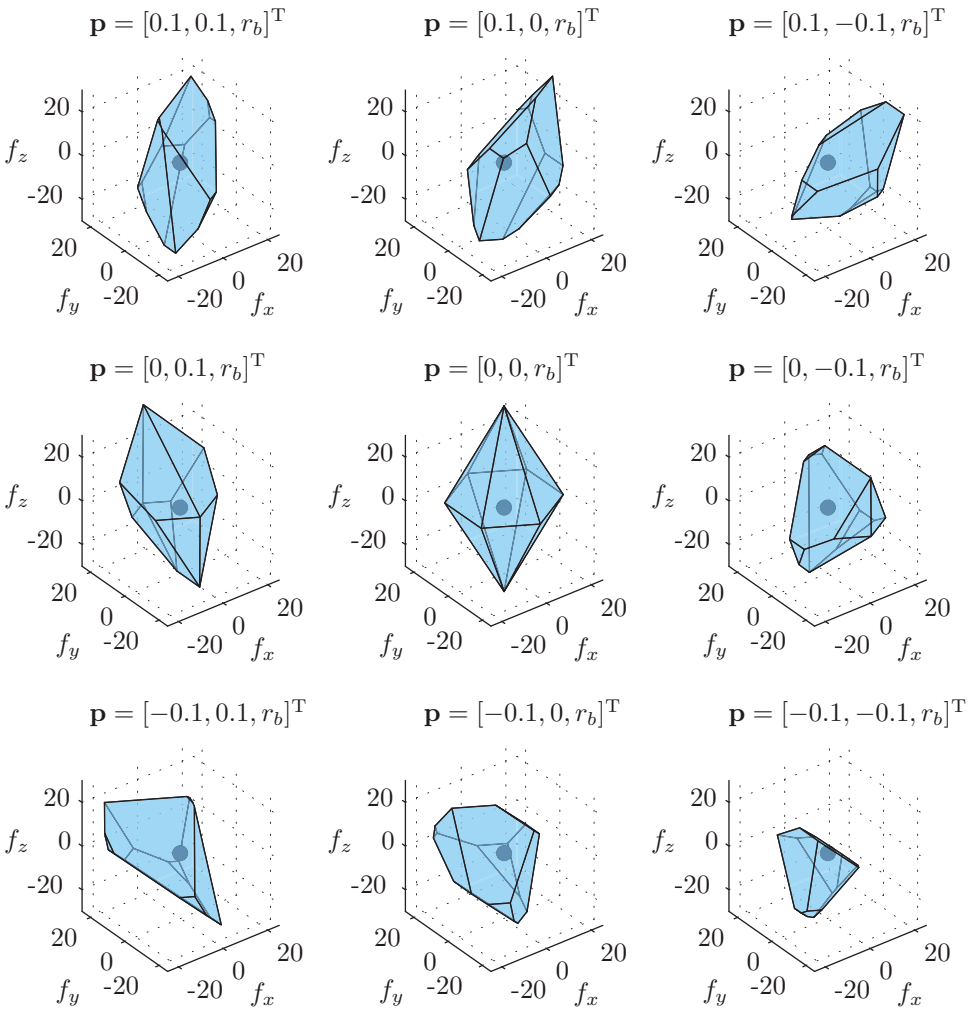

Figure 4.5: Characteristic force-only zonotopes and their corresponding mechanism poses. Based on parameters in Table 4.1. All forces are in Newtons.

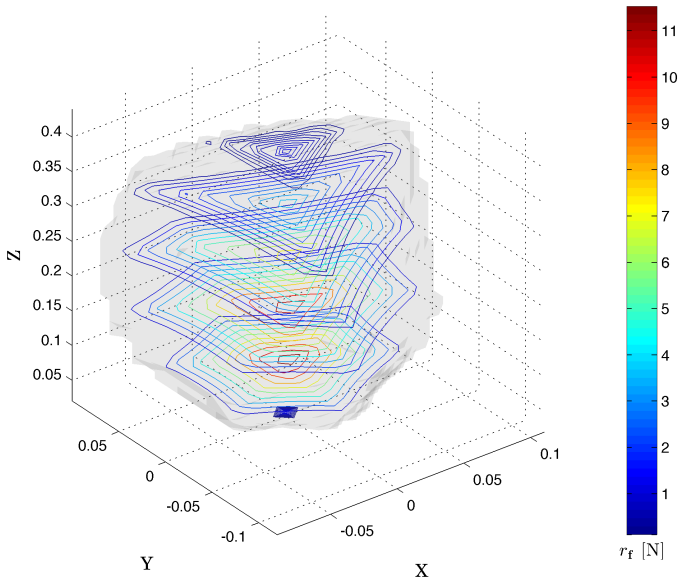

(a) Contour slices of r_f

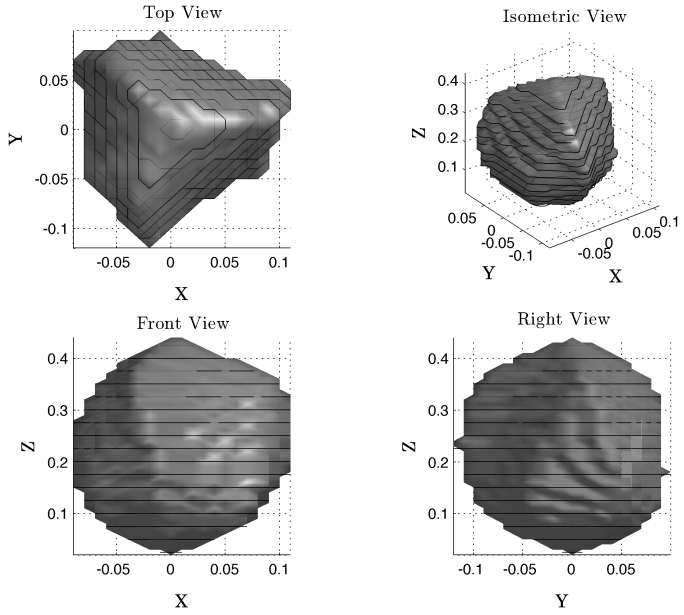

(b) Surface formed by $r_f = 0$

Figure 4.6: Force capabilities over the static workspace when the mechanism is standing (weight tends to decrease cable tension).

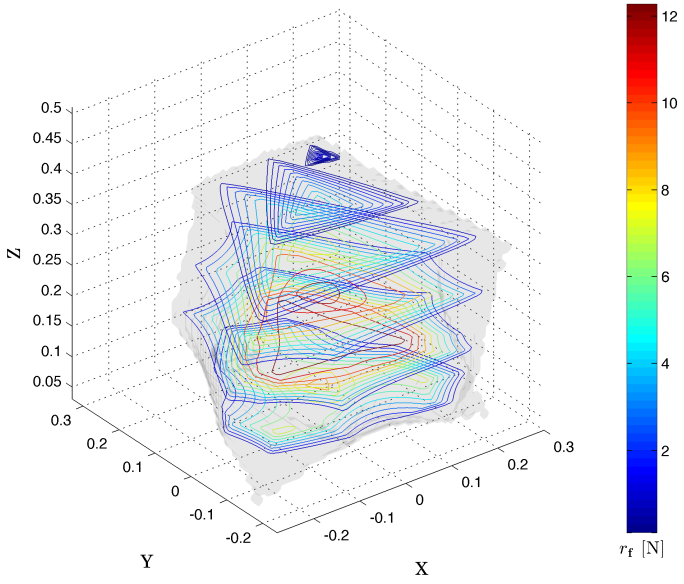

(a) Contour slices of r_f

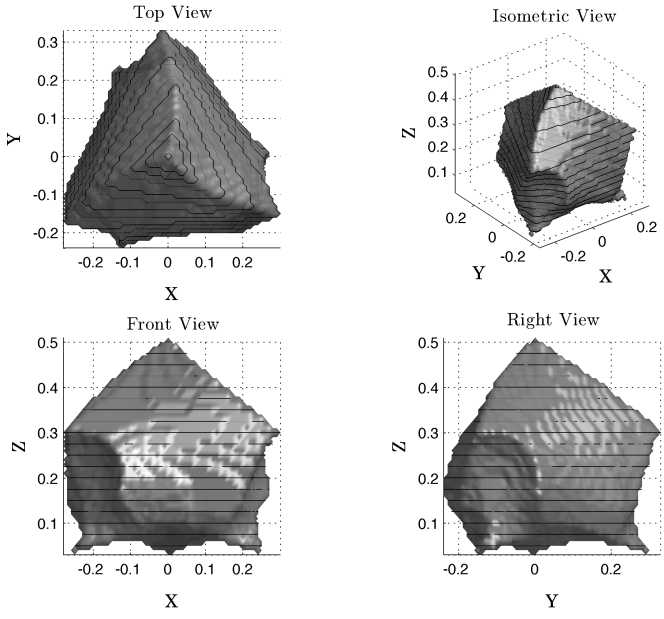

(b) Surface formed by $r_f = 0$

Figure 4.7: Force capabilities over the static workspace when the mechanism is hanging (gravity tends to increase tension).

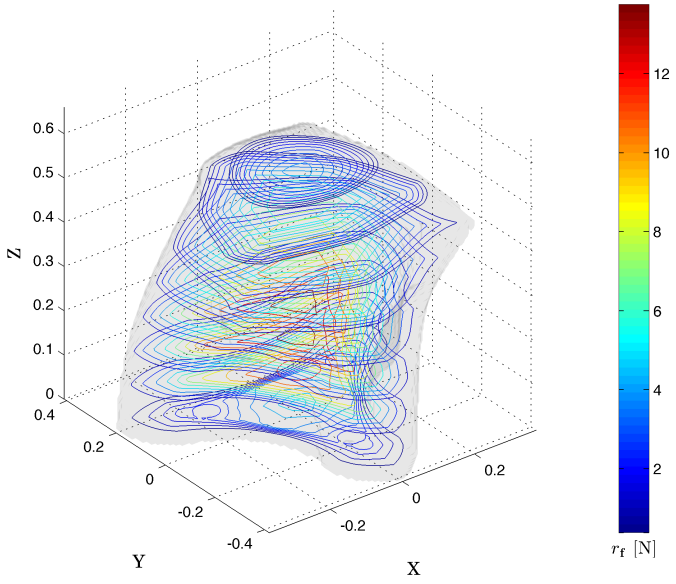

(a) Contour slices of r_f

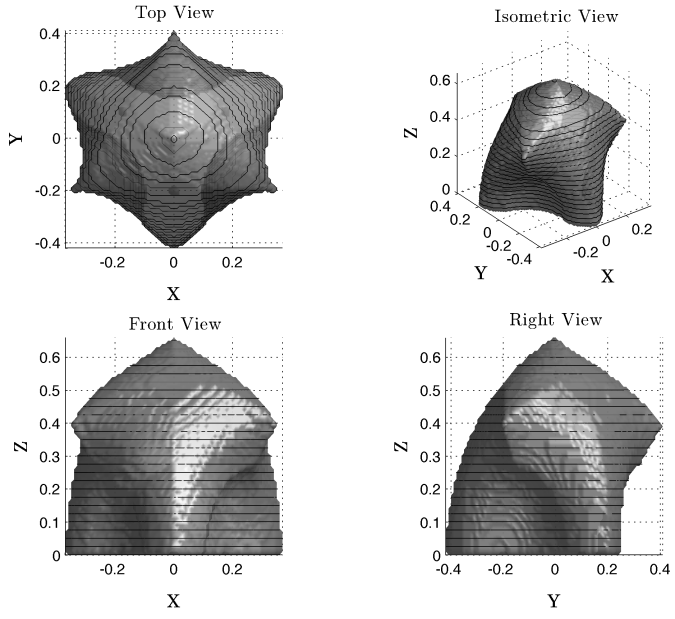

(b) Surface formed by $r_f = 0$

Figure 4.8: Force capabilities over the static workspace when gravity is ignored.

requirement that the mechanism need only support itself and no load. This is where the effect of gravity on the shape and size of the static workspace may be seen most clearly. Figure 4.6 shows that when the mechanism is "standing" the overall size of the workspace is reduced substantially. This is due to the weight of the spring legs and end-effector, which are not negligible for the designed prototype, and which tend to decrease cable tension.

The weight of the spring legs also introduces an interesting distortion to the contours of r_f. When looking at the top views of Figures 4.6b and 4.7b a clockwise twist of the workspace boundary can be observed. This is due the offset mass of the spring legs and their assembly mode, i.e., the direction that they fold. It is therefore not present in the case that does not consider gravity.

When the mechanism is instead considered to be hanging, or when gravity is neglected, the static workspace is much larger in size. As predicted, the weight of the spring legs act to increase prestress if the mechanism's base is located above its workspace. The volume also begins to show some of the features of the theoretical boundaries of the kinematic workspace boundaries in Chapter 3, i.e., the pyramid-like shape and the voids that appear centred around the mechanism's base nodes.

The results can be validated by using Equation 4.10 to independently derive the static workspace boundaries. By assuming no external forces or moments the set of poses that satisfy this equation while keeping cable tension within the allowable limits is analogous to the boundary formed by the zonotope method when r_f approaches zero. For example, Figure 4.9 shows the computed workspace boundary for the case where gravity is ignored based on the wrench equation instead of AWS. The cable tensions were calculated for a number of poses and tension limits were enforced by rejecting all poses where the vector inequality $\underline{\mathbf{t}} \leq \mathbf{t} \leq \overline{\mathbf{t}}$ was not satisfied. The resulting volume appears very similar to Figure 4.8b, ignoring the difference in resolution of the grids used.

The tension data generated allows us to investigate the effect that the upper and lower tension limits have on the workpace volume. Figure 4.10 shows the workspace volume for different tension ranges. From these plots it can be seen that increasing the upper tension limit tends to expand the static boundary and push it toward the kinematic boundaries. Increasing the lower tension limit tends to shrink the bottom portion of the workspace boundary. For example, setting $\mathbf{t} \in [10, 15]$ N causes the workspace to detach from the base plane and become a rounded shape. This is not unlike the plot of the workspace when prestress is decreased by the weight of the spring legs.

In summary, the static workspace has been shown to exist and therefore contains the subset of poses for which the translational motion assumption is

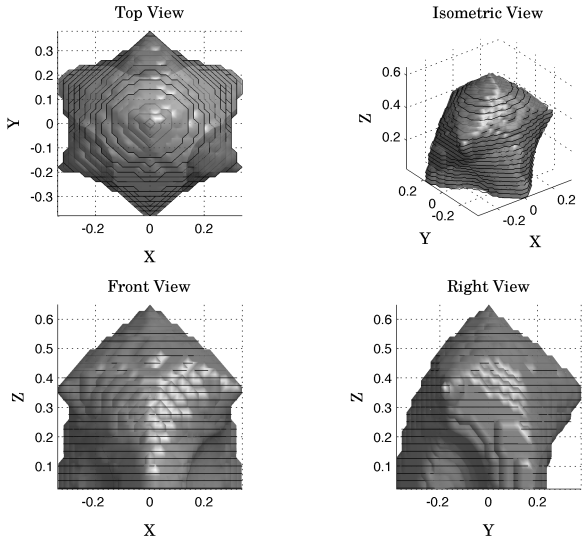

Figure 4.9: Views of the static workspace boundary ($t \in [1, 20]$, $\mathbf{w}_e = 0$, no gravity) derived using the wrench equation based method.

valid. Calculating cable tensions directly or generating the available wrench set both offer insight into the force capabilities of the mechanism throughout its workspace. These methods also help us understand the impact of several design factors, e.g., tension limits, mechanism weight, and the direction of gravity.

4.3 Mechanism Stiffness

Stiffness is the relationship between forces applied at the end-effector and any resulting displacements of the mechanism away from the commanded pose. In typical tasks, such as attempting to closely follow trajectories and manipulate objects, the positional accuracy is very important and thus a high stiffness is desired. Other applications may require the inverse to be true. Compliance (the inverse of stiffness) could be desired so that if a mechanism comes in contact with an object it will deflect rather than apply damaging forces, or so compensation methods may be applied to reduce positional inaccuracies. Regardless, stiffness is an important tool for the designer to use when optimizing mechanism architecture, choosing materials or selecting actuators.

In the case of tensegrity or cable-driven mechanisms the stiffness becomes

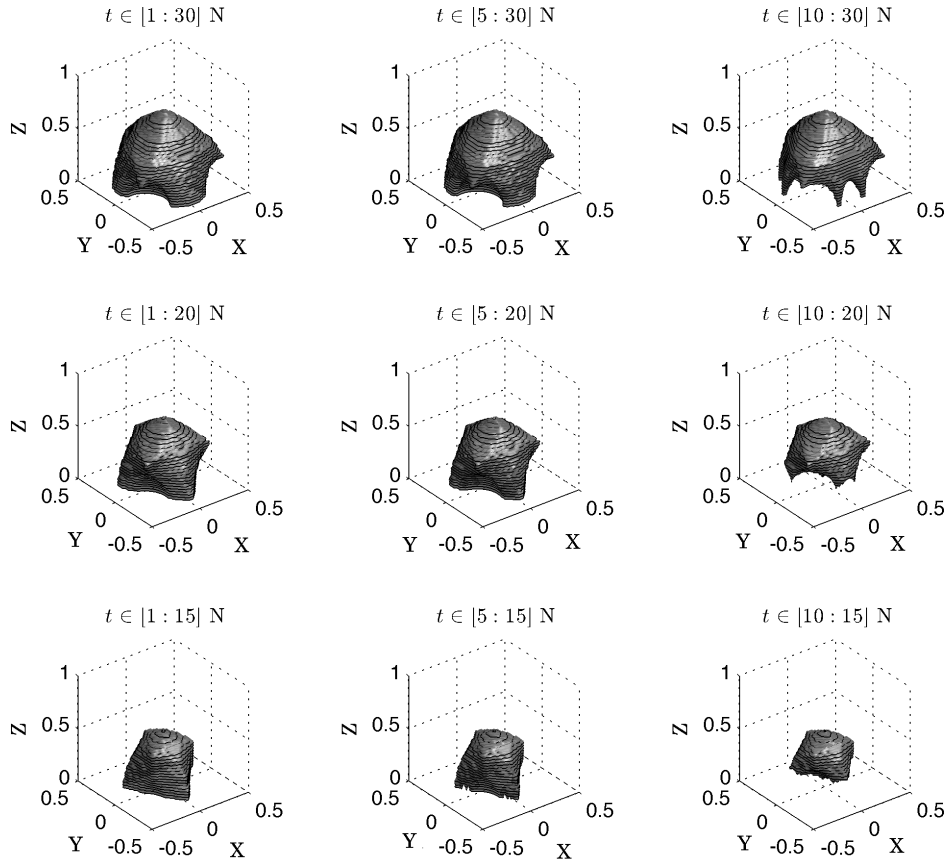

Figure 4.10: Views of the static workspace boundary ($\mathbf{w}_e = 0$, no gravity) for various allowable ranges of cable tension.

more significant because their elements, i.e., cables, are typically much more elastic than those of rigid link manipulators. Furthermore, in the case of the tensegrity mechanism being investigated, the rotational stiffness is of interest since it will determine how well the assumption of translational motion holds. This section provides a method of calculating the stiffness of the mechanism and mapping it over the workspace.

4.3.1 Derivation of the Stiffness Matrix

Applied wrenches (i.e., forces and moments) are related linearly to deflections (i.e., translational and rotational) by the stiffness matrix, $\mathbf{K}$, of the mecha-

nism. Numerous methods of deriving this matrix exist. In this thesis a method by Huang et al. [76] will be used.

To start, if energy is to be conserved (ignoring frictional losses) then the work done by an external wrench $\mathbf{w}$ to cause an infinitesimal displacement $d\mathbf{x}$ of the end-effector must be equal to the work done by the actuators forces $\mathbf{t}^*$ to change the actuator lengths $d\mathbf{q}$. Therefore:

$$\mathbf{w}^{\mathrm{T}} d\mathbf{x} = \mathbf{t}^{*\mathrm{T}} d\mathbf{q} \tag{4.26}$$

where the spring legs will be considered actuators, such that $\mathbf{t}^*$ includes both the cable tensions and the compressive forces:

$$\mathbf{t}^* = [t_1, t_2, \ldots, f_1, f_2, f_3]^{\mathrm{T}} \tag{4.27}$$

and $d\mathbf{q}$ will include small changes in the cable lengths and the virtual spring lengths:

$$d\mathbf{q} = [d\rho_{23}, d\rho_{13}, d\rho_{12}, d\rho_{32}, d\rho_{31}, d\rho_{21}, dl_1, dl_2, dl_3]^{\mathrm{T}} \tag{4.28}$$

where $d\rho_{ij}$ is the change in length in the cable between nodes i and j, and dl_i is the change in the virtual length of the ith spring leg.

From the kinematic definition of the mechanism the relationship between the end-effector displacement and the change in cable and spring lengths is:

$$d\mathbf{x} = \frac{\partial \mathbf{x}}{\partial \mathbf{q}} d\mathbf{q} = \mathbf{W}_K^{-\mathrm{T}} d\mathbf{q} \tag{4.29}$$

which, when substituted into Equation 4.26, gives:

$$\begin{aligned} \mathbf{w}^{\mathrm{T}} \mathbf{W}_K^{-\mathrm{T}} d\mathbf{q} &= \mathbf{t}^{*\mathrm{T}} d\mathbf{q} \\ \mathbf{w}^{\mathrm{T}} \mathbf{W}_K^{-\mathrm{T}} &= \mathbf{t}^{*\mathrm{T}} \\ \mathbf{W}_K^{-1} \mathbf{w} &= \mathbf{t}^* \\ \mathbf{w} &= \mathbf{W}_K \mathbf{t}^* \end{aligned} \tag{4.30}$$

It is important to note that the wrench matrix $\mathbf{W}_K$ differs from the wrench matrix in the equation $\mathbf{w} = \mathbf{W}\mathbf{t}$ because it includes columns that account for the forces of the spring legs:

$$\mathbf{W}_K = \begin{bmatrix} \mathbf{W} & \begin{matrix} \mathbf{u}_1 \\ \mathbf{b}_1 \times \mathbf{u}_1 \end{matrix} & \begin{matrix} \mathbf{u}_2 \\ \mathbf{b}_2 \times \mathbf{u}_2 \end{matrix} & \begin{matrix} \mathbf{u}_3 \\ \mathbf{b}_3 \times \mathbf{u}_3 \end{matrix} \end{bmatrix} \tag{4.31}$$

The end goal of this exercise is to get the overall end-effector stiffness, $\mathbf{K}_p$, which is defined as:

$$\mathbf{K}_p = \frac{d\mathbf{w}}{d\mathbf{x}} \tag{4.32}$$

Taking the differential form of Equation 4.30 as follows:

$$d\mathbf{w} = d\mathbf{W}_K\mathbf{t}^* + \mathbf{W}_K d\mathbf{t}^* \tag{4.33}$$

and substituting in the definition of the overall stiffness matrix yields the following expression:

$$\mathbf{K}_p d\mathbf{x} = d\mathbf{W}_K\mathbf{t}^* + \mathbf{W}_K d\mathbf{t}^* \tag{4.34}$$

This result shows that the overall stiffness matrix is the sum of two other matrices.

The first term, $d\mathbf{W}_K\mathbf{t}^*$, can be interpreted as containing the geometric stiffness, i.e., the apparent stiffness caused by small changes in the mechanism's pose due to the internal forces in its components. Expanding it as a partial differential gives:

$$d\mathbf{W}_K\mathbf{t}^* = \sum_i \frac{\partial \mathbf{W}_K}{\partial x_i}\mathbf{t}^* dx_i \tag{4.35}$$

from which we define the geometric stiffness matrix, $\mathbf{K}_g$, as:

$$\mathbf{K}_g = \left[\frac{\partial \mathbf{W}_K}{\partial x_1}\mathbf{t}^*, \frac{\partial \mathbf{W}_K}{\partial x_2}\mathbf{t}^*, \dots\right] \tag{4.36}$$

so that the term can be rewritten as:

$$d\mathbf{W}_K\mathbf{t}^* = \mathbf{K}_g d\mathbf{x} \tag{4.37}$$

The second term requires us to define the joint stiffness, $\mathbf{K}_q$, as:

$$\mathbf{K}_q = \frac{d\mathbf{t}^*}{d\mathbf{q}} = \mathrm{diag}(k_1, k_2, \dots, k_{s1}, k_{s2}, k_{s3}) \tag{4.38}$$

where k_i is the stiffness of the ith cable:

$$k_i = \frac{EA}{l_i} \tag{4.39}$$

with E being the elastic modulus of the cable material and A being it's cross-sectional area. The effective stiffness of the virtual springs, $k_{s,i}$, is found by differentiating Equation 4.3 as follows:

$$k_{si} = \frac{df_i}{dl_i} = \frac{4\kappa}{l_0^2\left[1 - \left(\frac{l_i}{l_0}\right)^2\right]} + \frac{2\kappa\left[2\arcsin\left(\frac{l_i}{l_0}\right) - \pi\right]}{l_0^3\left[1 - \left(\frac{l_i}{l_0}\right)^2\right]^{\frac{3}{2}}} \tag{4.40}$$

Applying these definitions of the overall, joint and geometric stiffness matrices, Equation 4.33 is now:

$$\mathbf{K}_p d\mathbf{x} = \mathbf{K}_g d\mathbf{x} + \mathbf{W}_K \mathbf{K}_q \mathbf{W}_K^{\mathrm{T}} d\mathbf{x} \tag{4.41}$$

This means that the overall stiffness matrix can be extracted as:

$$\mathbf{K}_p = \mathbf{K}_g + \mathbf{W}_K \mathbf{K}_q \mathbf{W}_K^{\mathrm{T}} \tag{4.42}$$

The analytical forms of the matrix $\mathbf{W}_K$, the joint stiffness $\mathbf{K}_q$, and the force vector $\mathbf{t}^*$ are readily available and, with the assistance of Maplesoft Maple, the geometric stiffness terms in Equation 4.36 were also derived. Calculation of the overall stiffness matrix is then done numerically.

Another method of deriving the stiffness matrix, by Svinin et al. [77], was considered. Their method uses vector mechanics to arrive at a more detailed analytical derivation of the stiffness matrix for generalized Gough-Stewart platforms, which gives more insight into the individual contributions of a mechanism's elements. In the end the Svinin method was implemented primarily to verify the numerical results calculated using the CCT derivation. In all test cases the two methods were in agreement and the difference between the elements of the calculated stiffness matrices were on the order of 0.01%. This can be attributed to numerical error and therefore shows that the two methods support each other.

4.3.2 Stiffness Indices

It is difficult to make conclusions about the mechanism stiffness simply from the numerical stiffness matrix. Instead it is more helpful to extract a numerical index to gain a more intuitive impression of the stiffness. For example, knowing the minimum or maximum stiffness in a given direction is far more useful.

Since the mechanism stiffness considers both translational and rotational displacements the derived stiffness matrix suffers from non-homogeneous units. This problem is similar to the issue with quantifying the available wrench set, which includes both forces and moments. The solution is to partition the stiffness matrix so that rotational and translational stiffness can be separated. For example, matrix $\mathbf{K}_p$ can be partitioned as:

$$\mathbf{K}_p = \left[\begin{array}{c:c} \mathbf{K}_{\mathbf{xx}} & \mathbf{K}_{\mathbf{x}\boldsymbol{\theta}} \\ \hdashline \mathbf{K}_{\boldsymbol{\theta}\mathbf{x}} & \mathbf{K}_{\boldsymbol{\theta}\boldsymbol{\theta}} \end{array}\right] \tag{4.43}$$

where the sub-matrices are then used to re-write the stiffness equation as:

$$d\mathbf{f} = \mathbf{K_{xx}} d\mathbf{x} + \mathbf{K_{x\theta}} d\boldsymbol{\theta} \tag{4.44}$$

$$d\mathbf{n} = \mathbf{K_{\theta x}} d\mathbf{x} + \mathbf{K_{\theta\theta}} d\boldsymbol{\theta} \tag{4.45}$$

Assuming that no moments are applied ($d\mathbf{n} = \mathbf{0}$), these equations can be rearranged to yield:

$$d\mathbf{f} = (\mathbf{K_{xx}} - \mathbf{K_{x\theta}} \mathbf{K_{\theta\theta}^{-1}} \mathbf{K_{\theta x}}) d\mathbf{x} \tag{4.46}$$

which gives the relationship between an infinitesimal force, $d\mathbf{f}$, applied to the end-effector and the resulting translational displacement, $d\mathbf{x}$. By assuming no forces are applied ($d\mathbf{f} = \mathbf{0}$), the same procedure can be used to isolate the rotational stiffness as:

$$d\mathbf{n} = (\mathbf{K_{\theta\theta}} - \mathbf{K_{\theta x}} \mathbf{K_{xx}^{-1}} \mathbf{K_{x\theta}}) d\boldsymbol{\theta} \tag{4.47}$$

where $d\mathbf{n}$ is an infinitesimal moment and $d\boldsymbol{\theta}$ is the resulting rotation. The same partitioning procedure can be repeated to isolate the stiffness in any subset of the coordinates. The stiffness can be extracted in a single Cartesian direction, about a single axis of rotation, or in certain planes (e.g., the xy plane). The stiffness in arbitrary directions can also be extracted [78] from the stiffness matrix, so long as it has homogeneous units.

Instead of calculating directional stiffness, it is also useful to calculate the overall minimum or maximum stiffness. So long as the stiffness matrix has consistent units, its minimum and maximum eigenvalues ($\lambda_{\min}$ and $\lambda_{\max}$) correspond to the minimum and maximum stiffness values, respectively. The matrix's eigenvectors therefore represent the direction in which these values occur. From this the condition number, η, of the stiffness matrix is defined as:

$$\eta = \frac{k_{\min}}{k_{\max}} = \frac{\lambda_{\min}}{\lambda_{\max}} \tag{4.48}$$

where $k_{\min}$ and $k_{\max}$ are the magnitudes of the stiffness in the minimum and maximum directions. By definition, the condition number has a range of $0 \leq \eta \leq 1$ and gives a measure of how uniform the stiffness is in different directions. Without knowledge of the application, a condition number close to 1 may be desirable to keep stiffness roughly uniform in all directions. Keep in mind that even though it may be desirable to have a condition number closer to 1, lower condition numbers do not necessarily suggest anything about the absolute values of the minimum and maximum stiffness, only their relative values.

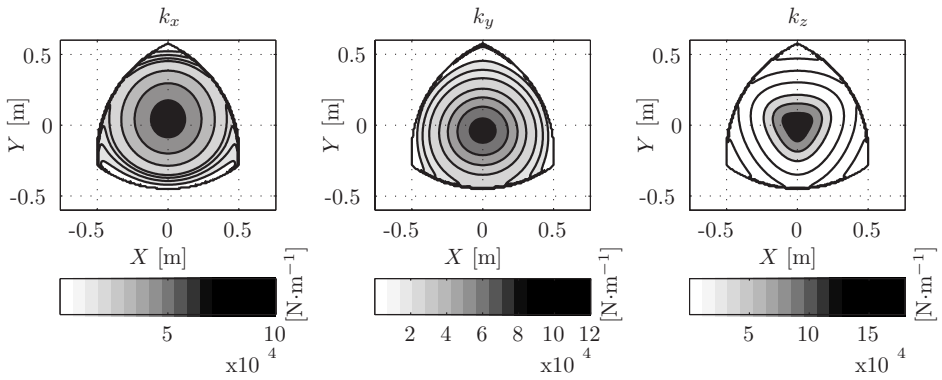

Figure 4.11: Stiffness in the direction of the three Cartesian axes, mapped on a horizontal plane at $z = 0.15$ m.

4.3.3 Stiffness Mapping

Using these single value indices to visualized the stiffness over the mechanism's workspace is referred to as mapping [79]. In this section several stiffness maps are generated and discussed. All of the stiffness calculations are based on the mechanism parameters from the prototype, listed in Table 4.1.

To start, the stiffness in the three Cartesian axes directions will be explored. Assuming translational motion of the end-effector, the stiffness in Cartesian space will end up affecting nearly all manipulation tasks that the tensegrity mechanism performs. After calculating and partitioning the stiffness matrix, each directional stiffness was mapped over horizontal slices of the mechanism's workspace at heights of $z = 0.15$ and $z = 0.4$ m, as shown in in Figures 4.11 and 4.12.

The stiffness is generally higher toward the origin. This result mirrors the force capability results and makes sense since the mechanism has higher prestress in the centre of its workspace than at its boundaries. There are also slight asymmetries in mappings of the x and y directions. This is due to the triangular construction of the mechanism's base. However, the horizontal stiffnesses are axis-symmetric, i.e., the plots will repeat themselves if generated for directions that are rotated 120° from each other.

Throughout most of the maps the stiffness in the z-direction is higher than in the xy-plane. It becomes increasingly larger than the other two directions at greater heights, e.g., comparing the k_z map in Figure 4.11 to that in Figure 4.12. Most of the mechanism's elements (i.e., cables and springs) are aligned in a direction that is close to vertical. This means that their con-

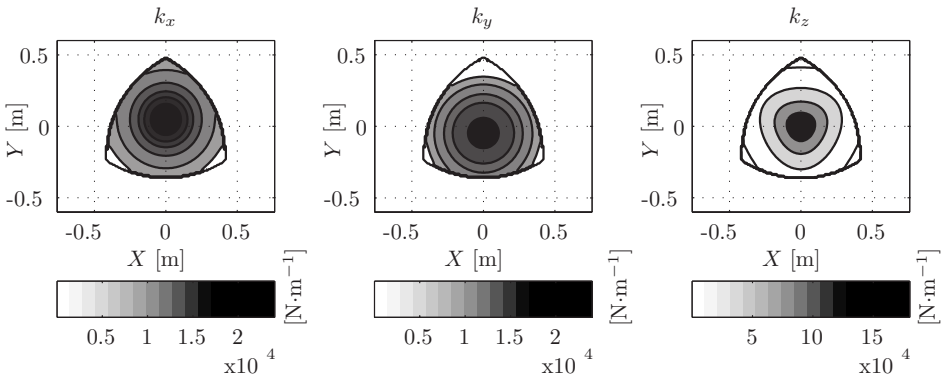

Figure 4.12: Stiffness in the direction of the three Cartesian axes, mapped on a horizontal plane at $z = 0.4$ m.

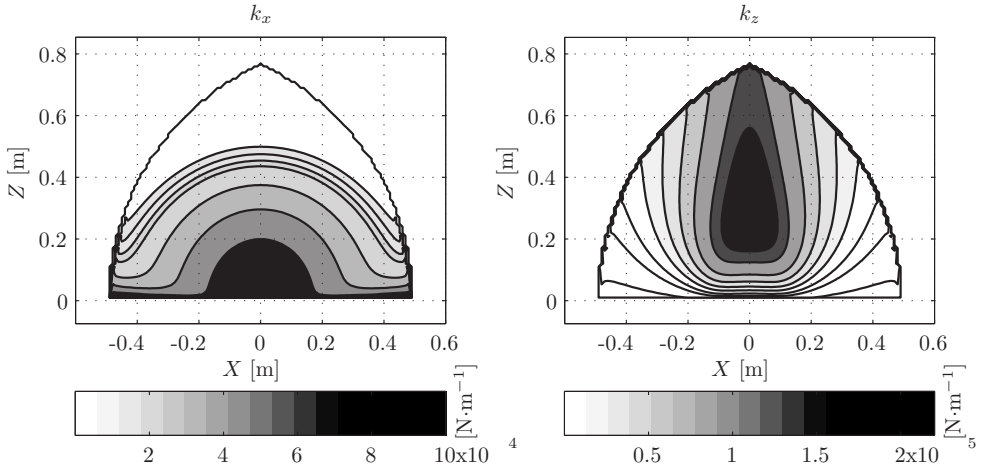

Figure 4.13: Stiffness in the x and z directions, mapped on the xz-plane through the origin.

tributions to the overall stiffness will be projected more on the z-axis rather than in the xy plane. This becomes increasingly true at higher elevations and explains why the highest value of k_z mapped at $z = 0.4$ m is nearly an order of magnitude larger than highest values of k_x or k_y.

Figure 4.13 shows the mapping of k_x and k_z onto the vertical xz-plane. These plots support the reasoning that the average orientation of the mechanism's elements has the greatest influence on the stiffest directions. The k_z mapping shows that stiffness in the z-direction is fairly constant with height,

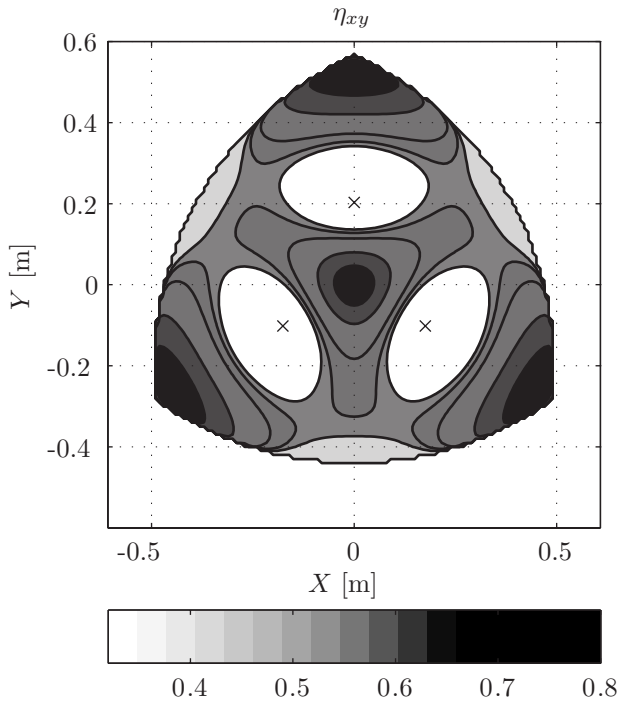

Figure 4.14: Condition number of the $\mathbf{K}_{xy}$ stiffness matrix, mapped on a horizontal plane at $z = 0.15$ m.

until reaching the top boundary of the workspace. The slight decrease at the top makes sense since the cables and spring legs can never all become completely vertical and eventually the spring leg contribution decreases. The k_x stiffness remains high at lower elevations and at positions further away from the z-axis.

The condition number of the full Cartesian stiffness matrix will be relatively low. This is because the vertical stiffness tends to be much higher than the horizontal stiffness, as observed in the Cartesian stiffness maps. However, the condition number of the planar stiffness matrix $\mathbf{K}_{xy}$ may be of more interest. As shown in Figure 4.14 the condition number was mapped across a horizontal plane.

For the most part, the condition number remains above ≈ 0.55, confirming that the stiffness in the xy plane is relatively uniform. The exception to this are the three areas where the condition number drops below ≈ 0.3, which are centred roughly around the location of the mechanism's base nodes, marked on

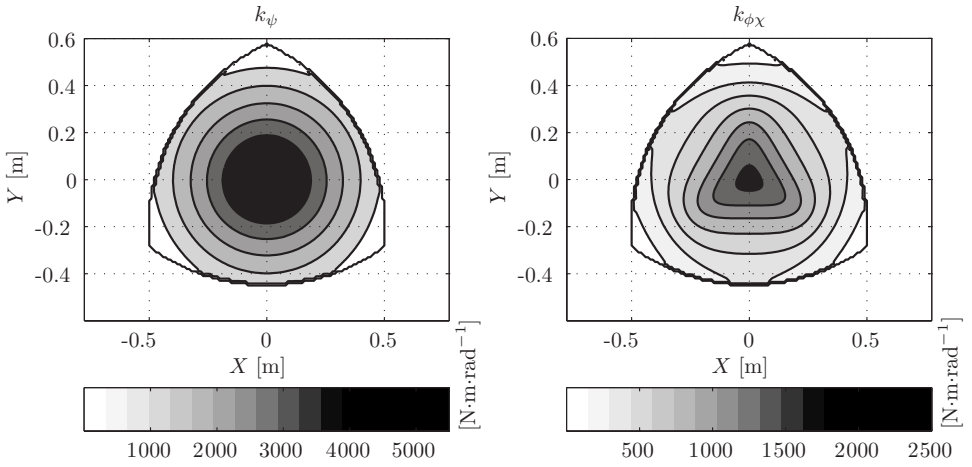

Figure 4.15: Rotational stiffness about the z-axis and minimum rotational stiffness out of the horizontal plane (i.e., $\mathbf{K}_{\phi\chi}$), mapped on a horizontal plane at $z = 0.15$ m.

the mapping by crosses. The co-location may be explained by the orientation of the mechanism's cables when the end-effector is positioned over one of these nodes.

Consider a plane formed by the two cables that terminate at any given node. As the xy coordinates of the end-effector approach the location of this node, the cable plane will become closer to being parallel to the z-axis. The cables in the plane and their matching pairs will all act in this plane. However, the two other cables will be close to perpendicular to this plane, suggesting that in-plane stiffness may be very different from the out of plane stiffness.

In addition to the Cartesian stiffness, the rotational stiffness of the mechanism is also of interest. Most importantly it can show how likely the end-effector is to remain in translation only when subjected to small external moments. As a reminder, the rotation angles ϕ, χ, ψ are defined around the body-fixed axes X', Y', and Z', respectively. This means that the angles ϕ and χ represent rotation of the end-effector away from being parallel with the base. The angle ψ represents a twisting of the end-effector with respect to the base. The rotational stiffness, in both out of plane rotations and twisting, is shown in Figure 4.15.

Both rotational stiffness maps are symmetric and higher toward the origin. The $k_{\phi\chi}$ stiffness being plotted is actually the minimum out of plane stiffness. While the stiffness in the individual angular directions may be less symmetric,

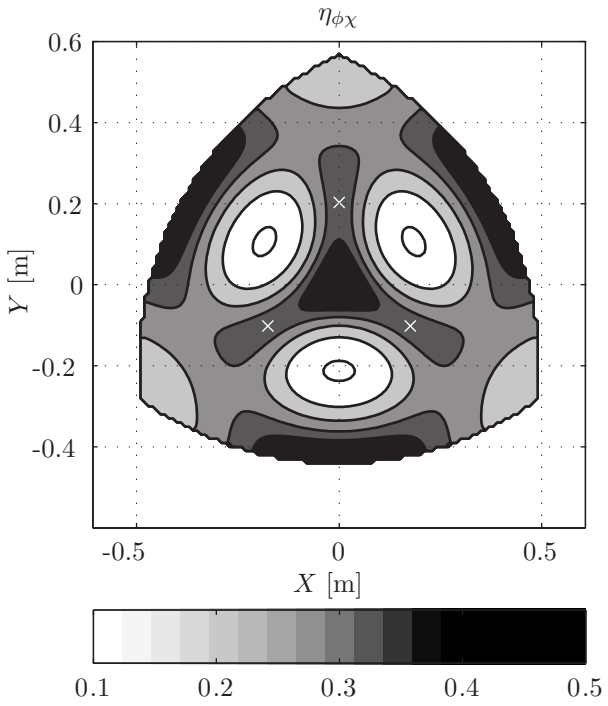

Figure 4.16: Condition number of the $\mathbf{K}_{\phi\chi}$ (rotational) stiffness matrix, mapped on a horizontal plane at $z = 0.15$ m.

they do not hold much significance on their own. From the maps it appears that the end-effector is unlikely to leave translational motion as a result of small moments, especially if most of its used workspace is closer to the z-axis.

The condition number of the out of plane stiffness was mapped in Figure 4.16. It exhibits a similar appearance to the condition mapping of the Cartesian planar stiffness but shows that the rotational stiffness is, in general, much less uniform. There are again areas of much lower uniformity, but this time they are located midway between the base nodes, marked as white crosses.

The stiffness results suggest that the prototype mechanism is fully capable of resisting small external moments. These could arise from offset or irregular payloads and end-of-arm tooling. The indices and mapping also provide optimization tools. In the future these could prove invaluable when attempting to customize the mechanism to specific applications.

5 Dynamic Analysis

The previous chapter described the conditions required to maintain tension under static loading. This chapter will consider the dynamics of the mechanism and the influence that it has on the cable tensions during movement. A dynamic model of the mechanism is derived and used to verify that cables remain in tension while following end-effector trajectories. Several trajectories were generated to be representative of typical manipulator motions. Additionally, a series of reciprocating linear trajectories were created to test the acceleration limits of the mechanism. The speed of these motions was incrementally increased until tension was lost during a simulation. The results are compared and discussed. Additionally, the potential incorporation of the dynamic model into the control algorithm is examined.

5.1 Development of the Dynamic Model

In Chapter 3, the direct kinematic problem was solved using a constrained optimization process. The constraints posed by the actuated cables were represented in Equations 3.10-3.15 as holonomic functions of the form $\phi(\mathbf{x}, t) = 0$ where $\mathbf{x}$ was defined in Equation 3.5. These constraint functions imply that the cables will constrain the mechanism regardless of their tension, which is not incorrect. However, for the purposes of this thesis we are only interested in positions or trajectories that maintain positive tension in all cables so that the mechanism remains fully actuated and controllable. As such, the constraints will continue to be used as defined with the understanding that the dynamic model ceases to be valid as soon as any cable loses tension.

With this assumption, the mechanism can be interpreted as a Stewart-Gough platform with massless prismatic actuators and three redundant, passive limbs (i.e., the spring linkages). The cable lengths are still actuated in pairs, but will be considered independent for the derivation of the model. There are many examples throughout literature of deriving dynamic models

for the Stewart-Gough platform [80–82]. A Lagrangian approach is used in this thesis for ease of derivation. The approach will derive the energies of the end-effector and each spring leg separately and then combine them without needing to consider reaction forces between bodies.

First, the kinetic and potential energy of the end-effector platform are derived. The end-effector is represented as a rigid disc of radius r_b, with uniform density and a mass of m_e. The coordinates selected to describe the end-effector are the same used throughout this thesis: the Cartesian coordinates of the centre of mass $\mathbf{p} = [x, y, z]^{\mathrm{T}}$ and the three Euler angles φ, χ, ψ about the body fixed reference frame. As a reminder, the matrix $\mathbf{Q}$ is calculated from these Euler angles, using an XYZ convention, and describes the rotation of a vector expressed in the $X'Y'Z'$ reference frame into the corresponding vector in the global reference frame X, Y, Z. The kinetic energy of the end-effector is therefore:

$$T_e = \frac{1}{2} m_e \dot{\mathbf{p}}^{\mathrm{T}} \dot{\mathbf{p}} + \frac{1}{2} \boldsymbol{\omega}_e'^{\mathrm{T}} \mathbf{I}_e' \boldsymbol{\omega}_e' \tag{5.1}$$

where $\boldsymbol{\omega}_e'$ is the angular velocity and $\mathbf{I}_e'$ the inertia tensor of the end-effector, both expressed in the body fixed reference frame as denoted by the prime, $'$, symbol.

The angular velocity can be calculated in the fixed reference frame from the time derivatives of the rotation angles as:

$$\begin{aligned} \boldsymbol{\omega}_e &= \begin{bmatrix} \mathbf{e}_\varphi & \mathbf{Q}_\varphi \mathbf{e}_\chi & \mathbf{Q}_\varphi \mathbf{Q}_\chi \mathbf{e}_\psi \end{bmatrix} \begin{bmatrix} \dot{\varphi} \\ \dot{\chi} \\ \dot{\psi} \end{bmatrix} \\ &= \begin{bmatrix} 1 & 0 & \mathrm{s}\chi \\ 0 & \mathrm{c}\varphi & -\mathrm{c}\chi\mathrm{s}\varphi \\ 0 & \mathrm{s}\varphi & \mathrm{c}\chi\mathrm{c}\varphi \end{bmatrix} \begin{bmatrix} \dot{\varphi} \\ \dot{\chi} \\ \dot{\psi} \end{bmatrix} \end{aligned} \tag{5.2}$$

where, for example, $\mathbf{e}_\varphi$, $\mathbf{e}_\chi$, and $\mathbf{e}_\psi$ are the rotation axes of the respective Euler angles. To find the angular velocity with respect to the body fixed reference frame it is rotated by $\mathbf{Q}^{\mathrm{T}}$:

$$\boldsymbol{\omega}_e' = \mathbf{Q}^{\mathrm{T}} \boldsymbol{\omega}_e \tag{5.3}$$

The inertia tensor for the thin disc end-effector about its centre of mass is defined as:

$$\mathbf{I}_e' = m_e r_b^2 \begin{bmatrix} \frac{1}{4} & 0 & 0 \\ 0 & \frac{1}{4} & 0 \\ 0 & 0 & \frac{1}{2} \end{bmatrix} \tag{5.4}$$

which is already in the body fixed frame. Finally, the potential energy of the end-effector is:

$$U_e = m_e \mathbf{g}^{\mathrm{T}} \mathbf{p} \tag{5.5}$$

where $\mathbf{g} = [0, 0, g]$ is the gravity vector.

Next, the kinetic and potential energy of the spring linkages and the springs themselves is derived. The pose of each leg is fully defined based on the location of the end-effector node to which it is connected. This is due to the selected directions of the joint axes, as discussed in Section 2.3.3. However, to assist with the energy derivations, three angles are introduced: α_i, β_i, and θ_i, as shown in Figure 5.1. These angles can be calculated given that $\mathbf{p} + \mathbf{Q}\mathbf{b}'_i$ is known (a detailed derivation of the angles can be found in Appendix A). The time derivatives can also be calculated by recognizing that the velocity of node B_i is:

$$\dot{\mathbf{b}} = \dot{\mathbf{p}} + \boldsymbol{\omega}_e \times \mathbf{Q}\mathbf{b}'_i \tag{5.6}$$

Each link is treated as slender rod of length $l_0/2$ and has its centre of mass at its midpoint. The mass of the proximal link is m_p and the mass of the distal link is m_d. One end of the proximal link is located at the base node A_i while the other end locates node C_i. In Chapter 2 C_i was also defined as the location of the torsion spring joint. In the global reference frame this node is located by the vector $\mathbf{c_i}$ and can be calculated using only the angles α_i and β_i. The distal link is then connected to this node and the end-effector. The angle between the proximal and distal links is $2\theta_i$.

Given $\mathbf{c_i}$, the locations of the centres of mass of the proximal, $\mathbf{c}_{pi}$, and distal, $\mathbf{c}_{di}$, links are defined as:

$$\mathbf{c}'_{pi} = \frac{\mathbf{c}_i + \mathbf{a}_i}{2} \tag{5.7}$$

$$\mathbf{c}'_{di} = \frac{\mathbf{c}_i + \mathbf{p} + \mathbf{Q}\mathbf{b}_i}{2} \tag{5.8}$$

Using the definitions of $\dot{\alpha}_i, \dot{\beta}_i, \dot{\theta}_i$, the angular velocities in the body fixed reference frames can be found as:

$$\boldsymbol{\omega}'_{pi} = \begin{bmatrix} \mathrm{c}\beta_i\dot{\alpha}_i & \dot{\beta}_i & \mathrm{s}\beta_i\dot{\alpha}_i \end{bmatrix}^{\mathrm{T}} \tag{5.9}$$

$$\boldsymbol{\omega}'_{di} = \begin{bmatrix} -\mathrm{c}(\beta_i + 2\theta_i)\dot{\alpha}_i & \dot{\beta}_i + 2\dot{\theta}_i & -\mathrm{s}(\beta_i + 2\theta_i)\dot{\alpha}_i \end{bmatrix}^{\mathrm{T}} \tag{5.10}$$

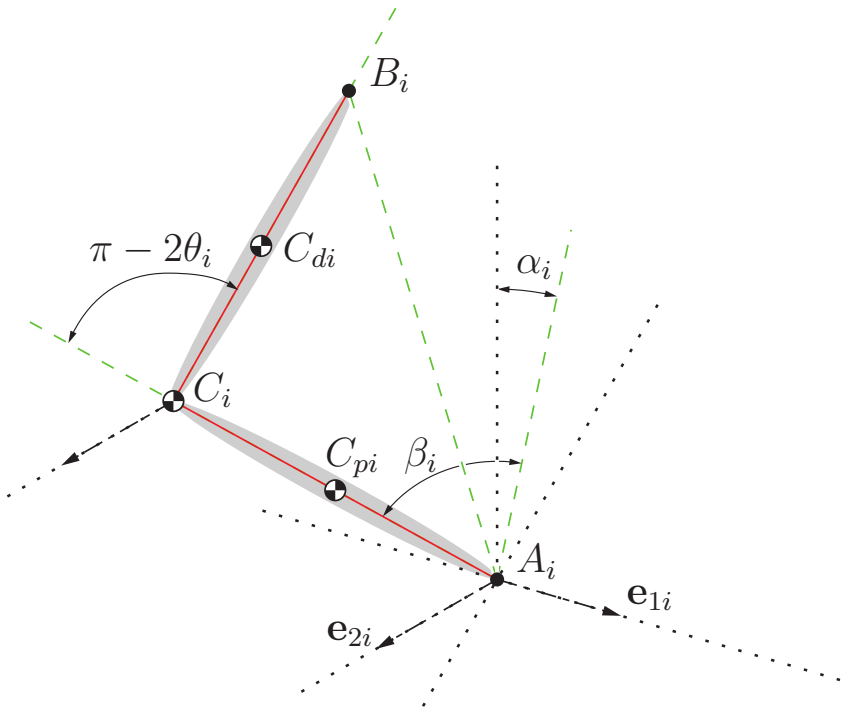

Figure 5.1: Simplified spring linkage representation used for dynamic simulation.

Using these results, the velocities of node C_i and the centres of mass of the proximal and distal links can be found as:

$$\dot{\mathbf{c}}_i = \boldsymbol{\omega}_{pi} \times (\mathbf{c}_i - \mathbf{a}_i) \tag{5.11}$$

$$\dot{\mathbf{c}}_{pi} = \frac{1}{2}\dot{\mathbf{c}}_i \tag{5.12}$$

$$\dot{\mathbf{c}}_{di} = \dot{\mathbf{c}}_i + \boldsymbol{\omega}_{di} \times \frac{1}{2}(\mathbf{p} + \mathbf{Q}\mathbf{b}'_i - \mathbf{c}_i) \tag{5.13}$$

where the angular velocities of the links, $\boldsymbol{\omega}_{pi}$ and $\boldsymbol{\omega}_{di}$, are now with respect to the global reference frame. The torsion spring joints are considered point masses, located at $\mathbf{c}_i$, and each having a mass of m_s. The kinetic energy of

all three legs is then:

$$T_l = \sum_{i=1}^{3} \left(\frac{1}{2} m_p \dot{\mathbf{c}}_{pi}^{\mathrm{T}} \dot{\mathbf{c}}_{pi} + \frac{1}{2} m_d \dot{\mathbf{c}}_{di}^{\mathrm{T}} \dot{\mathbf{c}}_{di} + \frac{1}{2} m_s \dot{\mathbf{c}}_{i}^{\mathrm{T}} \dot{\mathbf{c}}_{i} \right) + \sum_{i=1}^{3} \left(\frac{1}{2} \boldsymbol{\omega}_{pi}'^{\mathrm{T}} \mathbf{I}_p' \boldsymbol{\omega}_{pi}' + \frac{1}{2} \boldsymbol{\omega}_{di}'^{\mathrm{T}} \mathbf{I}_d' \boldsymbol{\omega}_{di}' \right) \tag{5.14}$$

where the inertia tensors $\mathbf{I}_p$ and $\mathbf{I}_d$ are defined in the body fixed reference frames as:

$$\mathbf{I}_p' = \frac{m_p l_0^2}{48} \begin{bmatrix} 1 & 0 & 0 \\ 0 & 1 & 0 \\ 0 & 0 & 0 \end{bmatrix}, \qquad \mathbf{I}_d' = \frac{m_d l_0^2}{48} \begin{bmatrix} 1 & 0 & 0 \\ 0 & 1 & 0 \\ 0 & 0 & 0 \end{bmatrix} \tag{5.15}$$

with the longitudinal axes of each link being directed along the body fixed Z axes. The potential energy of the legs is:

$$U_l = \sum_{i=1}^{3} \left(m_p \mathbf{g}^{\mathrm{T}} \mathbf{c}_{pi} + m_d \mathbf{g}^{\mathrm{T}} \mathbf{c}_{di} + m_s \mathbf{g}^{\mathrm{T}} \mathbf{c}_{i} \right) \tag{5.16}$$

The torsion springs will be treated as undamped, linear torsion springs with rotational stiffness of κ. The deflection of the spring is equal to $\pi - 2\theta_i$, making the contribution of the spring joints to the potential energy equal to:

$$U_s = \sum_{i=1}^{3} \frac{1}{2} \kappa (\pi - 2\theta_i)^2 \tag{5.17}$$

The Lagrangian derivation describes the motion of the mechanism with the following set of differential equations:

$$\frac{d}{dt} \frac{\partial T}{\partial \dot{\mathbf{x}}} - \frac{\partial T}{\partial \mathbf{x}} + \frac{\partial U}{\partial \mathbf{x}} = \mathbf{w}_{\mathbf{x}} \tag{5.18}$$

where T and U are the total kinetic and potential energy of the mechanism:

$$T = T_e + T_l \tag{5.19}$$

$$U = U_e + U_l + U_s \tag{5.20}$$

and $\mathbf{x}$ is the vector of coordinates defined in Equation 3.5. The term $\mathbf{w}_{\mathbf{x}}$ is the generalized force that accounts for the cable tensions and any external forces:

$$\mathbf{w}_{\mathbf{x}} = \mathbf{W}\mathbf{t} - \mathbf{w}_e \tag{5.21}$$

where $\mathbf{W}$ is the wrench matrix derived in Equation 4.7. To consider rotation of the end-effector, each $\mathbf{b}_i$ term in Equation 4.7 is replaced with $\mathbf{Q}\mathbf{b}'_i$. Expanding Equation 5.18 and collecting terms allows the equations of motion to be written in their final form:

$$\mathbf{M}(\mathbf{x})\ddot{\mathbf{x}} + \mathbf{V}(\mathbf{x}, \dot{\mathbf{x}}) + \mathbf{G}(\mathbf{x}) = \mathbf{W}\mathbf{t} - \mathbf{w}_e \tag{5.22}$$

5.2 Simulation Results

The inverse dynamic problem is defined as calculating the actuator forces (i.e., cable tensions) from the dynamic model when an end-effector trajectory is provided. If the first and second time derivatives of a trajectory $\mathbf{x}(t)$ are known, solving this problem becomes trivial:

$$\mathbf{t} = \mathbf{W}^{-1}\left[\mathbf{M}\ddot{\mathbf{x}} + \mathbf{V}(\mathbf{x}, \dot{\mathbf{x}}) + \mathbf{G}(\mathbf{x}) + \mathbf{w}_e\right] \tag{5.23}$$

so long as the mechanism isn't in a singularity, i.e., the inverse $\mathbf{W}^{-1}$ exists. While there is no specific task or application planned for the mechanism, several sample trajectories will be used as examples of end-effector motion. In each case the orientation of the end-effector will be kept constant and no external wrenches will be considered, i.e., $\mathbf{w}_e = 0$. The parameters values that are used were collected from the constructed prototype and are listed in Table 4.1. The mechanism is considered to be in the hanging orientation, which is reflected in the value of the gravity vector $\mathbf{g}$. The results for each trajectory were verified against a model of the mechanism that was created in MATLAB/SimMechanics, which is a multi-body dynamic simulation engine.

The first trajectory represents deployment of the end-effector. As mentioned in earlier chapters, one benefit of the tensegrity mechanism is that it can be nearly folded flat by retracting the end-effector. This would make it easier to transport. The deployment trajectory is a sinusoidal motion along the vertical axis, starting from rest:

$$x(t) = y(t) = 0, \qquad z(t) = z_0 + \frac{H}{2}\left[1 - \cos\left(2\pi\frac{t}{T}\right)\right] \tag{5.24}$$

where H is the peak-to-peak amplitude of the motion, T is the period of the motion, and z_0 is the minimum height. The minimum height z_0 is chosen to be greater than zero because the XY plane is a known singularity, which would cause numerical difficulties with the model. Simulation results for $H = 0.4$ m, $T = 2$ s, and $z_0 = 0.1$ m, are shown in Figure 5.2.

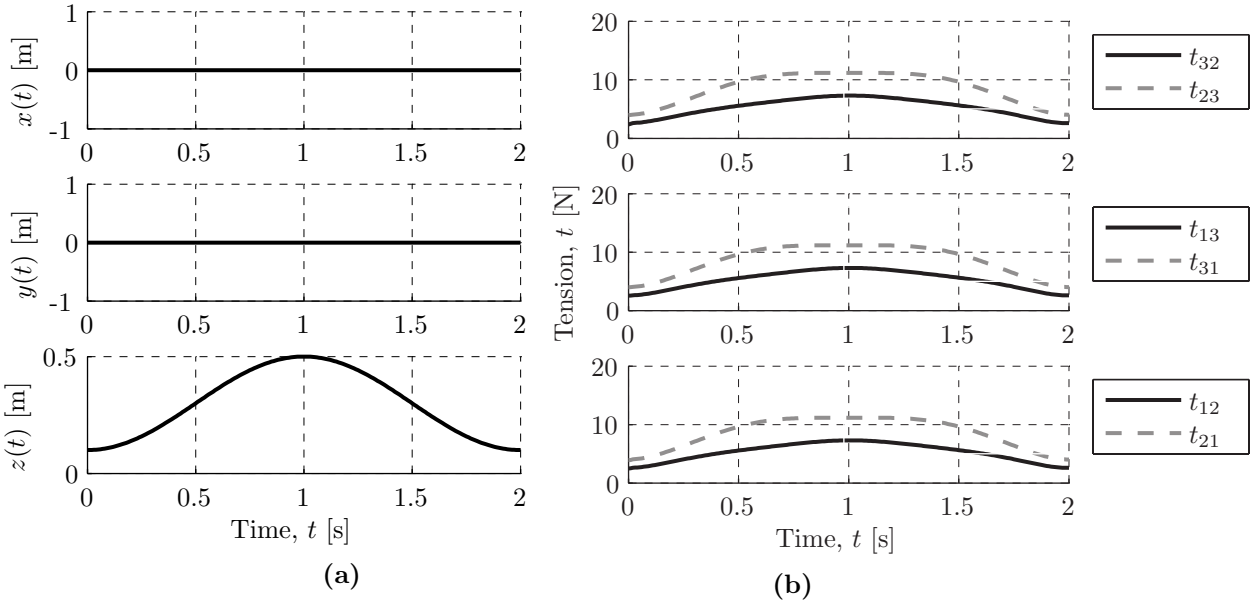

Figure 5.2: The trajectory (a) that is representative of deployment and retraction of the end-effector and the calculated cable tensions (b) required to generate it.

Next, a circular trajectory will be used to represent general movement of the mechanism in a horizontal plane. The trajectory has the end-effector tracing out a circle with constant height as follows:

$$\begin{aligned} x(t) &= R\cos\left[\pi - \pi\cos\left(\pi\frac{t}{T}\right)\right], \\ y(t) &= R\sin\left[\pi - \pi\cos\left(\pi\frac{t}{T}\right)\right], \\ z(t) &= z_0 \end{aligned} \tag{5.25}$$

where R is the radius of the circle, which is centred about the Z axis. The nested cosine functions are included so that the velocity of the trajectory at time 0 is zero, i.e., the mechanism starts from rest. Simulation results for $R = 0.1$ m, $T = 1$ s, and $z_0 = 0.2$ m, are shown in Figure 5.3.

Finally, a helical path is used to observe the cable tensions during movement in all three axes at once. The trajectory is described using the parametric

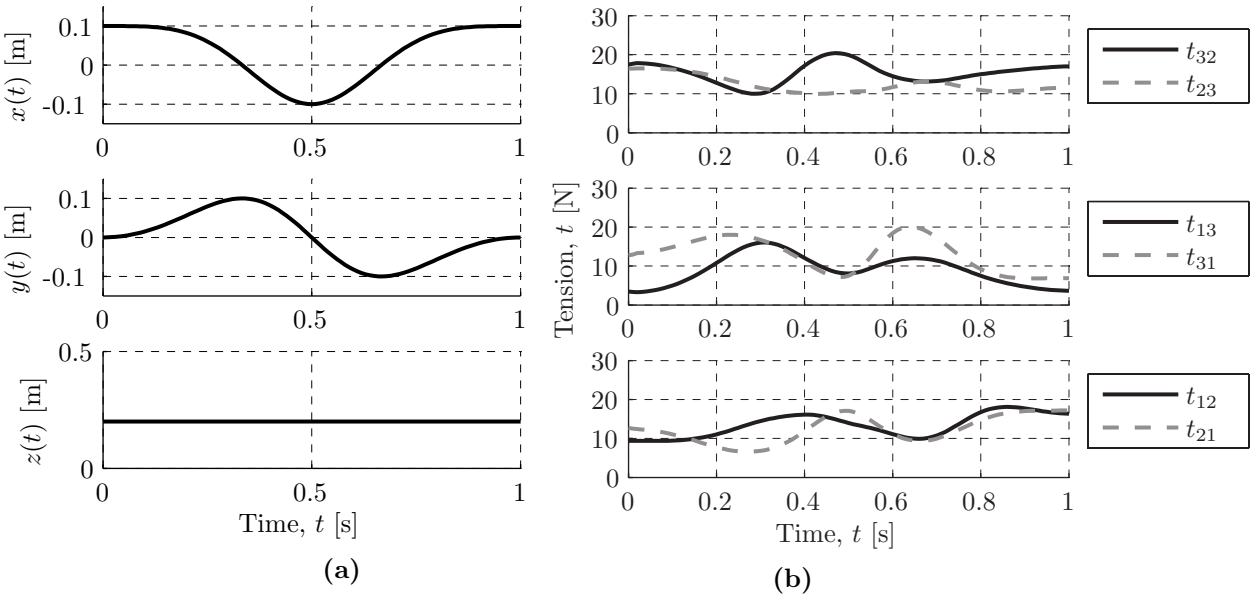

Figure 5.3: A horizontal, circular trajectory (a) and the calculated cable tensions (b) required to generate it.

variables:

$$a(t) = 0.1R + R\left[1 - \cos\left(4\pi\frac{t}{T}\right)\right] \tag{5.26}$$

$$b(t) = 5\pi\left[1 - \cos\left(\pi\frac{t}{T}\right)\right] \tag{5.27}$$

such that the end-effector path is:

$$\begin{aligned} x(t) &= a(t)\cos(b(t)), \\ y(t) &= a(t)\sin(b(t)), \\ z(t) &= z_0 + \frac{H}{2}\left[1 - \cos\left(2\pi\frac{t}{T}\right)\right] \end{aligned} \tag{5.28}$$

The trajectory begins at rest on the Z axis. The end-effector then follows a helix with variable radius that increases with height until the maximum height is reached. The trajectory then retraces itself back to the initial position. Simulation results for the case of $R = 0.1$ m, $T = 10$ s, and $z_0 = 0.1$ m, are shown in Figure 5.4.

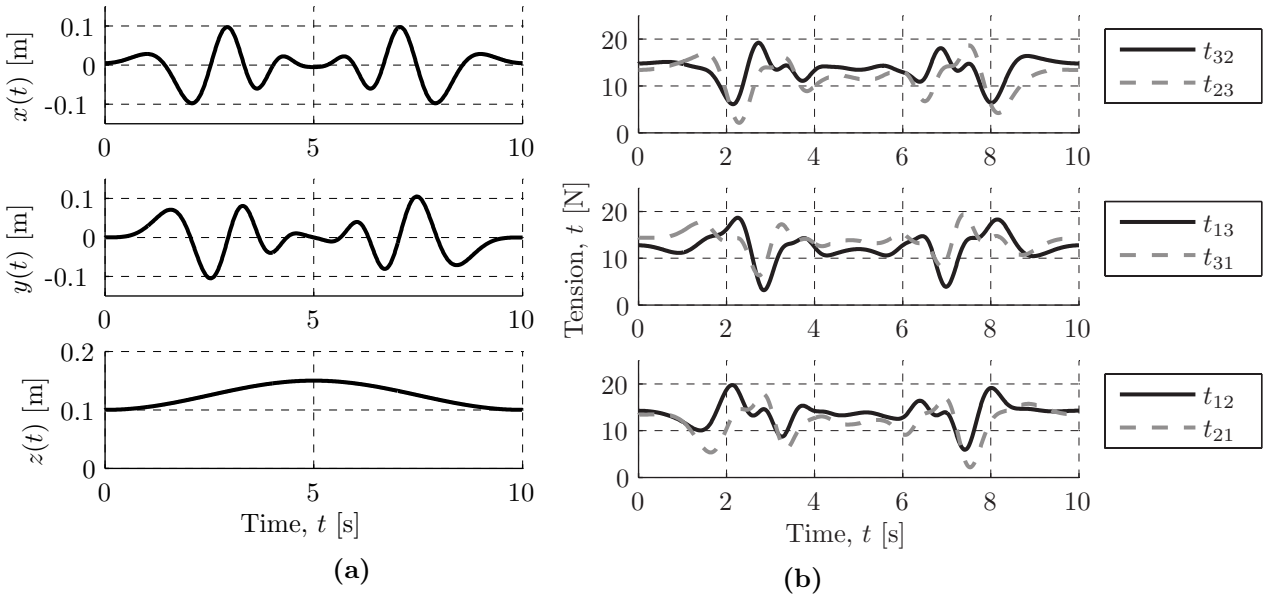

Figure 5.4: A three dimensional helical trajectory (a) and the calculated cable tensions (b) required to generate it.

5.2.1 Acceleration Limits

To test the linear acceleration capabilities of the mechanism, the following rectilinear trajectory is defined:

$$s(t) = \frac{L}{2}\left[1 - \cos\left(2\pi\frac{t}{T}\right)\right] \tag{5.29}$$

where L is the peak-to-peak amplitude of the motion and $s(t)$ describes a motion that can be applied in any desired direction. The second time derivative of Equation 5.29 gives the acceleration of this trajectory as:

$$\ddot{s}(t) = \frac{2\pi^2 L}{T^2}\cos\left(2\pi\frac{t}{T}\right) \tag{5.30}$$

It can be seen that the acceleration will be maximized whenever the cosine term is equal to ± 1, which occurs at the beginning ($t = 0$), middle ($t = T/2$), and end ($t = T$) of the motion. The maximum magnitude of the acceleration at these times is therefore:

$$\ddot{s}_{\max} = \frac{2\pi^2 L}{T^2} \tag{5.31}$$

Simulations of the rectilinear trajectory were repeated for increasing speeds (i.e., decreasing period of motion) until the minimum cable tension became negative. The acceleration calculated from the fastest valid trajectory is then considered representative of the maximum possible acceleration. Equation 5.29 was used to create two trajectories, one in the x and the other in the y direction, with $L = 0.15$ m and $z_0 = 0.35$ m. The results are shown in Figure 5.5 and Figure 5.6. The discontinuities observed in some of the minimum tension plots is due to a changeover between which cable is experiencing the lowest cable tension at that point of the trajectory.

The displayed results have been normalized by their periods, which are marked in-line. From the plots it is found that the minimum tension is lost in the x direction at $T \approx 0.57$ s and at $T \approx 0.52$ s in the y direction. Using Equation 5.31 the maximum accelerations are calculated to be 9.11 $\mathrm{m \cdot s^{-2}}$ and 10.95 $\mathrm{m \cdot s^{-2}}$ in the x and y directions respectively. It should be noted that trajectories starting at different initial positions will not necessarily achieve the same accelerations. The initial value of the static component of the cable tensions varies through the workspace, as shown in Chapter 4. However, it was also shown that the static cable tensions are generally higher toward the z axis and therefore the trajectories used here will generate some of the highest accelerations the mechanism is capable of.

5.3 Discussion

In the results gathered from all of the example trajectories, the cable pairs do not share the same tension. This is for the same reason that the static tensions vary within cable pairs: the offset mass of the spring linkages. Depending on the assembly mode, the inertia of the spring linkages during motion will generate a net moment about the end-effector, which must be resisted by the cable tensions.

The direction of the motion also affects the cable tensions. Since the cables are unidirectional force elements, the only way they can generate acceleration of the end-effector away from the base is by rapidly reducing their tension. This explains the decrease in the minimum cable tension at peak acceleration during the increasingly fast trajectories shown in Figures 5.5 and 5.6. The inertial effects on the cable tension eventually have a greater influence than the tension that resists the spring leg forces. During high rates of deceleration the opposite is true. Cable tensions tend to be higher while the end-effector is decelerating, i.e., accelerating toward the base, since they must resist the change in the momentum of the mechanism's components.

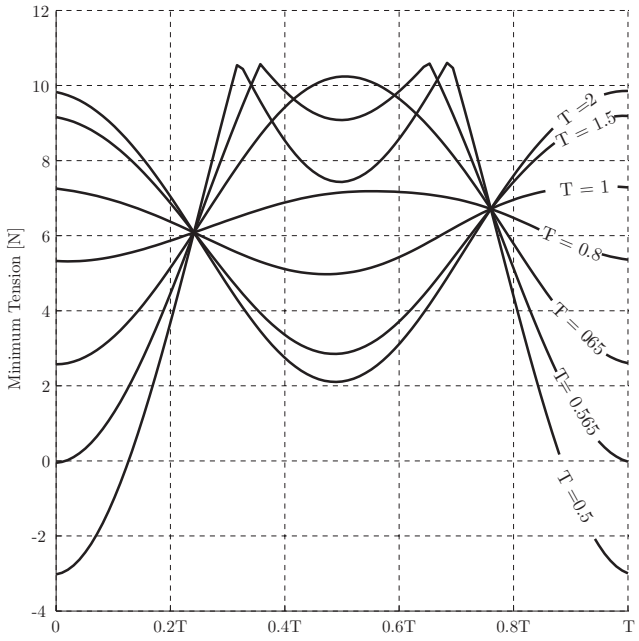

Figure 5.5: Computed minimum cable tensions for reciprocating linear trajectories in the x-direction of increasing speed.

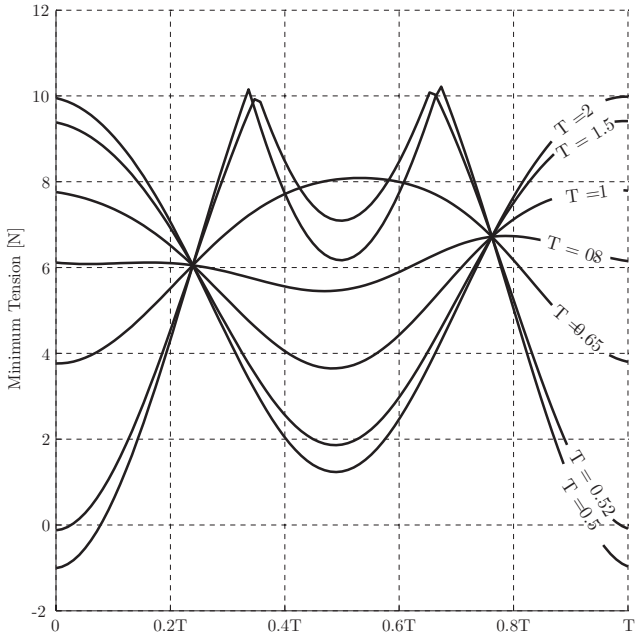

Figure 5.6: Computed minimum cable tensions for reciprocating linear trajectories in the y-direction of increasing speed.

The model used could have been derived using the cable lengths as the generalized coordinates of the Lagrangian equations. The trajectories would be provided in terms of cable lengths and the cable tensions would directly correspond to the generalized forces, without the need for a conversion using the wrench matrix $\mathbf{W}$. However, it was much simpler to derive the energy terms using Cartesian coordinates. The model can still be converted from its current form by using the Jacobian matrix of the mechanism to transform it into the joint space. This presents an issue though, since the lengths of the cables are not independent coordinates because they are actuated in pairs. The winches that actuate the cables cannot control their individual tensions but instead can only resist the torque generated by the sum of their tensions, i.e., $\tau_i \propto (t_{ij} + t_{ji})$.

This thesis is only interested in a fully defined and controllable mechanism. If the mechanism were actuated using only three generalized forces, i.e., the winch torques, the system would actually be underactuated (three torques can't independently control six coupled tensions). There is no direct feedback of the end-effector position or orientation, so it is undesirable to allow any cable tension to be lost. Should the mechanism lose tension, there would be no way to know the state to which it would recover or return. Furthermore, the translational behaviour of the end-effector could not be guaranteed. The cables must therefore be length actuated so that the dynamics are sufficiently constrained.

There is no need for a solution to the forward dynamics of the mechanism if the winches are position controlled. On the other hand, the inverse dynamics could be used to improve the performance of the winch motor controller. Given the model, a known trajectory can be used to anticipate the inertia of the system and its influence on the cable tensions. The sum of the cable tensions can be considered a disturbance force that can be compensated for and rejected by the winch controllers. This would lead to greater positional accuracy of the cable lengths.

6 Physical Implementation and Prototyping

This chapter describes the process of designing a fully functional robot from the proposed tensegrity architecture. There are several motivations behind fabricating a physical prototype. The prototype will act as a proof-of-concept for both the reinforced triangular prism mechanism and tensegrity-based robots in general. Few examples of constructed tensegrity robots exist in the reviewed literature and the author is not aware of any current real-world applications of this class of mechanism. As such, the prototype is a novel development in the field of robotics and will also prove useful in the future for experimental purposes.

The primary objective during construction was to design the mechanical components of the robot in such a way that they replicate the theoretical architecture as closely as possible. Remaining faithful to the simplified mechanism representation ensures that the analysis presented earlier in this thesis remains applicable to the final robot. Likewise, designing the actuation system to use the minimum number of motorized winches, i.e., three, will ensure cable pairs are constrained to be equal in length, a crucial assumption used in the theoretical developments. The robot was also designed with simplicity in mind to reduce the manufacturing costs.

The remainder of this chapter will identify the specific issues with physically implementing this architecture, and more general problems with constructing tensegrity robots. The solutions to some of the design challenges are described in detail and design choices are explained. The actuation, control and calibration systems of the prototype are developed and the mechanism performance is discussed. Recommendations are made regarding the future use and possible improvement of the developed prototype.

6.1 Issues with Physical Implementation

By definition, tensegrity structures, and the mechanisms that are derived from them, must be pin-jointed. These joints will generally have multiple components connected to them. This causes the most difficulty when implementing a tensegrity-based robot; consideration of the physical space occupied by the struts and joints is critical. Connecting multiple rigid bodies at the same point while maintaining full rotational freedom and supporting reaction forces is problematic, and increases the opportunity for mechanical interferences to occur.

Interference between components of the tensegrity mechanism can also occur away from the joints. As already discussed in Chapter 2, the compressive struts of the reinforced triangular prism tensegrity will inherently intersect with one another. The torsion spring linkage introduced in Section 2.3.3 solved this. Alternatively, a split spring design such as the one shown in Figure 6.1 could also be used to eliminate interferences. Gas springs, like those used by Behzadipour et al. [83], could provide a much higher prestress but the greater number of components may reduce the reachable workspace of the mechanism enough to negate any increase to the static workspace. An optimization could be run to reach a balance between mechanical interference and static workspace for the split spring design, but this is outside the scope of this thesis.

Another issue of the pin-jointed architecture is that the actuated cables must also connect to the same nodes as the compressive components. Furthermore, the cables must be routed through some of these joints, since it is not practical for their lengths to be driven by winches within the joints or along the cables themselves. The cables must instead be routed to remotely located winches.

Each cable pair needs to be actuated by the same winch to keep the cable lengths equal. It is desirable to maintain a stationary reel-in point so that there is a linear relationship between the winch motor angle and the change in cable length. This will assist with the development of a control algorithm and simplify solving the inverse kinematics of the mechanism. The cables must be wound on a drum, preferably using level winding to avoid overlapping or tangling, which will help to maintain the previously mentioned linear relationship and reduce wear of the cables. The winches will need to be driven by motors with adequate torque output and some form of feedback, e.g., rotary encoding, will be required for control.

Maintaining cable tension and sufficient prestress is essential to the performance of the physical mechanism. The chosen torsion springs must provide

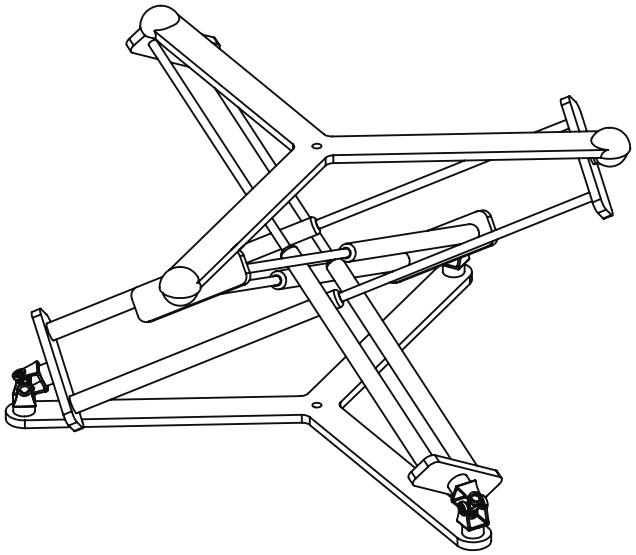

Figure 6.1: The split spring design, an alternative method of applying prestress to the mechanism using gas springs.

the largest torque possible over as large an operating range as possible. However, there is an upper limit to the size, and therefore mass, of the torsion spring before its weight begins to counter any increase in prestress. Finally, friction will be present throughout the system, e.g., the joint bearing resistance, cable contact, or within the winches. This will have a negative impact on cable tensions and must be minimized.

6.2 Design Overview

The fully assembled prototype is pictured in Figure 6.2. A support frame was built so that the mechanism could hang and the weight of most of its components contribute positively to the cable tensions. All stationary components are mounted to a plywood sheet, which acts as the mechanism's base. The design consists of four sub-assemblies: the end-effector, spring linkages, routing pulleys, and winches.

The end-effector is an aluminum plate with three square tubes arranged at 120° from each other. The distal joints of the spring linkages are attached to the ends of the tubes such that their centres are a distance $r_b = 203.4$ mm (8.0 inch) from the centre of the end-effector. The spring linkages are joined to the end-effector on one end and attached to the base at the other end via joints that are

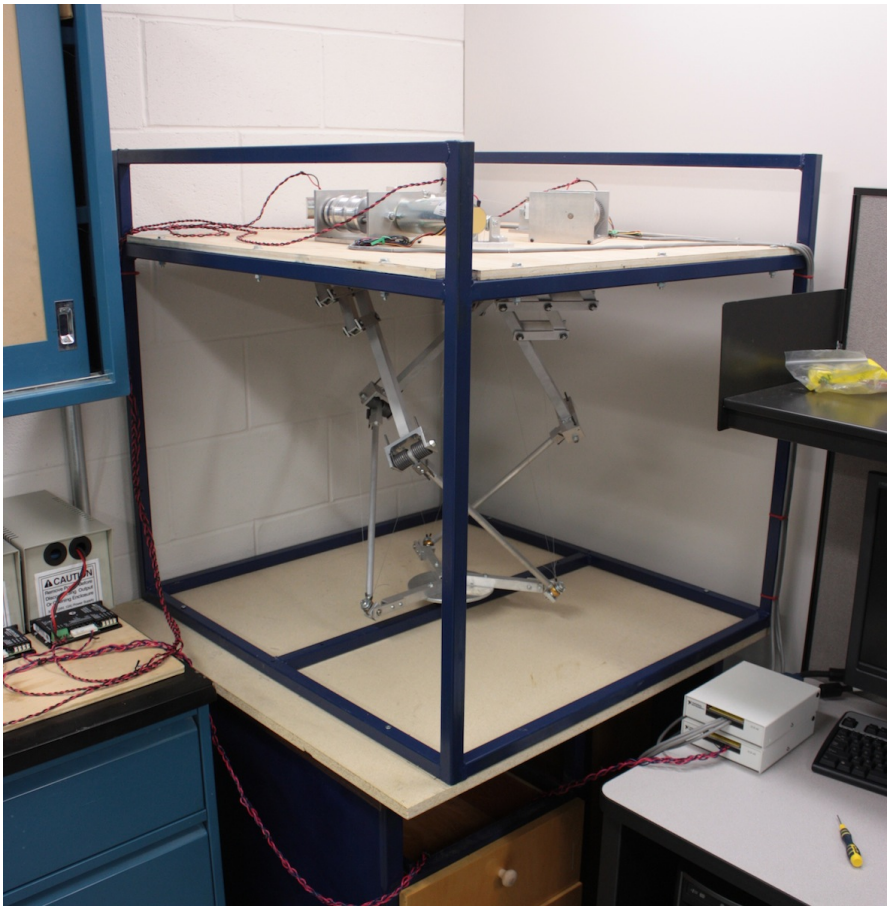

Figure 6.2: Photograph of the constructed prototype.

effectively universal. When fully extended, the spring linkages have a length of $l_0 = 863.6$ mm (34.0 inch). Small diameter steel cables are also attached to the end-effector and are routed through the base to the opposite side where the winches are mounted. The cables pass over pulleys before being wound on the winch drums.

The spring linkage and cable winch assemblies are the more complex parts of the prototype and as such the thought process behind their design is elaborated further in the following two sections. Most physical parameters of the prototype (e.g., masses and component dimensions) have already been listed in Table 4.1.

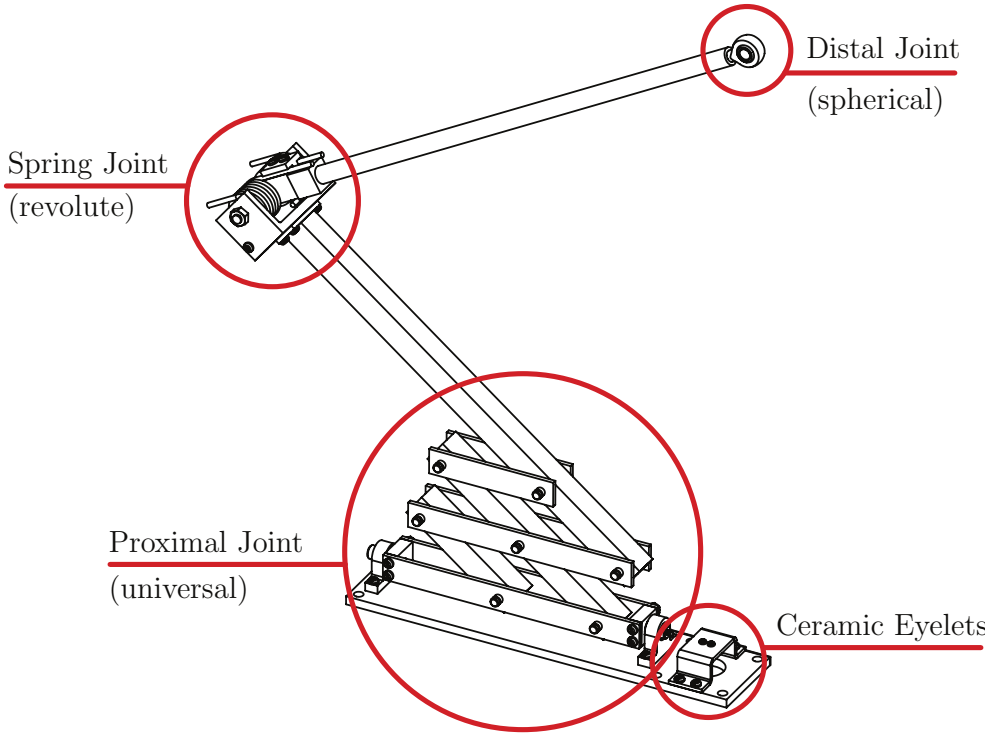

Figure 6.3: CAD drawing of the spring linkage, highlighting its primary components.

6.2.1 Spring Linkage

While functionally identical to the simplified model in Section 2.3.3, the spring linkage shown in Figure 6.3 may not appear to be familiar at first sight. As highlighted, the linkage still has a spherical-revolute-universal joint configuration; the joints are simply implemented in slightly unconventional ways. The reasoning behind this was to allow the cables to pass through the centres of each joint.

The distal end of the linkage must attach to the end-effector via a spherical joint. Each spherical joint must let two cables terminate at the centre of rotation, while still allowing the distal link three rotational degrees of freedom. A secondary goal of the joint design was to maximize its range of motion, so that it does not limit the mechanism workspace significantly. It was assumed that the flexibility of the cables was sufficient to provide them with their required degrees of freedom, and no concentric mechanical joints were needed.

The joint was implemented using a threaded rod end (i.e., ball and socket

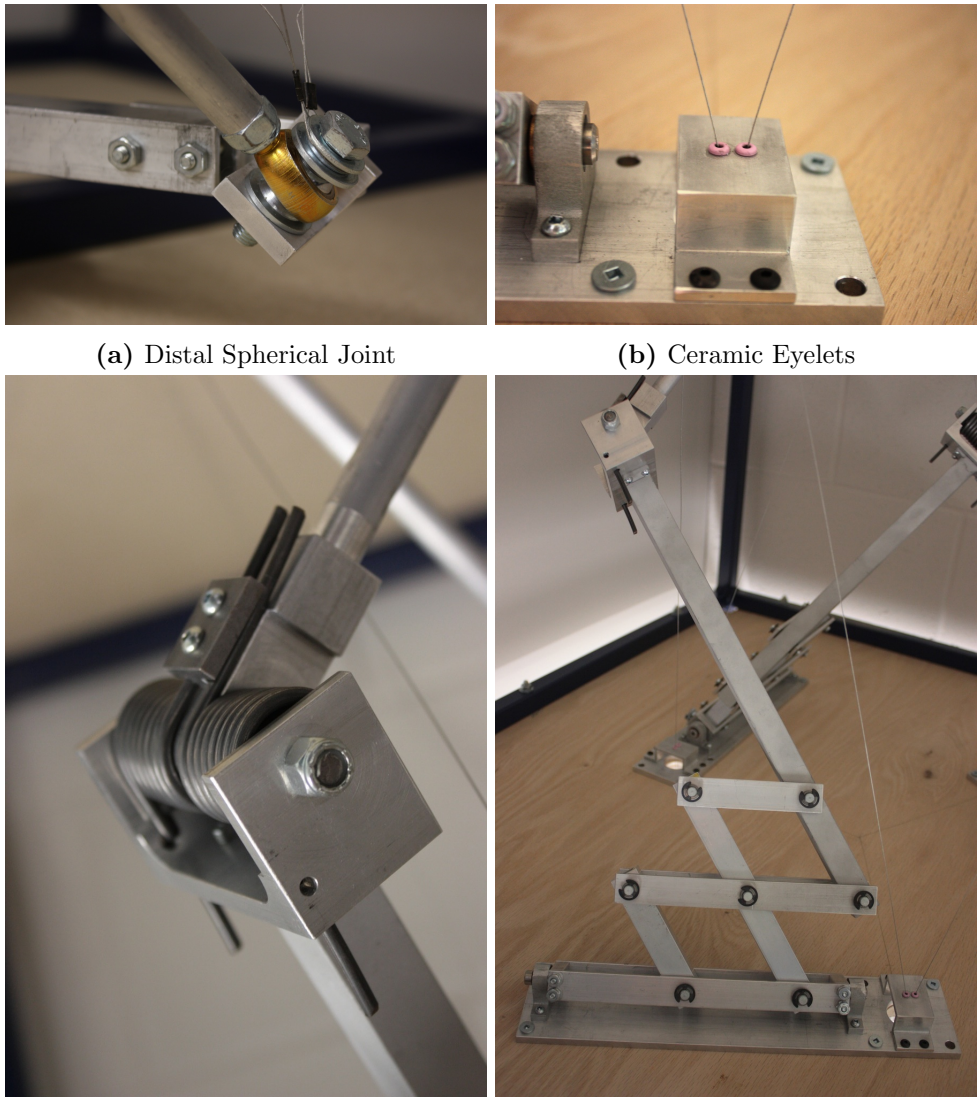

(a) Distal Spherical Joint

(b) Ceramic Eyelets

(c) Torsion Spring Joint

(d) Pantograph Linkage

Figure 6.4: Photographs of the torsion spring linkage components.

joint), as shown in Figure 6.4a. Using crimps, the cables were tied to the bolt that holds the ball of the rod end to the end-effector. While the cable termination points were not at the exact centre of the joint, the slight deviation is considered negligible with regards to the scale of the prototype.

Further down the spring linkage is the torsion spring joint. This must

be a passive revolute joint with torsion springs that apply a torque between the distal and proximal links. As with the rest of the linkage joints, range of motion is very important to consider so the mechanism workspace is not restricted. The spring joint must also be able to resist moments outside of the plane formed by the proximal and distal linkages (i.e., aside from that applied by the torsion springs) while maintaining a minimal weight and volume.

The chosen design, shown in Figure 6.4c, consists of a bracket mounted to the proximal link and a second connector that is attached to the distal link. The distal connector rotates freely about a shaft that spans across the proximal bracket. The connector is located at the midpoint of the shaft and is restricted from sliding along the shaft's axis by c-clips. Two torsion springs are placed symmetrically over the shaft, with one on each side of the distal connector. The legs of the torsion springs are held to the bracket and connector so that any rotational displacement of the joint results in spring deflection, and therefore a generated torque.

The torsion springs used in the revolute joint are also critical to the overall design of the prototype. It is desirable to maximize the stiffness of the springs used to increase the prestress in the mechanism. This optimization will be constrained by the weight of the spring, as well as manufacturing limitations. The standard material used by spring manufacturers is ASTM A288 music wire, which is a high tension steel that is only available in certain standard wire diameters. With some assistance from the manufacturer, a custom spring was designed to meet the requirements of the project. The final manufactured springs are described in Figure 6.5.

Using the values shown in the Table 6.1, the rotational stiffness is calculated to be:

$$\kappa = \frac{Ed^4}{10.8N(D-d)} = 14.95 \text{ N} \cdot \text{m/turn} = 2.38 \text{ N} \cdot \text{m} \cdot \text{rad}^{-1} \tag{6.1}$$

and may be considered linear over the operational range of the springs. This operating range is between 0-130° of deflection, where the stress within the springs will not exceed the material yield strength.

The final component is a base node joint to provide the spring linkage with two rotational degrees of freedom, as defined in Section 2.3.3. Typically, a standard off-the-shelf universal joint could be used to satisfy the mobility requirements of this component. However, in this particular case, challenges arise from the need to have the spring linkage and two cables meet at the joint's centre of rotation. The problem is not unique to the tensegrity architecture but some available solutions, such as using multiple concentric joints [84, 85], would be difficult to adapt so that the cables can still be actuated.

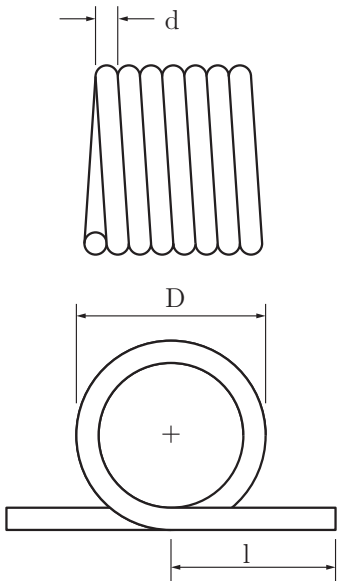

Figure 6.5: Schematic of the custom torsion springs.

Parameter	Value
Max Deflection	180°
Coil Diameter (D)	28.78 mm (1.133 inch)
Wire Diameter (d)	3.43 mm (0.135 inch)
Leg Length (l)	50.8 mm (2.0 inch)
Number of Coils (N)	7
Material	ASTM A288 Music Wire
Elastic Modulus (E)	207 GPa (30×10^6 lbf$\cdot$inch^{-2})

Table 6.1: Parameters of the custom designed torsion springs.

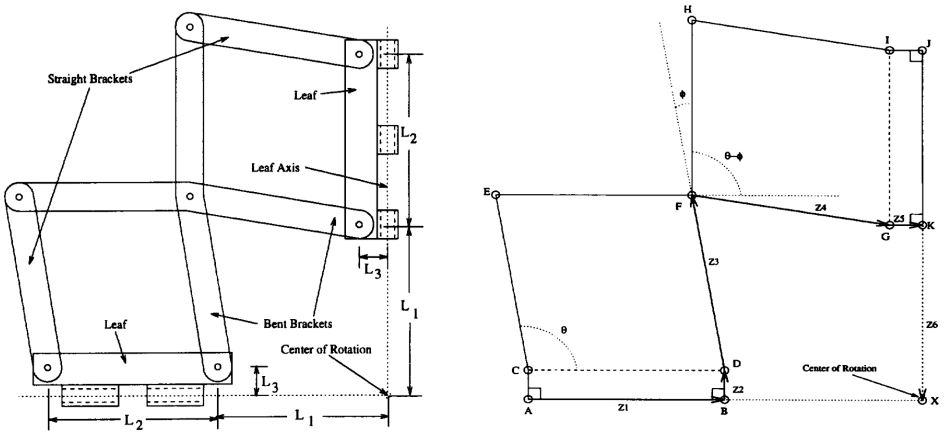

Figure 6.6: The concentric multi-link spherical joint design. Image adapted from Hamlin et al. [86].

One existing approach that would work is Hamlin et al.'s concentric multi-link spherical joint [86], shown in Figure 6.6. This is a modified pantograph linkage designed to constrain its two outer-most links (labelled as "leafs" in the diagram) to rotate about a remote centre of rotation, i.e., one that is not actually located on the links. The other two rotational axes of the joint are hinges attached to the two leafs, only one of which is required for the current application. The links are curved to compensate for the offset of these hinges, allowing all axes of rotation to intersect at the same point, thus creating a spherical joint.

The linkage was altered slightly for use in the tensegrity prototype. As shown in Figure 6.4d, all of the links are straight. In this implementation there is no offset between the centre-line of the lower leaf and its axis of rotation (i.e., $L_3 = 0$ in Figure 6.6), so there is no need for curved links. Each pivot within the linkage is created using a metal dowel and nylon bushing. While this does increase the mass of the overall spring linkage, the majority of the mass is closer to the base of the mechanism. Additionally, the desire to stay true to the theoretical mechanism architecture and allow the cables to pass directly through the base nodes was deemed more important than minimizing the mass of components. Ceramic eyelets are mounted at the effective centre of rotation and allow the cables to pass from the mechanism-side of the base to the winch-side.

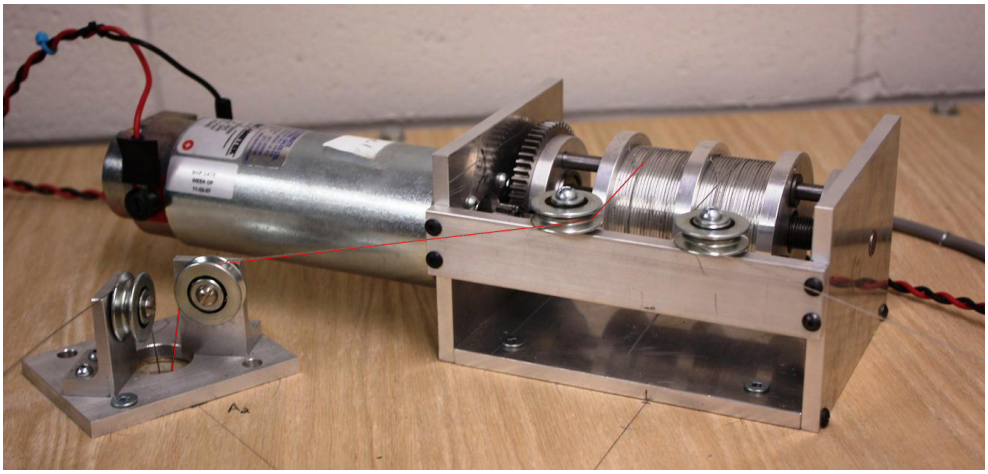

Figure 6.7: Photograph of the translating winch assembly.

6.2.2 Cable Winch

The cable winches were designed to enforce a linear relationship between the change in motor angle, $\Delta\theta$, and the change in cable length, $\Delta\rho$. Winches typically do not have a fixed cable reel-in point or level winding, both of which cause non-linearities. In the case of the tensegrity prototype, this means the length of cable between the winches and the base nodes (i.e., ceramic eyelets) would vary depending on how much cable has been wound up. Eliminating these non-linearities with intelligent hardware design would simplify the inverse kinematics of the prototype. Each winch must also actuate two cables at the same time.

The chosen design, shown in Figure 6.7, is similar to several existing winches [75, 87, 88] used to actuate CDPMs. Each cable passes over a pulley and is wound on the winch drum at a constant reel-in point. The drum is driven by a servomotor via a spindle, i.e., the three smooth shafts in Figure 6.7. The drum remains free to translate along the spindle shafts on oil-impregnated bronze bushings. The drum also rotates around a fixed threaded shaft. As such, when the spindle causes the drum to rotate, the drum translates at a rate equal to the shaft thread pitch of 0.787 thread/mm (20 thread/inch). The grooves on the drum have a matching thread so that both cables are level wound, enforcing $\Delta\theta \propto \Delta\rho$.

The motors were already available, so were not selected specifically for this application. A 3.5:1 gear ratio is used to magnify the output torque of the motors, resulting in a maximum continuous torque of approximately

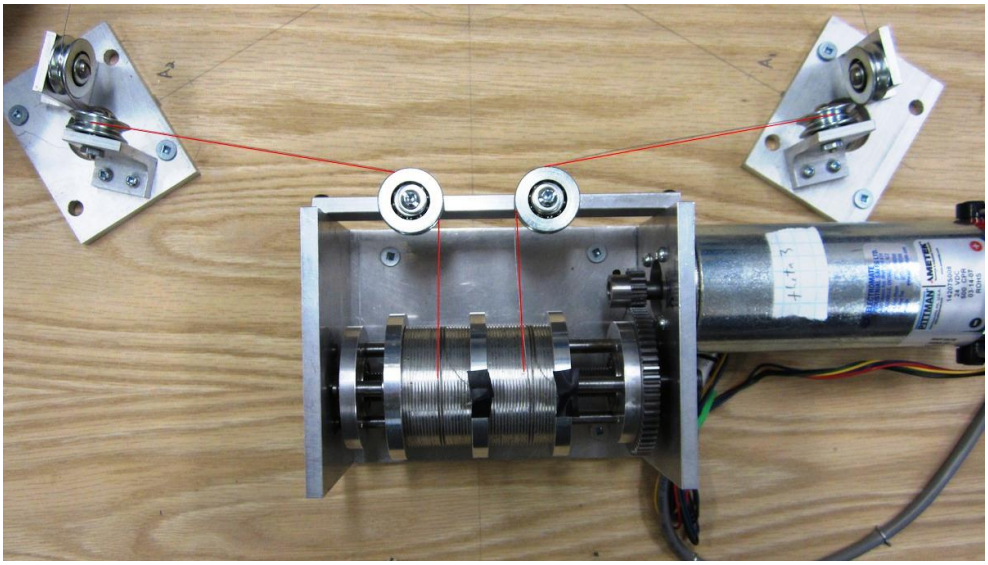

Figure 6.8: Photograph of the winch-side of the base, with one cable pair highlighted to illustrate how cables are routed.

1.48 N · m (13.1 lbf · inch) and a peak output of 2.97 N · m (26.3 lbf · inch), when considering the current limitations of the motor driver circuit. The winch drum radius is 25.4 mm (1.0 inch) so the total tension that each winch can exert on its cable pair is approximately 30 N (6.74 lbf) during continuous operation and 60 N (13.49 lbf) for brief durations.

Steel cables of diameter 0.397 mm (1/64 inch) were chosen, with a breaking strength of 222.4 N (50 lbf). The cables had a 7x7 strand construction, which makes them more flexible than single strand cables. Each cable passes over two pulleys, as shown in Figure 6.8; one pulley is on the winch and one is on the opposite side of the base from the ceramic eyelets. The pulleys are mounted on ball bearings to reduce frictional losses that would reduce cable tension. On the mechanism side of the base, the cables pass through the ceramic eyelets, shown in Figure 6.4b. The material was chosen for its hardness so that the steel cables could not cut them. A slight offset exists between the actual node locations and the locations of the eyelets, but on the scale of the prototype the distance is considered negligible.

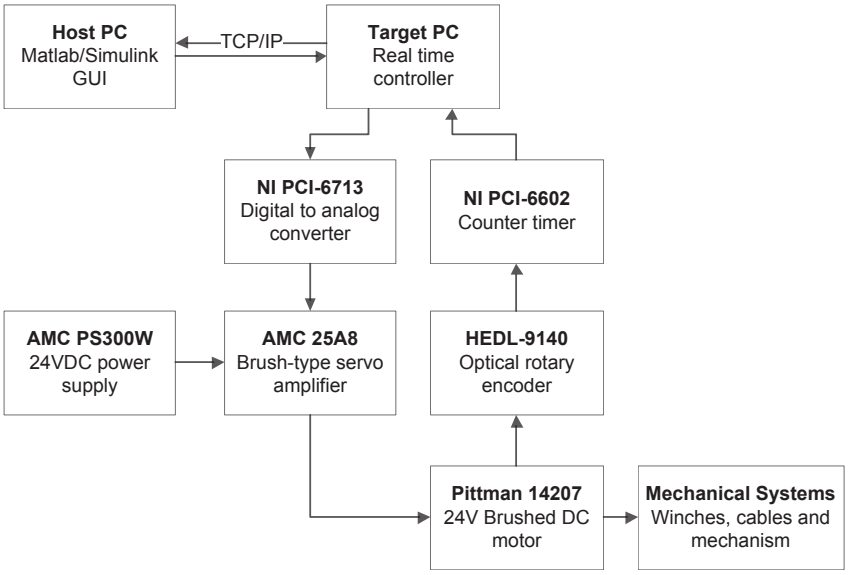

Figure 6.9: Hardware used to implement the prototype controller.

6.3 Control and Calibration

The control hardware configuration is shown in Figure 6.9. The position of the end-effector is controlled by directly actuating the length of the three cable pairs via winches. Each winch assembly is driven by a Pittman 14207 brushed 24 VDC servomotor and fitted with a 4000 count-per-revolution incremental encoder for position feedback. Power to the motors is supplied by Advanced Motion Controls (AMC) 25A8 brushed type servo amplifiers that are controlled by a PC DAC card. MATLAB xPC Target software was used to program the controller and, as shown in Figure 6.9, two computers are used in this setup: the host PC and the target PC.

The target PC runs a real time operating system, which performs data acquisition, executes control calculations, and generates command output while guaranteeing a minimum execution frequency. A National Instruments (NI) PCI-6602 counter timer card provides feedback of the motor angles by decoding the signal received from the incremental encoders. A NI PCI-6713 digital-to-analog converter outputs a ± 5 VDC signal that is used to command

the amplifier gains. Each amplifier supplies its respective motor with a 24 VDC pulse-width-modulated (PWM) signal. The output duty cycle of the PWM signal is proportional to the input to the amplifier by a gain that is set manually by a potentiometer. The host PC runs MATLAB/Simulink and provides a user interface to the controller. While the control algorithm shown in Figure 6.10 is uploaded and executed on the target PC, the host PC remains connected and allows parameters, e.g., controller gains, to be modified on the fly.

Two control modes are made available: set point control, which moves the end-effector to a specified position $\mathbf{p}$, and trajectory control, which follows pre-generated position trajectories, $\mathbf{p}(t)$. Both modes supply the controller with Cartesian coordinates of the robot end-effector. These coordinates are then converted into the required cable lengths, $\boldsymbol{\rho}_t(t)$, using the analytical inverse kinematic solution from Chapter 3, which assumes only translational motion of the end-effector.

Conversion from cable lengths to motor commands presents some minor complications. Due to the use of relative encoders (as opposed to absolute) the control system must be provided with the initial cable lengths, $\boldsymbol{\rho}_0$ of the end-effector after each system reboot. Therefore the controller is really only controlling the change in cable lengths, not the actual length of the cables. Once the relative change in cable length is calculated the motor angles, $\boldsymbol{\theta}(t)$ are found by diving by the radius of the winch drum, r_w and multiplying by the winch gear ratio G_r. The commanded motor angles are then fed into a PID controller with negative feedback of the measured motor angles, $\boldsymbol{\theta}_m(t)$.

A homing device was designed, as shown in Figure 6.11, to hold the mechanism in a known configuration while the controller is started. The base part has three dowels protruding from it and is mounted at a known point on the prototype's support frame. A second part, with three holes of the same size and spacing as the three dowels, is attached to the end-effector. When the two parts of the device mate, the prototype's spring linkages apply enough force to hold the mechanism position and orientation constant. The only accommodation that must be made for this solution is that all commanded trajectories must begin by travelling vertically to disengage the homing device. The initial cable lengths in the home pose must be subtracted from those calculated using the IKP to acquire the relative cable length changes.

The controller was first developed in MATLAB Simulink strictly as a position controller for a model of one of the winches. The winch model was based on the ideal model of a DC brushed motor and included the inertia of the shaft, gears, and drum. Initial PID gains were calculated automatically using the MATLAB/Simulink Control System Toolbox. When applied to a physi-

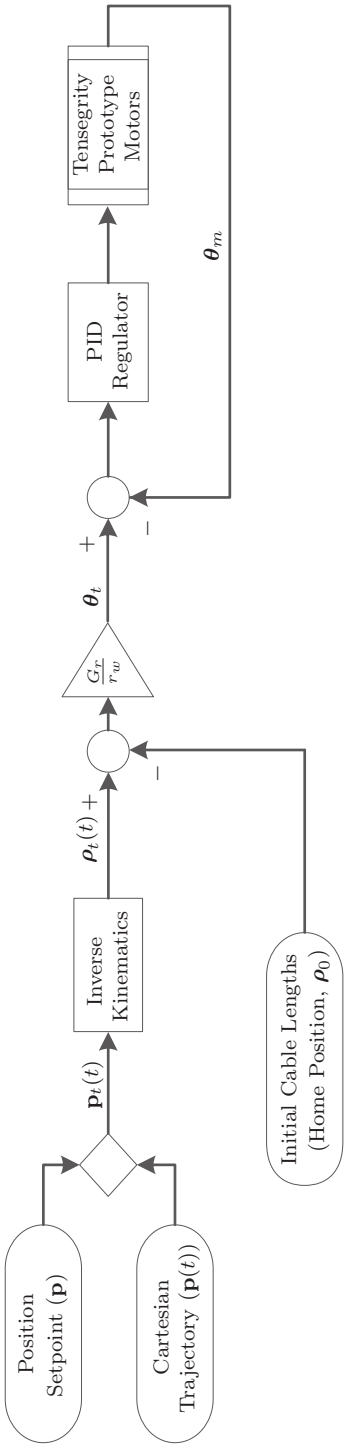

Figure 6.10: Flow diagram of the controller designed for the prototype.

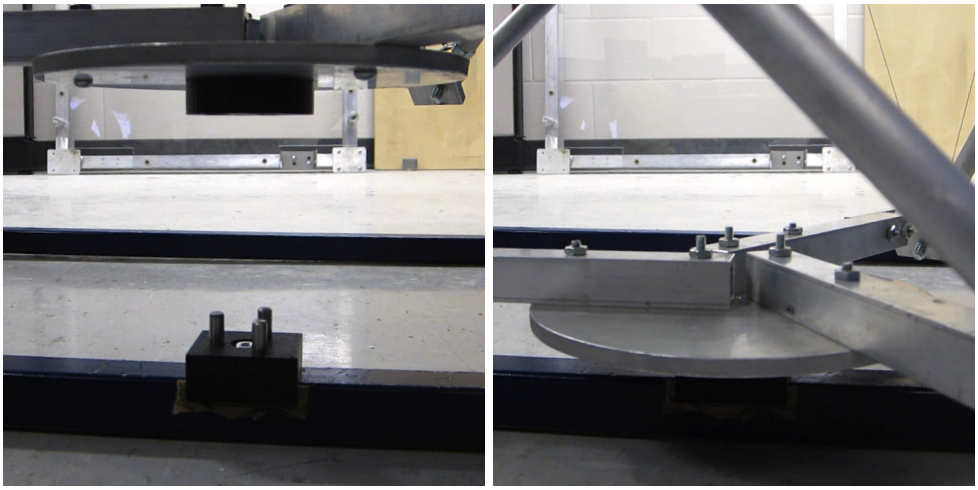

Figure 6.11: Homing device used to hold the tensegrity prototype in an initial configuration.

cal winch with no load attached, the controller performed poorly, presumably due to modelling inaccuracies. Better results were achieved by manually tuning the controller gains using the Ziegler-Nichols [89] tuning method. The derived gains were then applied to all three winches without observing any performance issues.

6.4 Discussion and Recommendations

Preliminary observations made while operating the tensegrity prototype were encouraging. Most importantly, the end-effector was visually confirmed to remain in translation. Additionally, paths that were theoretically valid were followed without any unexpected loss of cable tension. There did not appear to be any serious issues with respect to positional accuracy or vibrations. This can be observed in Figure 6.12, where several LEDs attached to the end-effector trace the relatively smooth path of a trajectory during a long exposure photo. However, these demonstration trajectories did not attempt to push the theoretical acceleration limits, for both the mechanism and the author's own safety.

The theoretical workspace boundaries were explored by slowly moving the mechanism's end-effector into positions where interferences or loss of tension should occur. The boundaries were found to be approximately correct, with any deviation likely due only to small modelling inaccuracies. It was interest-

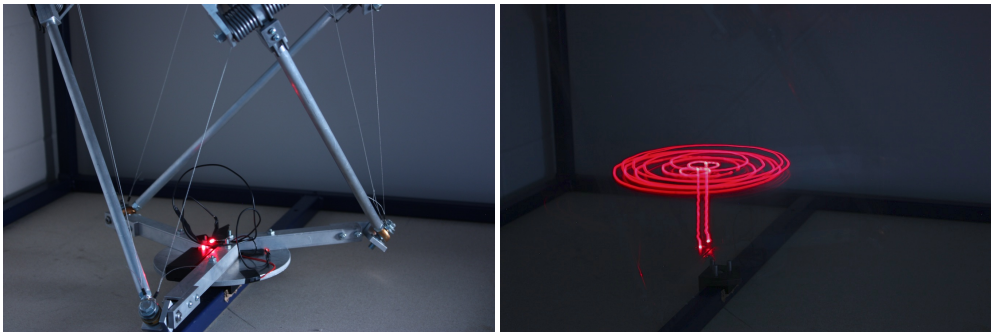

(a) Stationary **(b)** Moving

Figure 6.12: An example end-effector trajectory that has been traced using LEDs and long exposure photography.

ing to observe that the mechanism did not collapse when a single cable lost tension. Cable failure was not investigated within this thesis but the possibility of the mechanism being able to sustain the loss of tension in one cable is a promising result.

There were some notable issues, mostly related to cable friction. While not entirely unexpected, there was significant noise generated by the contact between the steel cables and the ceramic eyelets used to route them through the base of the prototype. This contact friction would presumably lead to cable abrasion and have a detrimental effect on the useful lifetime of the cables. From a strength-of-materials standpoint, the cables were designed to safely withstand the maximum loads that can be exerted by the DC motors, but fatiguing would certainly reduce this safety factor.

To reduce cable wear, the ceramic eyelets could be replaced by lubricated cable sheaths, such as those used to route dérailleur and brake cables on bicycles. Different cable coatings may also reduce friction and alternative wire rope constructions could improve resistance to wear and tear. The cables could also pass over rotating pulleys or bearings, instead of sliding over a stationary surface. For example, Figure 6.13a shows a swivelling pulley that could redirect a single cable. Another example is a bearing design proposed by Billette [90] and shown in Figure 6.13b. Unfortunately, these alternatives require more space than is available in the mechanism joints and would be difficult or impossible to place. Additionally, the solution shown in Figure 6.13a would not have a constant takeoff point for the cable, which was a major design consideration of the current prototype.

Other observed issues had more to do with design choices that are unique

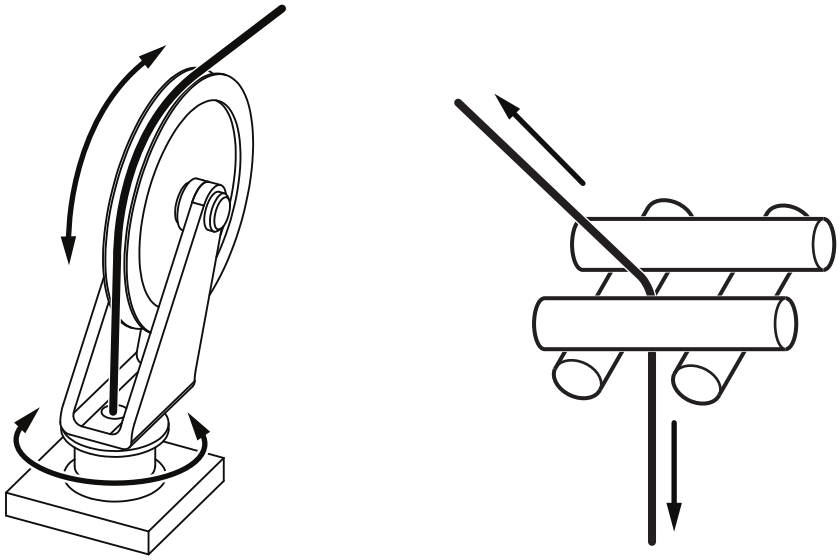

(a) Swivel **(b)** Bearings

Figure 6.13: Possible designs for routing cables through a point to reduce friction.

to this specific robot architecture. For example, the homing feature, described in Section 6.3, works in theory, but in practise small errors in the initial position or orientation of the end-effector may exist. These errors will be carried on throughout operation and are not observable by the controller. Additionally, the process of assembling the mechanism, especially stringing the cables, is awkward. Any error in initial cable lengths will further contribute to ongoing position errors. Finally, there is also a high amount of potential energy contained within the system when in the home configuration because interferences prevent the torsion spring linkages from fully extending. This may be unavoidable with this particular design and raises some safety concerns.

The next step in evaluating the mechanical design is to gather quantitative measurements, rather than relying purely on human observations. While experimental testing was not within the scope of this thesis, there are several ways the robot could be instrumented in the future.

A computer vision system is one possible measurement technique. It could be used to track the movement of the end-effector, calculate positional errors, and give a clearer measure of mechanism accuracy and repeatability. This method would be unobtrusive since vision systems generally only re-

quire small markers to be attached to the tracked object. Similar data could be estimated using an inertial measurement unit (e.g., a 6-axis accelerometer/gyroscope). Orientation data could also be estimated to confirm the translational behaviour of the end-effector.

Cable forces could be measured using load cells, verifying that the cables remain in tension and measuring the losses due to friction. These could be placed in-line with the cables, possibly where they terminate at the end-effector nodes, to directly measure cable tension. Tension could also be measured implicitly by measuring the winch torques. Tension could also be measured indirectly with a method similar to that used by Otis et al. [64] where cables were passed over pulleys. The reaction forces were measured where the pulleys were mounted, which were then used to calculate cable tension.

In summary, the tensegrity prototype was observed to behave in an expected manner. The positive qualitative results increase confidence that the theoretical work of this thesis correctly describe the tensegrity architecture. For further confirmation, quantitative methods must be applied. Future work on the prototype should involve executing one or more of the experimental assessments proposed above.

7 Summary and Conclusions

This thesis investigated the feasibility of applying the structural concept of tensegrity to robotic manipulators. A robotic mechanism based on tensegrity could inherit several benefits from the structure on which it is based. For example, the high strength to weight ratio of tensegrity structures could be beneficial to a derived mechanism's dynamic performance. Examples of tensegrity-based mechanisms have been previously presented in literature but few prototypes of these designs have been constructed. The lack of functional prototypes can often be attributed to complex actuation schemes and the difficulty of physically constructing the proposed designs. As such, the mechanism in this thesis was developed primarily to ensure ease of control, mechanical design, and manufacture.

The mechanism relies on length controlled cable-winch pairs for actuation. This actuation scheme is analogous in many ways to purely cable driven parallel mechanisms, which have received far more attention in recent research literature than tensegrity mechanisms. The similarity with cable driven mechanisms allows some existing analysis tools and methods to be adapted for use in this thesis. These tools are used throughout the thesis to determine the kinematic behaviour of the mechanism, investigate its reachable workspace, and to ensure the mechanism maintains tension in all of its cables under several conditions and loads.

7.1 Contributions of Thesis

The primary contribution of this thesis was to develop a new actuation scheme for a known tensegrity structural architecture to generate a novel 3-DoF translational mechanism. Before choosing an actuation scheme, the prestress requirements of the tensegrity architecture had to be determined. This lead to the knowledge that three of the structure's elements needed to be prestressed, thus the choice of three compressive spring legs was made. The types of joints

used, i.e., universal at the base, revolute at the torsion spring, and spherical at the end-effector, were chosen to supply sufficient mobility to the mechanism's end-effector. Furthermore, other elements of the tensegrity structure were chosen to be rigid in order to create both a base and a rigid end-effector for the mechanism. The orientation of the joint axes were determined by attempting to simplify analysis, limit motion of the rigid links, and to avoid mechanical interference between legs and cables. All of this work eventually lead to the choice of paired actuation of the tensile elements, i.e., cables.

Through the development of this mechanism existing robotic analysis methods were applied to the tensegrity mechanism. An understanding of the kinematics, statics and dynamics was gained via this analysis. These demonstrations could prove useful in any future work that examines the reinforced triangular prism tensegrity mechanism or similar tensegrity mechanisms. Additionally, the constructed prototype can serve as a design example. Its strengths and weaknesses can assist with the mechanical design of future functional tensegrity mechanisms and manipulators.

7.1.1 Chapter Summaries

The chapters within this thesis covered the following topics:

- Chapter 2 introduced the novel actuation and prestress scheme used by the mechanism. Background information on the concept of tensegrity was provided and a structural analysis was performed to confirm that the proposed mechanism remains rigid and still fits the definition of tensegrity.
- Chapter 3 presented analytical expressions for the mechanism position, velocity and acceleration-level kinematics that are valid so long as tension is maintained in all cables. The Jacobians of the mechanism were calculated and used to determine the conditions that lead to kinematic singularities. An efficient method of checking for cable-linkage interferences was developed. Finally, the kinematic workspace of the mechanism was visualized considering actuator limitations, singularities and the avoidance of cable interferences.
- Chapter 4 verified that the cables remain in tension under static and pseudo static cases, for at least a portion of the mechanism's reachable workspace. Static analysis of the mechanism was conducted to calculate the forces within individual cables. Depending on the orientation of the mechanism with respect to gravity, the actuated cable pairs do not have equal tensions. This was found to be due to the mass of the spring linkages, which cause asymmetric loading that is compensated for by the

tension difference. A method of quantifying the magnitude of forces that can be exerted or resisted by the mechanism, while maintaining tension in all cables within finite bounds, was developed. This method was then used to quantify the force exertion capabilities over the workspace and to determine the boundaries of the static workspace.

Additionally, the stiffness matrix of the mechanism was derived using techniques borrowed from cable driven parallel mechanisms. The resulting matrix, calculated numerically for various poses, was verified against other approaches and found to match. A matrix partitioning technique was used to separate translational DoF from rotational and solve the unit non-homogeneity issue of the stiffness matrix. Mappings of minimum and maximum stiffness in several directions, both rotational and Cartesian, were generated and displayed.

- Chapter 5 described the derivation of a dynamic model using the Lagrangian formulation, based on a simplified representation of the mechanism. This model was used to calculate the resultant cable forces for several generated trajectories to check if cable tension is maintained. It is also used to calculate the maximum linear acceleration that can be achieved without losing tension in several trial trajectories.
- Chapter 6 summarizes the obstacles involved in physically implementing the mechanism and presents potential solutions to these challenges. Details of the chosen design and why decisions were made with respect to the design challenges are outlined. A brief description is given of the physical mechanism, its actuation system, and the control hardware. The prototype is reviewed qualitatively and its limitations and flaws are identified. Future improvements with respect to the mechanical design are proposed along with proposed experimental procedures for quantitative evaluation and verification of the analytical work presented in this thesis.

7.2 Recommendations for Future Work

A possible extension of this thesis is further work on control algorithm development. The PID regulation of cable lengths, as applied to the constructed prototype, performs well but ignores the mechanism's dynamics. The dynamics of the system would become non-negligible if the mechanism were commanded to follow a trajectory requiring higher accelerations. To compensate for inertial effects, the dynamic model could be included in the control algorithm. Despite its non-linearity, the dynamic model could be included via feedback linearization.

There are several issues preventing the integration of the dynamic model in the controller. Firstly, there is no direct feedback of cable lengths. Cable lengths are inferred from the angular positions of the winches but calculating their lengths in this way is not valid if the cables become slack. Feedback linearization is also typically used for torque control. Cable tension could be measured in various ways, but in the case of the tensegrity mechanism the cables are driven in pairs. Therefore the tensions are not independent, nor are they necessarily identical. Controlling the mechanism using a reduced set of inputs adds even more complexity.

The dynamic model itself would require further development before being included in the controller. The issue lies with how the distance constraints posed by the cables are not explicitly enforced. The model developed in Chapter 5 assumes it is given a valid translation-only trajectory. This is appropriate if all cables remain in tension, but the moment tension is lost the model becomes invalid. Other methods of deriving the dynamic model of similar tensegrity mechanisms exist [34]. These methods add constraints to the equations of motion. The resulting system of non-linear equations can then be solved numerically at each time step while enforcing the velocity and acceleration level kinematics to provide a constrained simulation. However, solving equations numerically can take a indeterminate amount of time, creating yet another issue to consider when trying to implement a real-time controller.

Further work should also focus on improving the design of the mechanism. In addition to the changes already suggested in Section 6.4, the parameters that define the mechanism, e.g., spring linkage length, could be optimized. This thesis presents several performance indices, such as minimum cable tension, arbitrary force exertion, and stiffness. Each of these can be used to quantify the mechanism's performance throughout its workspace. Depending on the intended application of the mechanism, one or more of these indices could be used as objective functions. Relative weighting of the indices would vary by application, based on how important each is perceived to be. The goal of such an optimization could be, for example, to find parameters that result in a mechanism that maintains a minimum stiffness in a certain direction for every pose within a subsection of its workspace.

Finally, an evaluation of the constructed prototype's performance should be completed. This would require measurement and experimental validation of the indices (i.e., stiffness, force capabilities, etc.) developed in this thesis. If the intended purpose of the mechanism is to be used for pick-and-place tasks then the accuracy, repeatability, speed and workspace are all critical to its performance. After generating experimental data the tensegrity mechanism's performance can be compared to that of established pick-and-place

manipulators such as SCARA type serial manipulators or delta-bot parallel manipulators. This comparison may reveal further improvements that could be made to the design of the mechanism and establish the feasibility of real-world applications of tensegrity mechanisms.

7.3 Conclusion

This thesis has shown that the reinforced triangular prism tensegrity mechanism could potentially be used for real-world applications, such as industrial pick-and-place operations. The simplistic actuation scheme results in 3-DoF translational motions and easily computable solutions to the forward and inverse kinematic problems. The mechanism's reachable workspace is large and well defined, even when factoring in cable-linkage interferences and loss of cable tension. The ratio of the workspace volume to the base footprint is also comparable to some rigid link parallel mechanisms that are already in use. The mechanism's workspace is not obstructed by cables and could be mounted above a work cell, rather than completely surrounding it like most CDPMs must.

However, the mechanism has several drawbacks. The application of prestress to the mechanism is highly dependent on the stiffness of the selected torsion springs. Realistic stiffness values limit both the load capability and dynamic abilities of the mechanism. It is also difficult to scale the torsion spring design, to the point that torsion springs cannot supply sufficient prestress for a mechanism much larger or heavier than the constructed prototype. Additionally, the bending stresses within the torsion spring coils will cause fatiguing and the springs will eventually need to be replaced. Another critical component, the actuated cables, would also require frequent maintenance due to wear from friction and winding.

Despite these limitations there remain many opportunities for further study and optimization of this particular mechanism. Future work may also give rise to better methods of applying prestress, which would solve most of the mechanism's shortcomings. Finally, the adapted methods presented in this thesis, along with the solutions to the issues of physically implementing a tensegrity-based mechanism, could be applied to similar mechanisms in related studies.

Bibliography

[1] L.-W. Tsai, *Robotics: The Mechanics of Serial and Parallel Manipulators*. John Wiley & Sons, 1999.

[2] J. Angeles, *Fundamentals of Robotic Mechanical Systems*. Springer, 2007.

[3] GrabCAD Ltd. Grabcad library. [Online]. Available: http://www.grabcad.com/

[4] D. Corbel, M. Gouttefarde, and O. Company, "Towards 100G with PKM. Is Actuation Redundancy a Good Solution for Pick and Place," in *IEEE Transactions on Robotics and Automation*. Anchorage, Alaska: IEEE, 2010, pp. 4675–4682.

[5] S. Briot and I. A. Bonev, "Pantopteron: A New Fully Decoupled 3DOF Translational Parallel Robot for Pick-and-Place Applications," *Journal of Mechanisms and Robotics*, vol. 1, no. 2, p. 021001, 2009.

[6] S. E. Landsberger, "Design and Construction of a Cable-Controlled Parallel Link Manipulator," M.Sc. Thesis, Massachusetts Institute of Technology, Cambridge, MA, USA, 1984.

[7] J. Albus, R. V. Bostleman, and N. G. Dagalakis, "The NIST Robocrane," *Journal of Robotic Systems*, vol. 10, no. 5, pp. 709–724, 1992.

[8] S. Kawamura, W. Choe, S. Tanaka, and S. R. Pandian, "Development of an Ultrahigh Speed Robot FALCON using Wire Drive System," in *Proceedings of the 1995 IEEE International Conference on Robotics and Automation*, Nagoya, Japan, 1995, pp. 215–220.

[9] L. L. Cone, "Skycam: An aerial robotic camera system," *Byte*, vol. 10, no. 10, pp. 122–132, 1985.

[10] C. Meyer and A. Verl, "Large-scale assembly of solar power plants with parallel cable robots," in *Robotics (ISR), 2010 41st International Symposium on and 2010 6th German Conference on Robotics (ROBOTIK)*, Munich, Germany, 2010.

[11] S. Tadokoro, R. Verhoeven, M. Hiller, and T. Takamori, "A portable parallel manipulator for search and rescue at large-scale urban earthquakes and an identification algorithm for the installation in unstructured environments," in *Proceedings of the 1999 IEEE/RSJ International Conference on Intelligent Robots and Systems*, vol. 2, 1999, pp. 1222–1227.

[12] T. Bruckmann, L. Mikelsons, T. Brandt, M. Hiller, and D. Schramm, *Parallel Manipulators, New Developments.* Springer, 2008, ch. Wire Robots Part I: Kinematics, Analysis & Design.

[13] S. Behzadipour and A. Khajepour, "Design of Reduced DOF Parallel Cable-Based Robots," *Mechanism and Machine Theory*, vol. 39, no. 10, pp. 1051–1065, Oct. 2004.

[14] ——, "A New Cable-Based Parallel Robot with Three Degrees of Freedom," *Multibody System Dynamics*, vol. 13, no. 4, pp. 371–383, May 2005.

[15] S. Behzadipour, "High-Speed Cable-Based Robots with Translational Motion," Ph.D., University of Waterloo, Waterloo, ON, Canada, 2005.

[16] R. B. Fuller, "Tensile-Integrity Structures," Patent 3 063 521, 1962.

[17] R. Motro, *Tensegrity: Structural Systems for the Future.* Butterworth-Heinemann, 2003.

[18] A. S. Wroldsen, "Modelling and control of tensegrity structures," Ph.D., Norwegian University of Science and Technology, Trondheim, Norway, 2007.

[19] V. G. Jáuregui, "Tensegrity structures and their applications," Master's thesis, Queen's University, Belfast, 2004.

[20] K. D. Snelson, "Continuous tension, discontinuous compression structures," Patent US 3 169 611, 1965.

[21] ——. Personal webpage. [Online]. Available: http://www.kennethsnelson.net/

[22] R. E. Skelton and M. C. de Oliveira, *Tensegrity Systems.* Springer, 2009.

[23] A. Pugh, *An Introduction to Tensegrity.* University of California Press, 1976.

[24] I. J. Oppenheim and W. O. Williams, "Tensegrity Prisms as Adaptive Structures," *ASME Adaptive Structures and Material Systems*, vol. 54, pp. 113–120, 1997.

[25] R. E. Skelton and C. Sultan, "Controllable Tensegrity: A New Class of Smart Structures," in *Proceedings of SPIE 3039*, vol. 3039, San Diego, CA, USA, 1997, pp. 166–177.

[26] J. Duffy, J. Rooney, B. F. Knight, and C. D. Crane, "A Review of a Family of Self-Deploying Tensegrity Structures with Elastic Ties," *Shock and Vibration Digest*, vol. 32, no. 2, pp. 100–106, 2000.

[27] B. F. Knight, "Deployable Antenna Kinematics using Tensegrity Structure Design," Ph.D. Thesis, University of Florida, Gainesville, FL, USA, 2000.

[28] B. F. Knight, Y. Zhang, J. Duffy, and C. D. Crane, "On the Line Geometry of a Class of Tensegrity Structures," in *Proceedings of a Symposium Commemorating the Legacy, Works, and Life of Sir Robert Stawell Ball Upon the 100th Anniversary of A Treatise on the Theory of Screws*, University of Cambridge, Trinity College, Cambridge, UK, 2000.

[29] G. Tibert, "Deployable Tensegrity Structures for Space Applications," Ph.D., Royal Institute of Technology, Stockholm, Sweden, 2002.

[30] I. Stern, "Development of Design Equations for Self-Deployable N-Strut Tensegrity Systems," M.Sc., University of Florida, Gainesville, FL, USA, 1999.

[31] J. P. Pinaud, S. Solari, and R. E. Skelton, "Deplоment of a class 2 tensegrity boom," in *SPIE's 11th Annual International Symposium on Smart Structures and Materials*, San Diego, CA, USA, 2004.

[32] J. Aldrich, R. E. Skelton, and K. Kreutz-Delgado, "Control Synthesis for a Class of Light and Agile Robotic Tensegrity Structures," in *Proceedings of the American Control Conference*. Denver, CO, USA: Ieee, 2003, pp. 5245–5251.

[33] C. Sultan, M. Corless, and R. E. Skelton, "Tensegrity Flight Simulator," *Journal of Guidance Control and Dynamics*, vol. 23, no. 6, pp. 1055–1064, 2000.

[34] M. Arsenault and C. M. Gosselin, "Dynamic Simulation of a Spatial 3-DOF Tensegrity Mechanism," *Transactions of the Canadian Society for Mechanical Engineering*, vol. 29, no. 4, pp. 491–506, 2005.

[35] ——, "Kinematic, Static, and Dynamic Analysis of a Spatial Three-Degree-of-Freedom Tensegrity Mechanism," *Journal of Mechanical Design*, vol. 128, no. 5, pp. 1061–1069, 2006.

[36] ——, "Kinematic and Static Analysis of a Planar Modular 2-DoF Tensegrity Mechanism," in *Proceedings of the 2006 IEEE International Conference on Robotics and Automation*, Orlando, FL, USA, 2006, pp. 4193–4198.

[37] ——, "Kinematic and Static Analysis of a Three-degree-of-freedom Spatial Modular Tensegrity Mechanism," *International Journal of Robotics Research*, vol. 27, no. 8, pp. 951–966, 2008.

[38] M. Marshall and C. D. Crane, "Design and Analysis of a Hybrid Parallel Platform that Incorporates Tensegrity," in *Proceedings of the 2004 ASME Design Engineering Technical Conferences*, Salt Lake City, Utah, USA, 2004, pp. 535–540.

[39] C. Paul, J. Roberts, H. Lipson, and F. J. Valero-Cuevas, "Gait Production in a Tensegrity Based Robot," in *Proceedings of the 12th International Conference on Advanced Robotics*. Seattle, WS, USA: Ieee, 2005, pp. 216–222.

[40] C. Paul, F. J. Valero-Cuevas, and H. Lipson, "Design and Control of Tensegrity Robots for Locomotion," *IEEE Transactions on Robotics*, vol. 22, no. 5, pp. 944–957, Oct. 2006.

[41] J. Rieffel, B. Trimmer, and H. Lipson, "Mechanism as Mind: What Tensegrities and Caterpillars Can Teach Us about Soft Robotics," in *Artificial Life XI: Proceedings of the Eleventh International Conference on the Simulation and Synthesis of Living Systems*, 2008, pp. 506–512.

[42] M. Shibata, F. Saijyo, and S. Hirai, "Crawling by Body Deformation of Tensegrity Structure Robots," in *Proceedings of the 2009 IEEE International Conference on Robotics and Automation*. Kobe, Japan: Ieee, May 2009, pp. 4375–4380.

[43] J. M. Mirats Tur, "On the Movement of Tensegrity Structures," *International Journal of Solids and Structures*, vol. 25, no. 1, pp. 1–14, 2010.

[44] S. Guest, "The stiffness of Prestressed Frameworks: A Unifying Approach," *International Journal of Solids and Structures*, vol. 43, no. 3-4, pp. 842–854, Feb. 2006.

[45] R. E. Skelton, R. Adhikari, J.-P. Pinaud, and W. Chan, "An introduction to the mechanics of tensegrity structures," in *Proceedings of the 40th IEEE Conference on Decision and Control*, Orlando, FL, USA, 2001, pp. 4254–4259.

[46] G. Tibert and S. Pellegrino, "Review of Form-Finding Methods for Tensegrity Structures," *International Journal of Solids and Structures*, vol. 18, no. 4, pp. 209–223, 2003.

[47] M. Masic, R. E. Skelton, and P. Gill, "Algebraic Tensegrity Form-Finding," *International Journal of Solids and Structures*, vol. 42, no. 16-17, pp. 4833–4858, 2005.

[48] S. H. Juan and J. M. Mirats Tur, "Tensegrity frameworks: Static analysis review," *Mechanism and Machine Theory*, vol. 43, no. 7, pp. 859–881, 2008.

[49] Y. Li, X.-Q. Feng, Y.-P. Cao, and H. Gao, "A Monte Carlo Form-Finding Method for Large Scale Regular and Irregular Tensegrity Structures," *International Journal of Solids and Structures*, vol. 47, no. 14-15, pp. 1888–1898, 2010.

[50] C. Paul, H. Lipson, and F. J. V. Cuevas, "Evolutionary form-finding of tensegrity structures," in *Proceedings of the 2005 conference on Genetic and evolutionary computation*, New York, NY, 2005, pp. 3–10.

[51] C. Calladine, "Buckminster Fuller's "Tensegrity" Structures And Clerk Maxwell's Rules For The Construction Of Stiff Frames," *International Journal of Solids and Structures*, vol. 14, no. 2, pp. 161–172, 1978.

[52] S. Pellegrino and C. Calladine, "Matrix Analysis of Statically and Kinematically Indeterminate Frameworks," *International Journal of Solids and Structures*, vol. 22, no. 4, pp. 409–428, 1986.

[53] S. Pellegrino, "Analysis of Prestressed Mechanisms," *International Journal of Solids and Structures*, vol. 26, no. 12, pp. 1329–1350, 1990.

[54] A. Back and R. Connelly, "Catalogue of symmetric tensegrities," 1998. [Online]. Available: http://mathlab.cit.cornell.edu/visualization/tenseg/tenseg.html

[55] R. Connelly and B. Terrell, "Highly symmetric tensegrity structures," 2008. [Online]. Available: http://www.math.cornell.edu/~tens/

[56] H. Kenner, *Geodesic Math and How to Use It.* University of California Press, 1976.

[57] R. S. Tobie, "A report on an inquiry into the existence, formation and representation of tensile structures," Master's thesis, Pratt Institute, 1967.

[58] J. Angeles, *Rational Kinematics.* Spring, 1989.

[59] J. Nocedal and S. Wright, *Numerical Optimization.* Springer, 1999.

[60] C. M. Gosselin and J. Angeles, "Singularity Analysis of Closed-Loop Kinematic Chains," *IEEE Transactions on Robotics and Automation*, vol. 6, no. 3, pp. 281–290, 1990.

[61] C. Kossowski and L. Notash, "CAT4 (Cable Actuated Truss — 4 Degrees of Freedom): A Novel 4 DOF Cable Actuated Parallel Manipulator," *Journal of Robotic Systems*, vol. 4, no. 12, pp. 605–615, 2002.

[62] O. Masory and J. Wang, "Workspace Evaluation of Stewart Platforms," in *Proceedings of the 1992 ASME Design Technical Conferences*, Scottsdale, AZ, USA, 1992, pp. 337–346.

[63] C. Leclerc and C. M. Gosselin, "Multiobjective Genetic Algorithm for Optimizing Cable-Driven Mechanisms - A Flight Simulator Approach," in *Proceedings of the 2009 CCToMM M3 Symposium*, Quebec City, Quebec, Canada, 2009, pp. 1–12.

[64] M. J. D. Otis, S. Perreault, T.-L. Nguyen-Dang, P. Lambert, M. Gouttefarde, D. Laurendeau, and C. M. Gosselin, "Determination and Management of Cable Interferences Between Two 6-DOF Foot Platforms in a Cable-Driven Locomotion Interface," *IEEE Transactions on Systems, Man, and Cybernetics - Part A: Systems and Humans*, vol. 39, no. 3, pp. 528–544, 2009.

[65] R. E. Moore, R. B. Kearfott, and M. J. Cloud, *Introduction to Interval Analysis*. Society for Industrial and Applied Mathematics, 2009.

[66] S. Bouchard, C. M. Gosselin, and B. Moore, "On the Ability of a Cable-Driven Robot to Generate a Prescribed Set of Wrenches," in *Proceedings of the 2008 ASME International Design Engineering Technical Conferences*. Brooklyn, NY, USA: ASME, 2008.

[67] S. Abdelaziz, P. Renaud, B. Bayle, and M. D. Mathelin, "Combining Structural and Kinematic Analysis Using Interval Analysis for a Wire-Driven Manipulator," in *Advances in Robot Kinematics: Motion in Man and Machine*. Springer Netherlands, 2010, pp. 147–156.

[68] M. Gouttefarde, D. Daney, and J.-p. Merlet, "Interval-Analysis-Based Determination of the Wrench-Feasible Workspace of Parallel Cable-Driven Robots," *IEEE Transactions on Robotics*, vol. 27, no. 1, pp. 1–13, 2011.

[69] K. D. Gibson and H. A. Scheraga, "Volume of the intersection of three spheres of unequal size: a simplified formula," *Journal of Physical Chemistry*, vol. 91, no. 15, pp. 4121–4122, 1987.

[70] M. Gouttefarde and C. M. Gosselin, "Analysis of the Wrench-Closure Workspace of Planar Parallel Cable-Driven Mechanisms," *IEEE Transactions on Robotics*, vol. 22, no. 3, pp. 434–445, Jun. 2006.

[71] P. Bosscher and A. T. Riechel, "Wrench-feasible workspace generation for cable-driven robots," *IEEE Transactions on Robotics*, vol. 22, no. 5, pp. 890–902, 2006.

[72] C. Barber and D. Dobkin, "The quickhull algorithm for convex hulls," *ACM Transactions on Mathematical Software*, vol. 22, no. 4, pp. 469–483, 1996.

[73] B. Grünbaum, *Convex Polytopes*. Springer, 2003.

[74] M. Gouttefarde and S. Krut, "Characterization of Parallel Manipulator Available Wrench Set Facets," *Advances in Robot Kinematics: Motion in Man and Machine*, no. Section 4, pp. 475–482, 2010. [Online]. Available: http://www.springerlink.com/index/10.1007/978-90-481-9262-5

[75] N. Riehl, "Modelisation et Conception de Robots Paralleles a Cables de Grande Dimension," Ph.D., Universite Montpellier II, Montpellier, France, 2011.

[76] C. Huang, W.-H. Hung, and I. Kao, "New Conservative Stiffness Mapping for the Stewart-Gough Platform," in *Proceedings of the 2002 IEEE International Conference on Robotics and Automation*, vol. 1, Washington, DC, 2002, pp. 823–828.

[77] M. Svinin, S. Hosoe, and M. Uchiyama, "On the Stiffness and Stability of Gough-Stewart Platforms," in *Proceedings of the 2001 IEEE International Conference on Robotics and Automation*, Seoul, Korea, 2001, pp. 3268–3273.

[78] M. Arsenault, "Stiffness Analysis of a 2-DOF Planar Tensegrity Mechanism," in *Proceedings of the 2008 ASME International Design Engineering Technical Conferences*, Brooklyn, NY, USA, 2008, pp. 78–83.

[79] C. M. Gosselin, "Stiffness Mapping for Parallel Manipulators," *IEEE Transactions on Robotics and Automation*, vol. 6, no. 3, pp. 377–382, 1990.

[80] Z. Bingul and O. Karahan, "Dynamic modeling and simulation of stewart platform," in *Serial and Parallel Robot Manipulators - Kinematics, Dynamics, Control and Optimization*. InTech, 2012.

[81] L.-W. Tsai, "Solving the inverse dynamics of a stewart-gough manipulator by the principle of virtual work," *Journal of Mechanical Design*, vol. 122, no. 1, p. 3, 2000.

[82] J. Lin and C. W. Chen, "Computer-aided-symbolic dynamic modelling for stewart-platform manipulator," *Robotica*, vol. 27, no. 3, pp. 331–341, 2008.

[83] S. Behzadipour, R. Dekker, A. Khajepour, and E. Chan, "Deltabot: a new cable-based ultra high speed robot," *ASME International Mechanical Engineering Congress and Expo*, 2003.

[84] P. Bosscher and I. Ebert-Uphoff, "A Novel Mechanism for Implementing Multiple Collocated Spherical Joints," in *Proceedings of the 2003 IEEE International Conference on Robotics and Automation.* Taipei, Taiwan: Ieee, 2003, pp. 336–341.

[85] S. K. Song, D. S. Kwon, and W. S. Kim, "Spherical Joint for Coupling Three or More Links Together at One Point," 2003.

[86] G. J. Hamlin and A. Sanderson, "A Novel Concentric Multilink Spherical Joint with Parallel Robotics Applications," in *Proceedings of the 1994 IEEE International Conference on Robotics and Automation*, Troy, NY, USA, 1994, pp. 1267–1272.

[87] C. B. Pham, G. Yang, and S. H. Yeo, "Dynamic Analysis of Cable-Driven Parallel Mechanisms," in *Proceedings of the 2005 IEEE/ASME International Conference on Advanced Intelligent Mechatronics.* Monterey, CA, USA: Ieee, 2005, pp. 612–617.

[88] M. Aref and H. Taghirad. (2012) Cdrpm research group, k.n.toosi university of technology. [Online]. Available: http://saba.kntu.ac.ir/eecd/aras/projects/cdrpm.htm

[89] J. B. Ziegler and N. B. Nichols, "Optimum settings for automatic controllers," *ASME Transactions*, vol. 64, pp. 759–768, 1942.

[90] G. Billette, "Robot parallèle à câbles simulant des contacts rigides," Master's thesis, Université Laval, Québec, 2009.

Appendices

A Analysis of the Spring Linkages

A.1 Kinematic Analysis

The pose of each spring linkage is fully determinate if the location of the end-point, i.e., node B_i, is known. This is thanks to the selected directions of the universal joint axes that connect each spring linkage to the mechanism base. The links are oriented using the three angles $\theta_i, \alpha_i, \beta_i$ as shown in Figure A.1. Given the position, $\mathbf{p}$, and orientation, $\mathbf{Q}$, of the end-effector the location of B_i is:

$$\mathbf{b}_i = \mathbf{p} + \mathbf{Q}\mathbf{b}'_i \tag{A.1}$$

from which the three angles and their time derivatives can be calculated.

Calculating $\theta_i, \dot{\theta}_i$:

Consider the right-angled triangle formed by points C_i, B_i, and the midpoint of line $\overline{A_iB_i}$. One of this triangle's angles is equal to θ_i such that:

$$\sin(\theta_i) = \frac{l_i/2}{l_0/2} = \frac{l_i}{l_0} \tag{A.2}$$

The length $l_i = \sqrt{(\mathbf{b}_i - \mathbf{a}_i)^{\mathrm{T}}(\mathbf{b}_i - \mathbf{a}_i)}$, which is then substituted into the equation to give the following expression for θ_i:

$$\theta_i = \operatorname{asin}\left(\frac{\sqrt{(\mathbf{b}_i - \mathbf{a}_i)^{\mathrm{T}}(\mathbf{b}_i - \mathbf{a}_i)}}{l_0}\right) \tag{A.3}$$

Squaring Equation A.2 gives:

$$\mathrm{s}^2\theta_i = \frac{1}{l_0^2}(\mathbf{b}_i - \mathbf{a}_i)^{\mathrm{T}}(\mathbf{b}_i - \mathbf{a}_i) \tag{A.4}$$

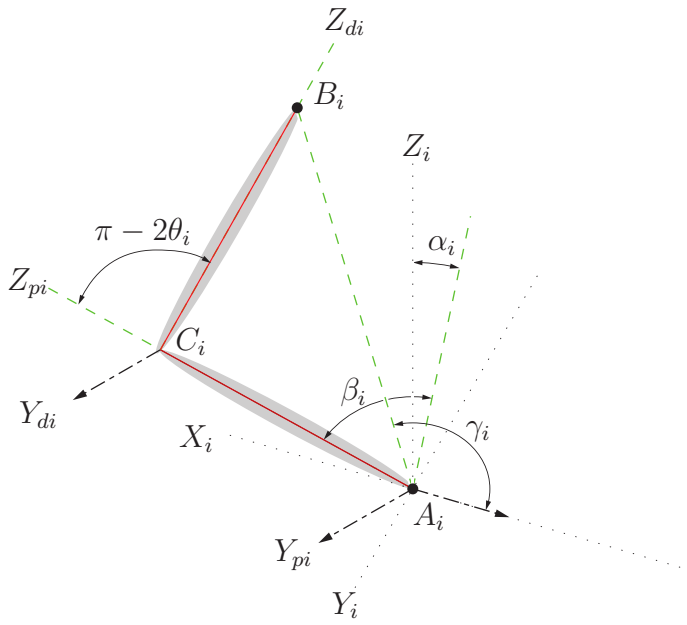

Figure A.1: Definitions of the spring linkage leg angles.

which can be differentiate with respect to time, yielding:

$$\dot{\theta}_i = \frac{1}{\mathrm{s}\theta_i \mathrm{c}\theta_i l_0^2} \dot{\mathbf{b}}^{\mathrm{T}} (\mathbf{b}_i - \mathbf{a}_i) \tag{A.5}$$

where $\dot{\mathbf{b}}_i = \dot{\mathbf{p}} + \boldsymbol{\omega} \times \mathbf{Q}\mathbf{b}'_i$ and $\boldsymbol{\omega}$ is the angular velocity of the end-effector in the global reference frame.

Calculating $\alpha_i, \dot{\alpha}_i$:

The first axis of rotation for the universal joint at A_i is:

$$\mathbf{e}_{1i} = \frac{\mathbf{k} \times \mathbf{a}_i}{||\mathbf{k} \times \mathbf{a}_i||} \tag{A.6}$$

and the second axis is normal to the plane that contains both $\mathbf{e}_{1i}$ and $(\mathbf{b}_i - \mathbf{a}_i)$:

$$\mathbf{e}_{2i} = \frac{\mathbf{e}_{1i} \times (\mathbf{b}_i - \mathbf{a}_i)}{||\mathbf{e}_{1i} \times (\mathbf{b}_i - \mathbf{a}_i)||} \tag{A.7}$$

The angle between the unit vector $\mathbf{k} = [0, 0, 1]^{\mathrm{T}}$ and the second axis of rotation is the complementary angle of α_i. It can be found using the dot

product of the two vectors:

$$(\mathbf{e}_{1i} \times (\mathbf{b}_i - \mathbf{a}_i))^{\mathrm{T}}\mathbf{k} = \cos(\pi/2 - \alpha_i)\sqrt{(\mathbf{b}_i - \mathbf{a}_i)^{\mathrm{T}}(\mathbf{b}_i - \mathbf{a}_i)}$$
$$= \sin(\alpha_i)\sqrt{(\mathbf{b}_i - \mathbf{a}_i)^{\mathrm{T}}(\mathbf{b}_i - \mathbf{a}_i)} \tag{A.8}$$

from which α_i is found to be:

$$\alpha_i = \mathrm{asin}\left(\frac{(\mathbf{e}_{1i} \times (\mathbf{b}_i - \mathbf{a}_i))^{\mathrm{T}}\mathbf{k}}{\sqrt{(\mathbf{b}_i - \mathbf{a}_i)^{\mathrm{T}}(\mathbf{b}_i - \mathbf{a}_i)}}\right) \tag{A.9}$$

Squaring both sides of Equation A.8 and taking the time derivative yields:

$$\dot{\alpha_i} = \frac{1}{2\mathrm{s}\alpha_i \mathrm{c}\alpha_i}\left(\frac{(\mathbf{e}_{1i} \times (\mathbf{b}_i - \mathbf{a}_i))^{\mathrm{T}}\mathbf{k}(\mathbf{e}_{1i} \times \dot{\mathbf{b}}_i)^{\mathrm{T}}\mathbf{k}}{\dot{\mathbf{b}}_i^{\mathrm{T}}(\mathbf{b}_i - \mathbf{a}_i)}\right) \tag{A.10}$$

Calculating $\beta_i, \dot{\beta}_i$:

From Figure A.1, the angle between the line $\overline{A_iB_i}$ and the first joint axis is equal to:

$$\gamma_i = \pi/2 + \beta_i - (\pi/2 - \theta_i) = \beta_i + \theta_i \tag{A.11}$$

and can be found by taking the dot product:

$$(\mathbf{b}_i - \mathbf{a}_i)^{\mathrm{T}}\mathbf{e}_{1i} = \cos(\beta_i + \theta_i)\sqrt{(\mathbf{b}_i - \mathbf{a}_i)^{\mathrm{T}}(\mathbf{b}_i - \mathbf{a}_i)} \tag{A.12}$$

which can be solved for β_i as follows:

$$\beta_i = -\theta_i + \mathrm{acos}\left(\frac{(\mathbf{b}_i - \mathbf{a}_i)^{\mathrm{T}}\mathbf{e}_{1i}}{\sqrt{(\mathbf{b}_i - \mathbf{a}_i)^{\mathrm{T}}(\mathbf{b}_i - \mathbf{a}_i)}}\right) \tag{A.13}$$

If Equation A.12 is squared and differentiated with respect to time, then $\dot{\beta}_i$ can be found as:

$$\dot{\beta}_i = -\dot{\theta}_i - \frac{1}{2\mathrm{s}(\beta_i + \theta_i)\mathrm{c}(\beta_i + \theta_i)}\left(\frac{(\mathbf{b}_i - \mathbf{a}_i)^{\mathrm{T}}\mathbf{e}_{1i}(\dot{\mathbf{b}}_i^{\mathrm{T}}\mathbf{e}_{1i})}{(\mathbf{b}_i - \mathbf{a}_i)^{\mathrm{T}}\dot{\mathbf{b}}_i}\right) \tag{A.14}$$

A.2 Static Analysis

The static force exerted by each spring linkage was found using a 3D vector approach. Vector definitions are included in Figure A.2 as a reminder. The

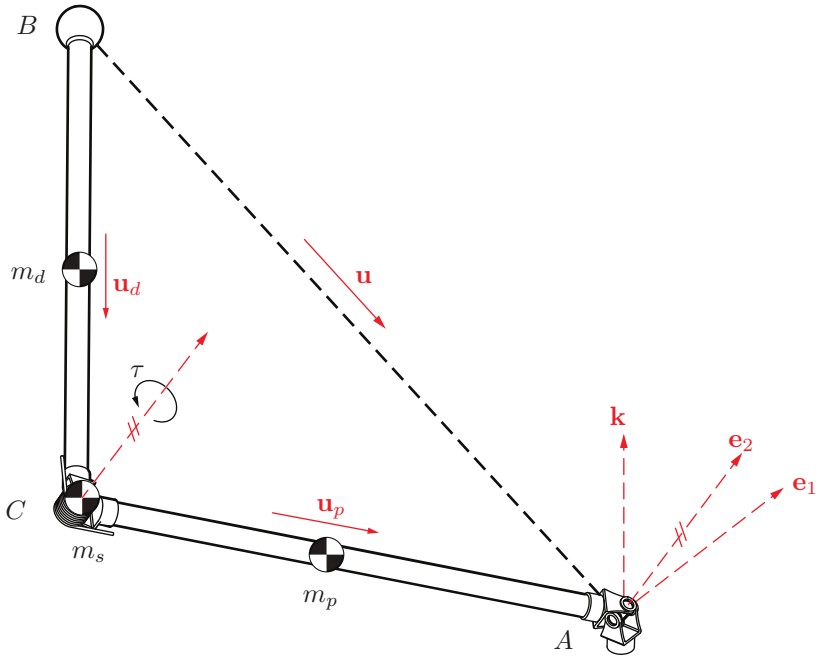

Figure A.2: Vector definitions for the spring linkage

unit vectors $\mathbf{e}_1$, $\mathbf{e}_2$ represent the first and second axes of the universal joint at node B. The reaction forces $\mathbf{f}_A, \mathbf{f}_B, \mathbf{f}_C$ and the reaction moments $\mathbf{n}_A, \mathbf{n}_B, \mathbf{n}_C$ are at nodes A, B, C, respectively. Unit vectors $\mathbf{u}_\mathrm{p}$ and $\mathbf{u}_\mathrm{d}$ represent the direction of the proximal and distal links. The mass of the links are m_p and m_d, and their centres of mass are at their midpoints. The mass of the spring joint is treated as a point mass of m_s at node C. The gravitational vector is $\mathbf{g} = [0, 0, \pm 9.81]^\mathrm{T}$, depending on the orientation of the mechanism with respect to its base.

Taking a force and moment balance about the proximal link, shown in Figure A.3, at node A gives the following two equations:

$$\mathbf{f}_A + \mathbf{f}_C + m_p\mathbf{g} + m_s\mathbf{g} = \mathbf{0} \tag{A.15}$$

$$\mathbf{n}_A + \mathbf{n}_C - \frac{1}{4}l_0\mathbf{u}_\mathrm{p} \times m_p\mathbf{g} - \frac{1}{2}l_0\mathbf{u}_\mathrm{p} \times m_s\mathbf{g} - \frac{1}{2}l_0\mathbf{u}_\mathrm{p} \times \mathbf{f}_C = \mathbf{0} \tag{A.16}$$

Likewise, a force and moment balance of the distal link about node C yields

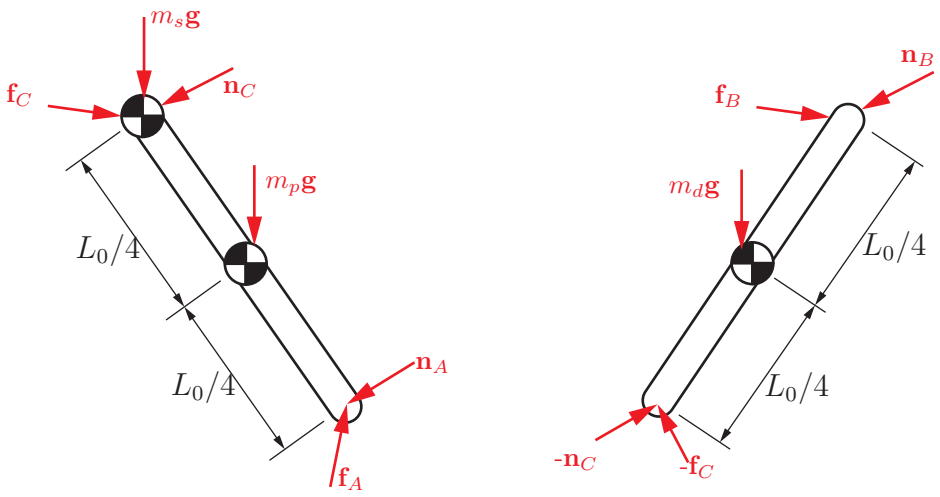

Figure A.3: Free body diagrams of the proximal and distal links.

another two equations.

$$\mathbf{f}_B - \mathbf{f}_C + m_d\mathbf{g} = \mathbf{0} \tag{A.17}$$

$$\mathbf{n}_B - \mathbf{n}_C - \frac{1}{4}l_0\mathbf{u}_\mathrm{d} \times m_d\mathbf{g} - \frac{1}{2}l_0\mathbf{u}_\mathrm{d} \times \mathbf{f}_B = \mathbf{0} \tag{A.18}$$

The joint at node B is spherical and will not transmit any moments, therefore $\mathbf{n}_B = \mathbf{0}$. Equations A.17 and A.18 are rearranged to find expressions for $\mathbf{f}_C$ and $\mathbf{n}_C$:

$$\mathbf{f}_C = \mathbf{f}_B + m_d\mathbf{g} \tag{A.19}$$

$$\mathbf{n}_C = -\frac{1}{4}l_0\mathbf{u}_\mathrm{d} \times m_d\mathbf{g} - \frac{1}{2}l_0\mathbf{u}_\mathrm{d} \times \mathbf{f}_B \tag{A.20}$$

and then substituted into Equation A.16 to find an expression for $\mathbf{n}_A$ in terms of only $\mathbf{f}_B$.

$$\mathbf{n}_A = -\frac{1}{2}l_0\left[\mathbf{f}_B \times (\mathbf{u}_\mathrm{p} + \mathbf{u}_\mathrm{d})\right] - \frac{1}{2}l_0\mathbf{g} \times \left[\left(\frac{1}{2}m_p + m_s + m_d\right)\mathbf{u}_\mathrm{p} + \frac{1}{2}m_d\mathbf{u}_\mathrm{d}\right] \tag{A.21}$$

The deflection of the torsion spring is known from the inverse kinematics, from which the torque, τ, exerted on the revolute joint at node C can be calculated. The axis of this joint is $\mathbf{e}_2$, which gives the following:

$$\mathbf{n}_C^\mathrm{T}\mathbf{e}_2 = \tau \tag{A.22}$$

Substituting Equation A.20 for $\mathbf{n}_C$ and rearranging gives:

$$(\mathbf{u}_\mathrm{d} \times \mathbf{e}_2)^\mathrm{T} \mathbf{f}_B = \frac{2}{l_0}\tau - \left(\frac{1}{2} m_d \mathbf{g} \times \mathbf{u}_\mathrm{d}\right)^\mathrm{T} \mathbf{e}_2 \tag{A.23}$$

Similarly, the universal joint at node A will not transmit moments along its axes leading to the following two identities:

$$\mathbf{n}_A^\mathrm{T} \mathbf{e}_1 = 0 \tag{A.24}$$

$$\mathbf{n}_A^\mathrm{T} \mathbf{e}_2 = 0 \tag{A.25}$$

Equation A.21 is substituted in place of $\mathbf{n}_A$ and the identities are rearranged to give:

$$[(\mathbf{u}_\mathrm{p} + \mathbf{u}_\mathrm{d}) \times \mathbf{e}_1]^\mathrm{T} \mathbf{f}_B = -(\mathbf{g} \times \mathbf{e}_1)^\mathrm{T} \left[\left(\frac{1}{2} m_p + m_s + m_d\right) \mathbf{u}_\mathrm{p} + \frac{1}{2} m_d \mathbf{u}_\mathrm{d}\right] \tag{A.26}$$

$$[(\mathbf{u}_\mathrm{p} + \mathbf{u}_\mathrm{d}) \times \mathbf{e}_2]^\mathrm{T} \mathbf{f}_B = -(\mathbf{g} \times \mathbf{e}_2)^\mathrm{T} \left[\left(\frac{1}{2} m_p + m_s + m_d\right) \mathbf{u}_\mathrm{p} + \frac{1}{2} m_d \mathbf{u}_\mathrm{d}\right] \tag{A.27}$$

Equations A.23, A.26, and A.27 form a system of equations that can be solved for the force exerted by each spring linkage $\mathbf{f}_i = \mathbf{f}_{Bi}$, $i = 1, 2, 3$, so long as the linkages are not in singular poses, i.e., fully extended or folded.

$$\mathbf{f}_i = \begin{bmatrix} (\mathbf{u}_{\mathrm{d}i} \times \mathbf{e}_{2i})^\mathrm{T}) \\ [(\mathbf{u}_{\mathrm{d}i} + \mathbf{u}_{\mathrm{p}i}) \times \mathbf{e}_{1i}]^\mathrm{T} \\ [(\mathbf{u}_{\mathrm{d}i} + \mathbf{u}_{\mathrm{p}i}) \times \mathbf{e}_{2i}]^\mathrm{T} \end{bmatrix}^{-1} \begin{bmatrix} \frac{2}{l_0}\tau_i - (\frac{1}{2} m_d \mathbf{g} \times \mathbf{u}_{\mathrm{d}i})^\mathrm{T} \mathbf{e}_{2i} \\ -(\mathbf{g} \times \mathbf{e}_{1i})^\mathrm{T} [(\frac{1}{2} m_p + m_s + m_d) \mathbf{u}_{\mathrm{p}i} + \frac{1}{2} m_d \mathbf{u}_{\mathrm{d}i}] \\ -(\mathbf{g} \times \mathbf{e}_{2i})^\mathrm{T} [(\frac{1}{2} m_p + m_s + m_d) \mathbf{u}_{\mathrm{p}i} + \frac{1}{2} m_d \mathbf{u}_{\mathrm{d}i}] \end{bmatrix} \tag{A.28}$$